

2D Reduced Order Model for Vascular Calcification

by

Jucelino Santos Fortes

to obtain the degree of Master of Science
at the Delft University of Technology,
to be defended publicly on May 14th 2025.

Student number:	4487524	
Thesis committee:	Prof. dr. ir. M.B. van Gijzen,	TU Delft, supervisor
	Dr. H. Yoldas,	TU Delft, supervisor
	Dr.ir. E.G. Rens,	TU Delft
Advisor:	Dr. S. Pirola,	TU Delft, supervisor

Acknowledgement

I want to thank my supervisors, Prof. Dr. Ir. Martin B. van Gijzen, Dr. Havva Yoldas, and Dr. Selene Pirola, for their guidance, availability, and expertise throughout my master's thesis. I also want to thank Pritesh Ramya and Federica Fontana for their help with FEBio. Understanding FEBio without their help would have taken much longer. I thank my brother Marvino Santos Fortes for running simulations on their server. I lastly want to thank my remaining brothers, Alineu Santos Fortes and Silvio Santos Fortes, for their support during my master's thesis.

Abstract

Vascular calcification, the deposition of calcium in the vessel wall, is associated with several vascular diseases, including atherosclerosis, diabetes mellitus, and hypertension. Fluid-structure interaction (FSI) is recommended to simulate blood flow incorporating vascular calcification. However, FSI applied to a three-dimensional (3D) model takes several days to simulate. To reduce the computational complexity, 1D reduced order models (ROMs) are often used instead.

Reduced order modeling decreases the computational complexity of a model by removing dimensions of the coordinate system within a model. The cylindrical coordinate system is used in hemodynamics, especially in ROMs. The 1D ROM for hemodynamics is obtained by removing the azimuthal dimension (accomplished by assuming axial symmetry for all properties within arteries) and the radial dimension (accomplished by applying a predefined velocity profile to blood flow) from the 3D model. However, incorporating vascular calcification can make the geometry of arteries and flow within arteries asymmetric. A 2D ROM can increase the accuracy of the 1D ROM by including one of the two removed dimensions. Research regarding 2D blood flow mainly focuses on including the radial dimension, which cannot implement asymmetric calcification since axisymmetry is assumed.

This study obtains a 2D ROM for blood flow by removing the dimension corresponding to the radial distance from the three-dimensional model and by assuming that axial velocity is continuous in the neighborhood near the artery's origin. The 2D ROM obtains axisymmetric velocity by only allowing a single velocity profile. However, enabling a family of velocity profiles can make flow within arteries asymmetric. Hence, this study contributes to hemodynamics by studying blood flow that allows a family of velocity profiles.

A non-physiological steady-state solution has been obtained analytically, in which the volumetric flow rate vanishes, and numerical methods are developed to simulate the 2D ROM, which incorporates dimensional (Godunov) splitting, linear approximate solvers, and high-resolution methods. Jump-discontinuities within the mechanical properties of the vascular walls are smoothed for the 2D simulations. Numerical methods for the 2D ROM yield significant errors within the smoothing region for simulations with coarse grids. The numerical method obtains the non-physiological steady-state solutions for arteries without calcification and has a relative error of $\mathcal{O}(\Delta x^{1.500})$ for arteries with axisymmetric calcification. The 2D ROM cannot numerically obtain the non-physiological steady-state solution for arteries with asymmetric calcification due to the numerical errors within the smoothing range.

3D and 2D numerical simulations with pulsatile blood flow are compared. The 3D simulation without calcification has a significantly higher diastolic pressure, larger inner wall radii, and larger volumetric flow rates than the 2D simulation. The differences in blood flow observed between pulsatile blood flow without calcification and with calcification match decently between the 3D simulations and the 2D simulations, except for locations within the smoothing region.

Keywords: 2D blood flow, asymmetric blood flow, vascular calcification, reduced order model

Contents

1	Introduction	1
1.1	Preliminaries	2
1.1.1	Definitions, theorems, and lemmas	2
1.1.2	Cylindrical coordinate system	4
1.2	Blood flow in three dimensions	5
1.2.1	Deformations of vascular walls.	5
1.2.2	Hemodynamics	5
1.2.3	Interface conditions	6
1.3	Reduced order modeling	6
1.3.1	General idea regarding reduced order modeling	7
1.3.2	Assumptions 1D blood flow	7
1.3.3	Linear elastic deformation model	8
1.3.4	1D reduced order model for blood flow	8
1.4	Finite volume methods for hyperbolic equations	9
1.4.1	Godunov method for one dimension.	10
1.4.2	1D Riemann problem for linear hyperbolic equation	10
1.4.3	1D Riemann problem for non-linear hyperbolic equation	10
1.4.4	1D Numerical schemes for hyperbolic equations	11
1.4.5	Finite volume methods for higher dimensions	13
2	Method	14
2.1	Problem description	14
2.2	2D Reduced order model	15
2.2.1	Assumptions.	16
2.2.2	Axisymmetric flow model	19
2.2.3	Asymmetric flow model	21
2.2.4	Numerical methods	25
2.2.5	Steady-state solutions	31
2.3	3D simulations	33
2.3.1	Mesh.	33
2.3.2	Calcification	34
2.3.3	Materials.	34
2.3.4	Boundary conditions.	35
2.3.5	Simulation	35
3	Results	37
3.1	Simulations without calcification	37
3.1.1	Upwind, Lax-Wendroff, and high-resolution methods	37
3.1.2	Numerical stability.	39
3.1.3	Steady-state solutions	40
3.2	Simulations with axisymmetric calcification	44
3.2.1	Simulations with fixed inlet	44
3.2.2	Steady-state solutions	45
3.2.3	Numerical stability.	50
3.3	Simulations with local calcification	52
3.3.1	Issues with continuity condition	52
3.3.2	Steady-state solutions	53

3.4 Simulations with pulsatile flow	58
3.4.1 No Calcification	59
3.4.2 Axisymmetric Calcification	61
3.4.3 Local Calcification	63
4 Conclusion	73
Bibliography	75
A The Axisymmetric Flow Model	77
A.1 Conservation of mass	77
A.2 Balance of momentum	78
A.3 Differential form	80
B The Asymmetric Flow Model	81
B.1 Conservation of mass	81
B.2 Balance of momentum	82
B.3 Differential form	84
C Roe's Linearization to 1D Blood Flow	85
D Lemma Lagrange (2D)	86

1

Introduction

Vascular calcification, the deposition of calcium in the vessel wall, is associated with several vascular diseases, including atherosclerosis (narrowing of blood vessel walls due to plaque), diabetes mellitus, hypertension (high blood pressure), and more [29]. Vascular calcification is categorized depending on where calcium is deposited in the vessel wall [11].

A blood vessel consists of the vessel wall and lumen (the area where blood flows). The vessel wall consists of three layers (see Figure 1.1), namely the tunicas intima, media and externa (which is also referred to as tunica adventitia) [14], [16]. The tunica externa holds the vessel in its relative position. The tunica media mainly

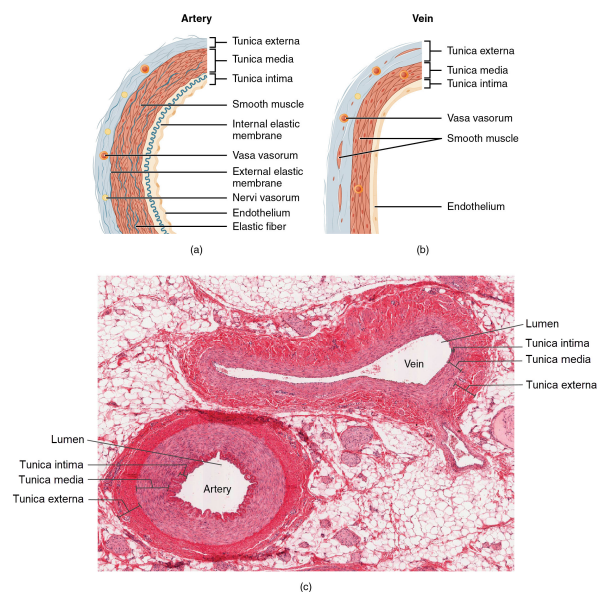


Figure 1.1: Structure of the vessel walls [14].

consists of smooth muscle cells, which enable vasoconstriction (narrowing the vessel's lumen) and vasodilation (enlarging the vessel's lumen). The tunica intima mainly consists of the endothelium, which serves as the boundary between the lumen and the vessel wall and releases chemicals that constrict (narrow) the smooth muscle cells [14]. The sizes and elasticity of these layers depend on the location of the blood vessels [14].

Vascular calcification in arteries occurs in the tunica intima and tunica media [29] and are classified as intimal arterial calcification and medial arterial calcification, respectively. The exact molecular mechanisms that contribute to the development of vascular calcification are still unknown [11], [10], and yet some papers plaque growth in their model [8].

Computational simulations have been used for several years to aid research in medicine [15]. There are two branches of numerical methods to simulate blood flow in arteries, which are computational fluid dynamics (CFD) and fluid-structure interaction (FSI) [9]. FSI combines CFD and finite element analysis (FEA), in which CFD simulates fluid flow, and FEA simulates the vessel wall. Due to the added computational complexity of the deformable wall, FSI takes significantly longer to simulate than CFD. As simulated in Brown et al. [2], a 3D CFD simulation of the aorta took 6.6 hours, while a 3D FSI simulation took 145 hours [15]. FSI is recommended to simulate blood flow with atherosclerosis [9].

There are many ways to reduce the computational time of a simulation, such as improving the algorithm incorporated in the numerical method, upgrading the software of the machine, and simplifying the mathematical model. One way to simplify the model is to apply assumptions to reduce the problem's dimensions, known as reduced-order modeling, reduced-dimensional modeling, or reduced modeling (not to be confused with reduced-order modeling applied in scientific computing). A 2D reduced order model (ROM) can be obtained by assuming axial symmetry [3], which can be further reduced to a 1D ROM by applying a predefined velocity profile [18].

An issue with the aforementioned 2D and 1D ROMs denoted in [3] and [18] is that these models assume axial symmetry. The addition of vascular calcification can make the geometry of arteries and flow within the artery asymmetric. One way of obtaining a 2D ROM that does not break axial symmetry is to apply a predefined velocity profile. However, no papers are found that research this 2D ROM for blood flow. Once calcification is applied asymmetrically, this 2D ROM should be less computationally complex than the 3D problem and more accurate than the 1D ROM.

This study obtains a 2D reduced order model (ROM) for blood flow that can model medial calcification asymmetrically by studying the following research questions:

- 1) What is the mathematical expression for the 2D ROM that can model blood flow asymmetrically?
 - a) Does the 2D the ROM have steady-state solutions?
- 2) How to develop a numerical method for the 2D ROM?
 - a) When is the numerical method stable?
 - b) How accurate is the numerical method?
- 3) How well do 2D simulations compare with 3D simulations?

This study is split into four chapters. The current chapter provides preliminary information regarding known mathematical definitions and theorems, blood flow in three dimensions, reduced order modeling, and finite volume methods. Chapter 2 'Method' describes the problem, studies the 2D ROM, and discusses how the 3D model is simulated. Chapter 3 'Results' discusses the results obtained from simulations. This study ends with Chapter 4 'Conclusion.'

1.1. Preliminaries

This section discusses the mathematical definitions, theorems, and lemmas used in this study and the cylindrical coordinate system.

1.1.1. Definitions, theorems, and lemmas

Preliminary theorems and lemmas will not be proven in this study.

Definition *Injective mapping.* A mapping $f : A \rightarrow B$ is injective if for all $x \in A$ and $y \in A$, f has the identity:

$$x \neq y \implies f(x) \neq f(y). \quad (1.1.1)$$

Definition *Surjective mapping.* A mapping $f : A \rightarrow B$ is surjective if for every $y \in B$ there exists an $x \in A$ such that $f(x) = y$.

Theorem *Mean value theorem.* Let $f : [a, b] \rightarrow \mathbb{R}$ be a continuous mapping on the closed interval $[a, b]$ and differentiable on the open interval (a, b) . Then there exists a $\xi \in (a, b)$ such that

$$f'(\xi) = \frac{f(b) - f(a)}{b - a}. \quad (1.1.2)$$

Definition *Lipschitz continuity.* A mapping $f : \mathbb{R} \rightarrow \mathbb{R}$ is Lipschitz continuous on an interval $I \subseteq \mathbb{R}$ if there exists an $L > 0$ such that for every $x \in I$ and $y \in I$ we have

$$|f(x) - f(y)| < L|x - y|. \quad (1.1.3)$$

Definition *Metric space.* Let X be a nonempty set and $d : X \times X \rightarrow \mathbb{R}$ be a metric (or distance function) that satisfies the following properties for all $x, y, z \in X$:

- 1) $d(x, y) \geq 0$ and $d(x, y) = 0 \iff x = y$;
- 2) $d(x, y) = d(y, x)$;
- 3) $d(x, y) \leq d(x, z) + d(z, y)$.

The pair (X, d) is called a metric space.

Definition *Uniform continuity.* Let (X, d) and (Y, ρ) be metric spaces, and let $f : X \rightarrow Y$ be mapping. f is uniformly continuous function if for every $\varepsilon > 0$ there exists a $\delta > 0$ such that

$$d(x, y) < \delta \implies \rho(f(x), f(y)) < \varepsilon. \quad (1.1.4)$$

Theorem *Gauss' divergence theorem.* Let $\Omega \subseteq \mathbb{R}^d$ be open and $\mathbf{f} : U \rightarrow \mathbb{R}^d$ be a continuously differential vector field. Let $V \subset \Omega$ be a closed, bounded region with piecewise-smooth boundary surface Γ . Then

$$\int_V \nabla \cdot \mathbf{f} d\Omega = \int_\Gamma \mathbf{f} \cdot \mathbf{n} d\Gamma, \quad (1.1.5)$$

where \mathbf{n} is the outward-pointing unit normal vector to Γ .

Theorem *Reynolds transport theorem.* Let $\Omega_t \subset \mathbb{R}^d$ be a region that depends on time, I be an interval, and $f(t, \mathbf{x}) : I \times \Omega_t \rightarrow \mathbb{R}$ be a continuously differentiable function with respect to both $t \in I$ and $\mathbf{x} \in \mathbb{R}^d$. Then,

$$\partial_t \int_{\Omega_t} f d\mathbf{x} = \int_{\Omega_t} (\partial_t f + \nabla \cdot (f\mathbf{u})) d\mathbf{x}. \quad (1.1.6)$$

Definition *Cover.* Let X be a nonempty set, $A \subset X$ be nonempty, and let $\mathcal{F} = \{A_i\}_{i \in I}$ be a family of sets. \mathcal{F} covers A if $A \subset \bigcup_{i \in I} A_i$.

Definition *Compact set.* Let (X, d) be a metric space and $A \subset X$. A is compact if every open cover of A has a finite subcover.

Definition *Almost everywhere.* Let $\Omega \subseteq \mathbb{R}^d$ be a measurable set with a measure μ . An assertion holds almost everywhere or, a.e. on Ω if there exists a set $A \subseteq \Omega$ such that the assertions holds everywhere on A and $\mu(\Omega \setminus A) = 0$.

Definition *L^p -spaces.* Let (S, \mathcal{A}, μ) be a measure space and $p \in [1, \infty]$. For a measurable function $f : S \rightarrow \mathbb{R}$, $\|f\|_{L^p(S)}$ is defined as

$$\|f\|_{L^p(S)} = \begin{cases} \left(\int_S |f|^p d\mu \right)^{\frac{1}{p}} & \text{for } p \in [1, \infty], \\ \text{ess sup}_{s \in S} |f(s)| & \text{for } p = \infty, \end{cases} \quad (1.1.7)$$

where $\text{ess sup}_{s \in S} |f(s)| = \inf\{r : |f| < r \text{ a. e.}\}$. Sometimes the notation $\|f\|_p$ is used instead of $\|f\|_{L^p(S)}$.

Definition *Jordan measurable.* A bounded set S is Jordan measurable if $\|1\|_{L^1(S)}$ is bounded.

Theorem *Change of variables theorem.* Let $R, S \subseteq \mathbb{R}^n$ be closed, bounded, and Jordan measurable. Let $\mathbf{g} : S \rightarrow R$ be a continuous subjective mapping such that

1. \mathbf{g} is continuously differentiable and injective on the interior of S ($\text{int}(S)$).
2. The determinant of $\mathbf{g}'(\mathbf{s})$ ($J\mathbf{g}(\mathbf{s})$) is non-zero for all $s \in \text{int}(S)$.

Then for every continuous function $f : R \rightarrow \mathbb{R}$, we have

$$\int_R f(\mathbf{x}) d\mathbf{x} = \int_S f(\mathbf{g}(s)) \cdot |J\mathbf{g}(s)| ds. \quad (1.1.8)$$

Lemma *Fundamental lemma of variational calculus.* Let $\Omega \subset \mathbb{R}^d$ be open and let $f \in L^1(K)$ for every compact set $K \subset \Omega$. If for all test functions $\phi \in C_c^\infty(\Omega)$

$$\int_{\Omega} f \phi \, dx = 0, \quad (1.1.9)$$

then $f = 0$.

Lemma *Lagrange* [27]. Let f be a continuous function defined on an interval $[A, B]$. If it holds that

$$\int_a^b f(x) \, dx = 0 \quad (1.1.10)$$

for each subinterval $[a, b] \subset [A, B]$, then $f(x) = 0$ for $x \in [A, B]$.

Definition *Hyperbolic equation.* The partial differential equation $\partial_t \mathbf{q} + A(\mathbf{q}) \partial_x \mathbf{q} = 0$ is said to be hyperbolic if the A is diagonalizable with real eigenvalues.

1.1.2. Cylindrical coordinate system

The cylindrical coordinate system is often used in reduced order models (ROMs) for blood flow within arteries. This study uses the cylindrical coordinate system $(x, \varphi, r) \in \mathbb{R} \times [0, 2\pi) \times [0, \infty)$, where x is the axial coordinate, φ is the azimuth and r is the radius. This section covers several transformations between Cartesian coordinates $(x, y, z) \in \mathbb{R}^3$ and cylindrical coordinates.

Transforming coordinates

Let (x, φ, r) be a point within the cylindrical coordinate system. (x, φ, r) is mapped into the Cartesian coordinate system (x, y, z) by the mapping $\Phi: \mathbb{R} \times [0, 2\pi) \times [0, \infty) \rightarrow \mathbb{R}^3$ expressed as

$$\Phi(x, \varphi, r) = (x, r \cos \varphi, r \sin \varphi). \quad (1.1.11)$$

The mapping Φ is invertible if $(y, z) \neq (0, 0)$. For $(y, z) \neq (0, 0)$, (x, y, z) in Cartesian coordinates is mapped into cylindrical coordinates by incorporating the mapping

$$\Phi^{-1}(x, y, z) = \left(x, \theta(y, z), \sqrt{y^2 + z^2} \right), \quad (1.1.12)$$

where

$$\theta(y, z) = \begin{cases} \arctan\left(\frac{z}{y}\right) & \text{for } y > 0 \text{ and } z \geq 0, \\ \frac{1}{2}\pi & \text{for } y = 0, z > 0, \\ \arctan\left(\frac{z}{y}\right) + \pi & \text{for } y < 0 \\ \frac{3}{2}\pi & \text{for } y = 0, z < 0, \\ \arctan\left(\frac{z}{y}\right) + 2\pi & \text{for } y > 0 \text{ and } z < 0. \end{cases} \quad (1.1.13)$$

The mapping Φ is surjective, but not injective since for $r = 0$, and $\varphi_1 \neq \varphi_2$ we have $\Phi(x, \varphi_1, 0) = \Phi(x, \varphi_2, 0)$. However, injectivity is lost only for $r = 0$, which is located at the boundary of $[0, \infty)$. The Jacobian of Φ is equal to

$$\frac{\partial \Phi}{\partial(x, \varphi, r)} = \begin{vmatrix} 1 & 0 & 0 \\ 0 & -r \sin \varphi & r \cos \varphi \\ 0 & \cos \varphi & \sin \varphi \end{vmatrix} = -r(\sin^2 \varphi + \cos^2 \varphi) = -r. \quad (1.1.14)$$

Thus the change of variables theorem can be applied for every closed, bounded, and Jordan measurable sets $R \subset \mathbb{R}^3$ and $S \subset \mathbb{R} \times [0, 2\pi) \times [0, \infty)$ (provided that $\Phi(S) = R$) and for every continuous function $f: R \rightarrow \mathbb{R}$ to obtain

$$\int_R f(\mathbf{x}) \, d\mathbf{x} = \int_S f(\Phi(\mathbf{s})) \cdot r \, d\mathbf{s}. \quad (1.1.15)$$

Transforming vector field

A vector field $\mathbf{f} = (f_x, f_y, f_z)$ is transformed from Cartesian components to cylindrical components by

$$\begin{bmatrix} f_x \\ f_\varphi \\ f_r \end{bmatrix} = \begin{bmatrix} 1 & 0 & 0 \\ 0 & -\sin \varphi & \cos \varphi \\ 0 & \cos \varphi & \sin \varphi \end{bmatrix} \begin{bmatrix} f_x \\ f_y \\ f_z \end{bmatrix}. \quad (1.1.16)$$

The proof of this transformation will not be given.

Transforming Laplace operator

Let $f : \mathbb{R}^3 \rightarrow \mathbb{R}$ be a twice continuously differentiable function. The Laplace operator Δf is used to describe blood flow. Δf physically represents the diffusion of f . The Laplace operator is expressed in Cartesian coordinates as

$$\Delta f = \partial_x^2 f + \partial_y^2 f + \partial_z^2 f. \quad (1.1.17)$$

The Laplace operator is expressed in cylindrical coordinates as

$$\Delta f = \partial_x^2 f + \frac{1}{r^2} \partial_\varphi^2 f + \frac{1}{r} \partial_r (r \partial_r f). \quad (1.1.18)$$

1.2. Blood flow in three dimensions

Blood flow through arteries is considered a fluid-structure interaction (FSI) problem. As the name suggests, FSI consists of three parts, each of which will be discussed in their section. This section starts by discussing the movement of the vascular wall in Section 1.2.1, is followed by hemodynamics in Section 1.2.2, and ends with discussing the interactions between blood and the vascular wall in Section 1.2.3.

1.2.1. Deformations of vascular walls

In the introduction, we have already discussed the three different layers and their functions of the arterial wall, but we have not discussed how the deformations of the walls are modeled. The arterial wall's deformation, or strain, depends on the amount of stress exerted on it.

Strain (ε) is the relative displacement, with respect to its reference configuration, a material undergoes while deforming. Stress (σ) is the intensity of the force applied across an area. In some deformation models applied to vascular walls, stress is related with the absolute displacement such that the total radius of the vascular wall can be rewritten as $R(t, \mathbf{x}) = R_0(\mathbf{x}) + \eta(t, \mathbf{x})$, where R_0 is the radius in reference configuration, η is the absolute displacement and R is the internal radius [3], [19]. For an in-depth explanation of strains and stresses, see [16, ch. 4].

Deformation models used within blood flow can be generalized by solid elastic models and viscoelastic models. Viscoelastic models are dynamic models in which the duration that a certain force is applied to the vascular walls affects how the wall will be deformed. The Kelvin-Voigt model is a viscoelastic model, which is suggested to be applied to model deformations of the arterial wall [22] and is used in [3] to compute the displacement of the arterial wall in their 2D axially symmetric model.

In solid elastic models, such as the linear elastic model, strains and stresses are related by a function. However, linear elasticity models can only be applied if the strains a material undergoes are small. In a general setting, stress and strain are related in a linear elastic model as

$$\sigma_{ij} = -\lambda(\varepsilon_{11} + \varepsilon_{22} + \varepsilon_{33})\delta_{ij} + 2G\varepsilon_{ij} \quad (1.2.1)$$

where the δ_{ij} is the Kronicker delta, λ is the bulk modulus of the material and G is the shear modulus of the material [22]. The bulk and shear modulus of a material are computed as [16],

$$G = \frac{E}{2(1+\nu)} \text{ and} \quad (1.2.2)$$

$$\lambda = \frac{E}{3(1-2\nu)} \quad (1.2.3)$$

where ν is the material's Poisson ratio and E is the material's Young's elastic modulus.

1.2.2. Hemodynamics

The fluid part of FSI covers hemodynamics, the study of blood flow. Blood is very complicated. Its rheology is still being researched. This section mainly follows van Groesen's book [27].¹

¹Van Groesen's explanation is followed with the adjustment that the walls surrounding the fluid are not rigid.

Fluid flow within a medium can be obtained by satisfying the conservation of mass and balance of momentum equations. Both equations are derived from the transport equation

$$\frac{d}{dt} \int_{V(t)} \mathbf{f}(t, \mathbf{x}) d\mathbf{x} = - \int_{\partial V(t)} \mathbf{Q} \cdot \mathbf{n} d\mathbf{x} + \int_{V(t)} S d\mathbf{x}, \quad (1.2.4)$$

where $V \subset \mathbb{R}^3$ is the volume element which changes in time, ∂V is the boundary of V , \mathbf{f} is the density of some property, \mathbf{Q} is the flux density corresponding to \mathbf{f} , \mathbf{n} is the outwards pointing normal vector, and S corresponds to sources and sinks. The conservation of mass equation is obtained by taking the density of blood (ρ) as \mathbf{f} , momentum ($\rho\mathbf{v}$) as \mathbf{Q} , and no sources and sinks, which by incorporating Gauss's divergence theorem leads to

$$\partial_t \int_{V(t)} \rho d\mathbf{x} + \int_{V(t)} \nabla \cdot (\rho\mathbf{v}) d\mathbf{x} = 0, \quad (1.2.5)$$

where \mathbf{v} is the velocity of blood. The balance of momentum equation is obtained by taking momentum ($\rho\mathbf{v}$) as \mathbf{f} , by taking the dyadic product $\rho(\mathbf{v} \otimes \mathbf{v})$ as \mathbf{Q} , and by taking stresses exerted on the fluid within V as sources and sinks. The dyadic product has the identities $(\mathbf{v} \otimes \mathbf{v})_{ij} = v_i v_j$ and

$$\nabla \cdot (\mathbf{v} \otimes \mathbf{v}) = \mathbf{v}(\nabla \cdot \mathbf{v}) + \nabla \mathbf{v} \cdot \mathbf{v}. \quad (1.2.6)$$

There are two different stresses exerted on the fluid. These are body forces \mathbf{f}_b , typically due to gravity for blood flow, and contact forces \mathbf{f}_c , generated from stress acting on the arterial wall. Body forces are generally omitted in hemodynamics. Contact forces are split into isotropic stress $-pI$, where p is the hydrostatic pressure and I is the identity matrix, and extra stress σ^e , which is computed as

$$\sigma^e = \nabla \cdot (\mu(\nabla \mathbf{v} + (\nabla \mathbf{v})^T)) \quad (1.2.7)$$

where μ is the viscosity of blood. The balance of momentum equation becomes

$$\partial_t \int_{V(t)} \rho\mathbf{v} d\mathbf{x} + \int_{V(t)} \rho\mathbf{v}(\nabla \cdot \mathbf{v}) + \rho\nabla \mathbf{v} \cdot \mathbf{v} d\mathbf{x} = \int_{V(t)} \nabla \cdot (\mu(\nabla \mathbf{v} + (\nabla \mathbf{v})^T)) - \nabla p d\mathbf{x}. \quad (1.2.8)$$

Hemorheology shows that blood is a shear-thinning (pseudoplastic) fluid, a non-Newtonian fluid in which shear stress decreases exponentially with increasing shear rates. However the non-Newtonian properties of blood are only noticeable in micro-circulation where the internal tube diameter is smaller than 1000 μm [6], [16]. Our research will be limited to flow in arteries whose diameters exceed 1000 μm . So, blood is considered as a Newtonian fluid within this study.

1.2.3. Interface conditions

The last part of the FSI problem is coupling the blood flow and the artery's movement with interface (or coupling) conditions. According to Canic et al. [3], there are two coupling conditions applied to FSI for blood flow, which are known as *kinematic* coupling condition and *dynamic* coupling condition. Kinematic coupling condition satisfies the continuity of velocity, where the fluid velocity adjacent to the inner wall is equal to the movement of the inner wall. Dynamic coupling condition satisfies the balance of contact forces, i.e., the contact forces exerted by blood are balanced with the contact forces exerted by the inner wall.

1.3. Reduced order modeling

Reduced order modeling decreases the computational complexity of a model by removing dimensions within a model. In hemodynamics, reduced order modeling has been applied to reduce blood flow into 1D and 2D axially symmetric models. Many papers describe different methods to obtain a 1D reduced order model (ROM) for blood flow. This study mainly refers to Quarteroni and Formaggia's paper [18] for the 1D ROM since they clearly state their assumptions. Their 1D ROM is a fluid-structure interaction model in which the radial and azimuthal dimensions have been removed from the three-dimensional model.

This section discusses the general idea regarding reduced order modeling, proceeds with the assumptions used to obtain the 1D ROM, continues with the linear deformation model, and ends by discussing the 1D ROM for blood flow.

1.3.1. General idea regarding reduced order modeling

A couple of claims will be introduced before discussing the general idea of reduced order modeling. Let $\Omega = \Omega_R \times E \subseteq \mathbb{R}^d$, where Ω is the original dimension, $\Omega_R \subseteq \mathbb{R}^n$ is the reduced dimension, and $E \subseteq \mathbb{R}^{d-n}$ contain the dimensions which will be removed to obtain a reduced order model. Let $\mathbf{x} = (\mathbf{y}, \mathbf{z}) \in \Omega$ with $\mathbf{y} \in \Omega_R$ and $\mathbf{z} \in E$. Let D be a differential operator, $\mathbf{f}: \Omega \rightarrow \mathbb{R}$ be a sufficiently smooth vector function such that $D[\mathbf{f}] \in L^1(K)$ for every compact set $K \subset \Omega$, and let for all test functions $\phi \in C_c^\infty(\Omega)$

$$\int_{\Omega} \phi D[\mathbf{f}] dx = 0. \quad (1.3.1)$$

The fundamental lemma of variational calculus can be applied to obtain $D[\mathbf{f}] = 0$.

The general idea regarding reducing a model is to restrict the test functions to

$$\phi(\mathbf{x}) = \phi_R(\mathbf{y}), \quad (1.3.2)$$

where $\phi_R \in C_c^\infty(\Omega_R)$. With the restricted test functions, equation (1.3.1) is reduced into

$$\int_{\Omega} \phi D[\mathbf{f}] dx = \int_{\Omega_R} \left(\int_E D[\mathbf{f}] dz \right) \phi_R d\mathbf{y} = \int_{\Omega_R} \phi_R D_R[\mathbf{f}_R] d\mathbf{y} = 0, \quad (1.3.3)$$

where $D_R = \int_E D[\mathbf{f}] dz$ is the differential operator for the reduced model and \mathbf{f}_R is a reduced vector function. Additional assumptions are necessary to relate \mathbf{f}_R to \mathbf{f} to ensure that $D_R[\mathbf{f}_R] \in L^1(K_R)$ for every compact set $K_R \subset \Omega_R$. After these assumptions are applied, the fundamental lemma of variational calculus can be applied in equation (1.3.3) to obtain $D_R[\mathbf{f}_R] = 0$. In summary, one must integrate $D[\mathbf{f}]$ over E and apply meaningful assumptions to obtain a ROM.

1.3.2. Assumptions 1D blood flow

Quarteroni and Formaggia use the following assumptions to obtain the 1D ROM for blood flow [18].

Assumption 1 *Axial symmetry.*

All quantities are independent of the angular coordinate φ .

Assumption 2 *Radial displacement.*

The walls of the arteries only change along the radial coordinate r .

Assumption 3 *Constant pressure.*

Pressure is constant within a cross-section. Thus, it will only depend on longitudinal coordinate x and time.

Assumption 4 *No body forces.*

The inclusion of gravity will be neglected.

Assumption 5 *Dominance in axial velocity.*

The velocity components orthogonal to the axial component x are neglected. With $\mathbf{v} = (v_x, v_\varphi, v_r)$ the velocity in 3D, we have that

$$v_x(t, x, \varphi, r) = u(t, x) s \left(\frac{r}{R(t, x)} \right) \quad (1.3.4)$$

in which u is the mean velocity in its cross-section and $s \in C^2([0, 1])$ is the velocity profile which satisfies

$$s(1) = 0, \quad (1.3.5)$$

$$\int_0^1 y s(y) dy = \frac{1}{2}. \quad (1.3.6)$$

Property (1.3.5) reflects the no-slip boundary condition, which, in conjunction with Assumption 2 (radial displacement), satisfies the kinematic coupling condition. Property (1.3.6) ensures that the measure is normalized. The velocity profile $s(y) = \frac{\gamma+2}{\gamma} (1 - y^\gamma)$ is used to reduce axial velocity, where γ is a strictly positive dimensionless variable which influences the shape of the velocity profile. γ is determined in advanced. $\gamma = 9$ is used to study 1D ROMs in [18] and [25] while a flat velocity profile is used

to study inviscid flow in $(\gamma \rightarrow \infty)$ in [28] and [23]. Some 1D ROM also impose the viscous axisymmetric flow [25]

$$\partial_r v_x|_{r=0} = 0, \quad (1.3.7)$$

which is satisfied for $\gamma > 1$.

Assumption 6 *Neglect the derivative w.r.t. the axial coordinate for the viscous term.*

The variation of v_x along the axial direction is small compared to the other terms. This assumption is not listed by Quarteroni and Formaggia but is applied to obtain their 1D ROM while deriving the viscous terms.

1.3.3. Linear elastic deformation model

Applying the linear elastic model to the walls of homogeneous, incompressible, isotropic, and longitudinally tethered arteries (tethered so that the artery cannot move longitudinally) leads to thin-wall or thick-wall theorems. The thin-wall model can be obtained by balancing the tension generated inside the wall with the stress exerted on its surfaces, which leads to the law of Laplace [22]

$$T = PR \quad (1.3.8)$$

where T is the tension, P is the pressure and R is the inner wall radius. The thin wall model is described as

$$\eta_r = \frac{3 \Delta P R^2}{4 E h}, \quad (1.3.9)$$

where η_r is the absolute displacement, $\Delta P = P_i - P_o$ is the pressure difference between pressure at the inner wall (P_i) and pressure at the outer wall (P_o), R is the vessel radius and h is the thickness of the wall [22]. The thin-wall model is used in papers such as [28] and [23], and will also be applied to the 2D ROM due to its simplicity.

1.3.4. 1D reduced order model for blood flow

The conservation of mass (1.2.5) and balance of momentum (1.2.8) equations in 3D are not in the form denoted in equation (1.3.1), the derivative ∂_t is in front of some integrals. By incorporating the assumption denoted in section 1.3.2 in conjunction with Reynolds transport theorem, Quarteroni and Formaggia obtain the integral form (or strong form) of the reduced mass and momentum equations

$$\int_I (\partial_t A + \partial_x Q) \phi dx = 0, \quad (1.3.10)$$

$$\int_I \left(\partial_t Q + \alpha \partial_x \left(\frac{Q^2}{A} \right) + \frac{A}{\rho} \partial_x P + K_r \frac{Q}{A} \right) \phi dx = 0, \quad (1.3.11)$$

where $I = [0, L]$, in which L is the length of an artery, $A = \pi R^2$ is the cross-section area, $Q = uA$ is the flow rate, $\alpha = \int_0^1 y s^2(y) dy = \frac{\gamma+2}{\gamma+1}$ is known as a momentum-flux correction term, $K_r = -2\pi \frac{\mu}{\rho} s'(1)$ is a friction parameter, P is the pressure within the cross-section and ϕ is a test function. The integral forms of the reduced mass and momentum equations are not satisfied for all test functions $\phi \in C_c^\infty(I)$, but for test functions of the form $\phi = \mathbb{1}_{[x_1, x_2]}(x)$, where $[x_1, x_2] \subset I$ and

$$\mathbb{1}_S(x) = \begin{cases} 1 & \text{for } x \in S, \\ 0 & \text{for } x \notin S. \end{cases} \quad (1.3.12)$$

Consequently, the fundamental lemma of variational calculus cannot be applied to obtain the differential form of the reduced mass and momentum equations. But by applying the mean value theorem, Quarteroni and Formaggia obtain the differential form of the reduced mass and momentum equation, depicted as

$$\partial_t A + \partial_x Q = 0, \quad (1.3.13)$$

$$\partial_t Q + \alpha \partial_x \left(\frac{Q^2}{A} \right) + \frac{A}{\rho} \partial_x P + K_r \frac{Q}{A} = 0. \quad (1.3.14)$$

Pressure is obtained from the vascular wall's deformation model. Quarteroni and Formaggia derive their own viscoelastic model. A linear elastic deformation model can be obtained from their viscoelastic model by

eliminating all derivatives from their model, which yields

$$P = P_0 + \frac{\sqrt{A} - \sqrt{A_0}}{A_0} \beta \quad (1.3.15)$$

where

$$\beta = \frac{4}{3} \sqrt{\pi} E h \quad (1.3.16)$$

is contains the mechanical properties of the wall. The linear elastic deformation model is identical to the thin-wall model denoted in (1.3.9) by substituting $P = P_i$, $P_0 = P_o$, $\sqrt{A} - \sqrt{A_0} = \sqrt{\pi} \eta_r$ and $A_0 = \pi R^2$. Substituting (1.3.15) into (1.3.14), leads to the momentum of balance equation [18]

$$\partial_t Q + \partial_x \left(\alpha \frac{Q^2}{A} + \frac{\beta}{3\rho A_0} A^{3/2} \right) + K_r \frac{Q}{A} = 0. \quad (1.3.17)$$

Quarteroni and Formaggia also performed characteristic analysis. Blood flow in 1D can be rewritten in the quasi-linear form

$$\partial_t \mathbf{q} + H(\mathbf{q}) \partial_x \mathbf{q} + S(\mathbf{q}) = 0 \quad (1.3.18)$$

where

$$\mathbf{q} = \begin{bmatrix} A \\ Q \end{bmatrix}, \quad (1.3.19)$$

$$H = \begin{bmatrix} 0 & 1 \\ \frac{\beta\sqrt{A}}{2\rho A_0} - \alpha \left(\frac{Q}{A}\right)^2 & 2\alpha \frac{Q}{A} \end{bmatrix}, \text{ and} \quad (1.3.20)$$

$$S = \begin{bmatrix} 0 \\ K_r \frac{Q}{A} \end{bmatrix}. \quad (1.3.21)$$

In their studies, they showed that H has real eigenvalues computed as

$$\lambda_{\pm} = \alpha \frac{Q}{A} \pm \sqrt{\frac{\beta\sqrt{A}}{2\rho A_0} + \frac{Q^2}{A^2} \alpha(\alpha - 1)}. \quad (1.3.22)$$

Blood flow under physiological configurations is sub-critical, i.e., $\lambda_1 < 0 < \lambda_2$. This indicates that one boundary condition will be applied at the inlet and the outlet. Quarteroni and Formaggia specify pressure at the inlet and the non-reflective boundary condition [18]

$$\mathbf{l}_1(\mathbf{q}_{out}) (\partial_t \mathbf{q}_{out} + S(\mathbf{q}_{out})) = 0 \quad (1.3.23)$$

at the outlet. Both area and flow rate must be defined on each boundary to develop numerical methods. This is done by incorporating compatibility conditions, defined in [18] as

$$\mathbf{l}_1(\mathbf{q}) (\partial_t \mathbf{q} + H(\mathbf{q}) \partial_x \mathbf{q} + S(\mathbf{q})) = 0 \quad \text{for } x = 0, \quad (1.3.24)$$

$$\mathbf{l}_2(\mathbf{q}) (\partial_t \mathbf{q} + H(\mathbf{q}) \partial_x \mathbf{q} + S(\mathbf{q})) = 0 \quad \text{for } x = L, \quad (1.3.25)$$

where \mathbf{l}_p is the left eigenvector corresponding to λ_p .

1.4. Finite volume methods for hyperbolic equations

Finite volume methods are well-known numerical methods that can simulate systems of non-linear hyperbolic equations. Finite volume methods are obtained by discretizing the domain in finite control volumes (or cells) and updating cell averages based on fluxes at cell interfaces. This section summarizes key concepts about finite volume methods discussed by Leveque [12] to develop numerical methods for blood flow in 1D and 2D.

1.4.1. Godunov method for one dimension

The Godunov method is a well-known method to develop finite volume methods for conservative equations. The Godunov method comes in the three stages *reconstruct*, *evolve*, *average* [12, p. 76].

Reconstruct

The Godunov method begins with the reconstruction stage. In this stage, a piecewise polynomial function will be reconstructed from the cell averages. We will mainly focus on reconstructing cell averages into piecewise constant functions, leading to an upwind method.

Evolve

The second stage of the Godunov method is the evolution stage. In this stage, the hyperbolic equation will be simulated using the piecewise polynomial function as initial data to obtain a solution after a certain duration. Simulating piecewise constant functions leads to solving Riemann problems at each cell interface. A Riemann problem at the cell interface located at $x = x_i$ is denoted as

$$\partial_t \mathbf{q} + H(\mathbf{q}) \partial_x \mathbf{q} = 0, \quad \begin{cases} \mathbf{q} = \mathbf{q}_l & \text{for } x < x_i, \\ \mathbf{q} = \mathbf{q}_r & \text{for } x > x_i, \end{cases} \quad (1.4.1)$$

where $\mathbf{q} \in \mathbb{R}^m$ is a vector function and $A \in \mathbb{R}^{m \times m}$ is a flux function.

Average The Godunov method ends with the averaging stage, in which cell averages will be obtained from the simulated solution.

1.4.2. 1D Riemann problem for linear hyperbolic equation

Solutions to equation (1.4.1) for a linear hyperbolic system are mainly piecewise constant, where the location of the discontinuities are propagated from the discontinuity in the initial solution. Propagations of these discontinuities are known as *shock waves*. The speed of the shock waves depends on the eigenvalues of H . Riemann solutions to an $m \times m$ system of linear hyperbolic equations yield $m + 1$ states and m shock waves if the system is strictly hyperbolic. A linear system is strictly hyperbolic if all eigenvalues are real and distinct.

Solutions to the Riemann problem for a strictly linear hyperbolic system are well known. The jump $\mathbf{q}_r - \mathbf{q}_l$ can be decomposed into the eigenvectors of A . This is done by finding a vector $\mathbf{a} \in \mathbb{R}^m$ that satisfies

$$R\mathbf{a} = \mathbf{q}_r - \mathbf{q}_l, \quad (1.4.2)$$

where R contains eigenvectors of H . The jump across the p th shock wave \mathcal{W}^p is equal to

$$\mathcal{W}^p = \mathbf{a}^p \mathbf{r}^p, \quad (1.4.3)$$

where \mathbf{r}^p is the eigenvector corresponding to λ^p . Once all of the jumps are known, the solution to the Riemann problem is evaluated as

$$\mathbf{q}(t, x) = \mathbf{q}_l + \sum_{p=1}^m H_p(x - \lambda^p t) \mathcal{W}^p \quad (1.4.4)$$

where $H_p(x)$ is the Heaviside function

$$H_p(x) = \begin{cases} 1 & \text{for } x > 0, \\ 0 & \text{for } x < 0. \end{cases} \quad (1.4.5)$$

1.4.3. 1D Riemann problem for non-linear hyperbolic equation

Blood flow for the 1D ROM is a non-linear system of hyperbolic equations. Applying Godunov's method for the 1D ROM leads to solving Riemann problems for a 2×2 system of non-linear hyperbolic equations. Solving non-linear Riemann problems is much more complicated than solving its linear counterpart, and its computational complexity is also higher. For a non-linear Riemann problem, each state is separated between either shock waves and *rarefaction waves*. A rarefaction wave leads to a continuous transition between two states. Solving a non-linear Riemann problem analytically is out of the scope of this master's thesis. Toro and Siviglia have studied analytical solutions for blood flow in 1D with discontinuous mechanical properties [26], and high-order numerical methods for a similar problem have been developed by Pimentel-García et al. [17].

Additionally, Riemann problems for non-linear hyperbolic equations can be solved approximately, which are known as *approximate Riemann solvers*. Approximate Riemann solvers linearizes the matrix $H(\mathbf{q})$ into \hat{H} and compute jumps across shock waves as denoted in section 1.4.2. Linearized Riemann solvers are easier to solve than the analytical solution, and their computational complexity is also lower. The drawback is that the approximated Riemann solver might not yield physically correct waves.

For the remainder of this section, we will assume that a compact form exists for the Riemann problem. That is, there exist a flux-function $\mathbf{f}: \mathbb{R}^m \mapsto \mathbb{R}^m$ such that the Riemann problem (1.4.1) is identical to

$$\partial_t \mathbf{q} + \partial_x \mathbf{f}(\mathbf{q}) = 0, \quad \begin{cases} \mathbf{q} = \mathbf{q}_l & \text{for } x < x_i, \\ \mathbf{q} = \mathbf{q}_r & \text{for } x > x_i. \end{cases} \quad (1.4.6)$$

According to Leveque, the linearized Riemann solver has to satisfy the conditions

- 1) \hat{H} is diagonalizable with real eigenvalues,
- 2) $\hat{H} \rightarrow \mathbf{f}'(\mathbf{q}_l)$ as $\|\mathbf{q}_l - \mathbf{q}_r\| \rightarrow 0$.

The first condition is important such that the approximated Riemann problem

$$\partial_t \mathbf{q} + \hat{H} \partial_x \mathbf{q} = 0, \quad \begin{cases} \mathbf{q} = \mathbf{q}_l & \text{for } x < x_i, \\ \mathbf{q} = \mathbf{q}_r & \text{for } x > x_i, \end{cases} \quad (1.4.7)$$

remains hyperbolic, whereas the second condition ensures that the linearized Riemann problem is consistent with (1.4.6) if \mathbf{q} is continuous. To ensure that the linearized Riemann solver is conservative, the linearized matrix \hat{H} needs to satisfy

$$\hat{H}(\mathbf{q}_r - \mathbf{q}_l) = \mathbf{f}(\mathbf{q}_r) - \mathbf{f}(\mathbf{q}_l). \quad (1.4.8)$$

An easy-to-implement linearized Riemann solver is to apply the simple linearization

$$\hat{H} = \mathbf{f}'(\hat{\mathbf{q}}), \quad \text{where } \hat{\mathbf{q}} = \frac{\mathbf{q}_r + \mathbf{q}_l}{2}. \quad (1.4.9)$$

Condition 2) is always satisfied for the simple linearization, whereas condition 1) depends on the flux function \mathbf{f} . The simple linearization denoted in (1.4.9) does not always satisfy (1.4.8).

Roe's linearization is a linearization technique that satisfies (1.4.8) and can yield easy-to-compute linearization. Roe originally developed this technique to linearize the Euler equations [21]. This is done by introducing an invertible parametrization vector $\mathbf{z}(\mathbf{q})$ and by introducing the parametrization

$$\mathbf{w}(\xi) = \mathbf{z}(\mathbf{q}_l) + (\mathbf{z}(\mathbf{q}_r) - \mathbf{z}(\mathbf{q}_l))\xi.$$

Remark that flux function \mathbf{f} can be expressed by \mathbf{z} as $\mathbf{f}(\mathbf{q}(\mathbf{z}))$. With these parametrizations, Leveque shows that [12]

$$\mathbf{f}(\mathbf{q}_r) - \mathbf{f}(\mathbf{q}_l) = \mathbf{f}(\mathbf{q}(\mathbf{w}(1))) - \mathbf{f}(\mathbf{q}(\mathbf{w}(0))) = \hat{C}(\mathbf{z}(\mathbf{q}_r) - \mathbf{z}(\mathbf{q}_l)), \quad (1.4.10)$$

where $\hat{C} = \int_0^1 \mathbf{f}'(\mathbf{z}(\xi)) d\xi$, and

$$\mathbf{q}_r - \mathbf{q}_l = \mathbf{q}(\mathbf{w}(1)) - \mathbf{q}(\mathbf{w}(0)) = \hat{B}(\mathbf{z}(\mathbf{q}_r) - \mathbf{z}(\mathbf{q}_l)). \quad (1.4.11)$$

where $\hat{B} = \int_0^1 \mathbf{q}'(\mathbf{z}(\xi)) d\xi$. If \hat{B} is invertible, we can show from equations (1.4.10) and (1.4.11) that equation (1.4.8) is satisfied if

$$\hat{H} = \hat{C} \hat{B}^{-1} \quad (1.4.12)$$

The challenge to incorporate this linearization is finding an invertible parametrization vector $\mathbf{z}(\mathbf{q})$ for the flux function \mathbf{f} .

1.4.4. 1D Numerical schemes for hyperbolic equations

This section discusses three well known numerical schemes: the upwind method, second-order accurate methods, and high-resolution methods. This section assumes that H is a 2x2 matrix and that $\lambda_1 < 0 < \lambda_2$.

Upwind method

By developing numerical methods based on the Godunov method described in 1.4.1, cell averages are updated as [12]

$$\mathbf{q}_i^{n+1} = \mathbf{q}_i^n - \frac{\Delta t}{\Delta x} (\mathcal{A}_{i-1/2}^+ + \mathcal{A}_{i+1/2}^-), \quad (1.4.13)$$

where

$$\mathcal{A}_{i-1/2}^+ = \lambda^2 \mathcal{W}_{i-1/2}^2 \text{ and } \mathcal{A}_{i+1/2}^- = \lambda^1 \mathcal{W}_{i+1/2}^1 \quad (1.4.14)$$

are known as *fluctuations*. Fluctuations can be seen as how much the cell averages change due to the fluxes at adjacent cell interfaces. The numerical scheme denoted in (1.4.13) is known as the upwind method and is first-order accurate. The leading order error of first-order accurate methods leads to numerical diffusion.

Second-order accurate methods

According to Leveque, applying a piecewise linear reconstruction to the Godunov's method yields second-order numerical schemes. One of those numerical schemes is known as the *Lax-Wendroff method*. The numerical scheme for the Lax Wendroff method can also be obtained with \mathcal{W}^p obtained from either the linear Riemann problem or by applying the approximated Riemann solver to the non-linear Riemann problem. Second-order numerical schemes can be described as

$$\mathbf{q}_i^{n+1} = \mathbf{q}_i^n - \frac{\Delta t}{\Delta x} (\mathcal{A}_{i-1/2}^+ + \mathcal{A}_{i+1/2}^-) - \frac{\Delta t}{\Delta x} (F_{i+1/2} - F_{i-1/2}), \quad (1.4.15)$$

where $F_{i+1/2}$ is a higher-order correction term. The Lax-Wendroff method has the following higher-order correction term [12]

$$F_{i+1/2} = \frac{1}{2} \sum_{p=1}^2 |\lambda_{i+1/2}^p| \left(1 - \frac{\Delta t}{\Delta x} |\lambda_{i+1/2}^p| \right) \mathcal{W}_{i+1/2}^p. \quad (1.4.16)$$

The leading order error of the Lax-Wendroff methods leads to numerical dispersion. Numerical dispersion can lead to oscillatory behavior and waves lagging behind the analytical solution.

High-resolution method

The idea behind high-resolution methods is to apply a high-order accurate method while using the low-order accurate method, where the dispersive error from the second-order accurate method is expected to be significant. Effectively, the high-order accurate method are limited by incorporating a limiter function, hence

$$\tilde{F}_{i+1/2} = \frac{1}{2} \sum_{p=1}^2 |\lambda_{i+1/2}^p| \left(1 - \frac{\Delta t}{\Delta x} |\lambda_{i+1/2}^p| \right) \mathcal{W}_{i+1/2}^p \phi(\theta_{i+1/2}^p), \quad (1.4.17)$$

where $\tilde{F}_{i+1/2}$ is the limited second order correction term, ϕ is a limiter function and $\theta_{i+1/2}^p$ influences how much each wave is limited. There are many limiter functions available, such as the van Leer limiter

$$\phi = \frac{\theta + |\theta|}{1 + |\theta|}. \quad (1.4.18)$$

How much the wave $\mathcal{W}_{i+1/2}^p$ should be limited depends on the magnitude and the direction of the wave behind it. For the linear case, $\theta_{i+1/2}^p$ is computed as

$$\theta_{i+1/2}^p = \frac{a_I^p}{a_i^p}, \quad I = \begin{cases} i-1 & \text{if } \lambda_{i+1/2}^p > 0, \\ i+1 & \text{if } \lambda_{i+1/2}^p < 0, \end{cases} \quad (1.4.19)$$

where $a_{i+1/2}^p$ is the magnitude of wave $\mathcal{W}_{i+1/2}^p$. For a non-linear hyperbolic problem, one also needs to take care of the direction of the eigenvectors since the eigenvectors $\mathbf{r}_{i+1/2}^p$ and $\mathbf{r}_{I+1/2}^p$ do not have to be collinear. This can be done by projecting the wave $\mathcal{W}_{i+1/2}^p$ onto the wave $\mathcal{W}_{I+1/2}^p$, thus

$$\theta_{i+1/2}^p = \frac{\mathcal{W}_{i+1/2}^p \cdot \mathcal{W}_{I+1/2}^p}{\mathcal{W}_{i+1/2}^p \cdot \mathcal{W}_{i+1/2}^p}, \quad I = \begin{cases} i-1 & \text{if } \lambda_{i+1/2}^p > 0, \\ i+1 & \text{if } \lambda_{i+1/2}^p < 0. \end{cases} \quad (1.4.20)$$

For more in-depth information about limiters and high-resolution methods, readers are advised to read [12].

1.4.5. Finite volume methods for higher dimensions

Different strategies exist to develop finite volume methods for two (or higher) dimensions. Three methods discussed by Leveque are [12][ch 19]:

Fully discrete flux-differencing methods

Similar to flux-differencing methods discussed in section 1.4.1, fluxes will be determined for all cell interfaces. Cell averages for a new timestep can be obtained by differencing the fluxes based on Taylor approximations.

Semidiscrete methods

For semidiscrete methods, the multidimensional problem will be turned into a system of ordinary differential equations (ODEs). Each ODE is solved numerically by a high-order accurate method, such as the Runge-Kutta method.

Dimensional splitting

For dimensional splitting, the multidimensional problem is split into sequences of sub-problems for a single time step. Usually, each sub-problem only deals with one dimension of the multi-dimensional problem. This splitting procedure can lead to a splitting error.

Splitting error

In dimensional splitting, the order of the splitting error depends on the splitting procedure and whether sub-problems *commute* or not. Splitting a problem into two subsequent sub-problems does not yield an error if these sub-problems commute. Two subsequent sub-problems commute if the order of solving the subsequent sub-problems does not influence the solution.

Godunov splitting and Strang splitting are two well-known splitting procedures to split a problem into two sub-problems [12][ch. 17]. For a Godunov splitting procedure, all sub-problems will be solved sequentially in a specific order. The Strang splitting procedure is more complicated, which leads to a higher computational complexity than the Godunov splitting procedure. According to Leveque [12], Godunov splitting is first-order accurate $\mathcal{O}(\Delta x)$ whereas Strang splitting is second-order accurate if the two sub-problems do not commute.

2

Method

This section will discuss the first two main research questions, which concern the mathematical expressions and numerical methods for the 2D ROM, while making preparations to discuss the last main research question, which concerns comparing the 2D and 3D simulations. This section explains the problem within a three-dimensional framework in Section 2.1 to discuss these research questions. This problem will be discussed in a two-dimensional framework in Section 2.2 to discuss the first two research questions. The finite element software package FEBIO used to obtain simulations in three-dimensions is discussed in Section 2.3 in preparation to discuss the last research question.

2.1. Problem description

This study focuses on blood flow within a longitudinal tethered artery without curvature and bifurcations, i.e. branching of arteries. Cylindrical coordinates will be used to describe the geometry of the artery (see Figure 2.1). The domain where blood flows within the artery in three dimensions is defined as $\Omega^{3D}(t) = (x_{in}, x_{out}) \times (0, 2\pi) \times (0, R(t, x, \varphi))$, where $R : [0, \infty) \times [x_{in}, x_{out}] \times [0, 2\pi] \rightarrow (0, \infty)$ is the inner wall radius. Blood flow is governed by conservation of mass (1.2.5) and balance of momentum (1.2.8) equations. Blood is considered a Newtonian fluid with viscosity of 0.003 Pa·s and a density of 1.060 g/cm³ [16].

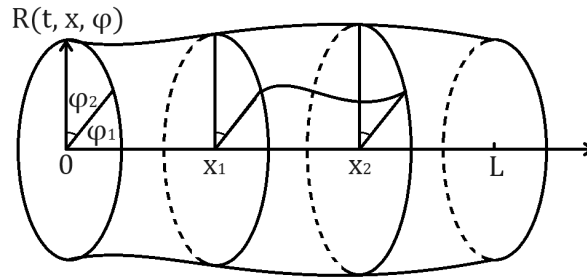


Figure 2.1: 3D representation of the domain without calcification where R is the inner wall radius.

The artery has a reference radius of 2.5 mm (reference radius of the internal carotid artery [4]), and the thickness of the vascular wall is 0.5 mm. The total length of the artery is chosen to be 15 mm. The elastic properties of the vascular walls are based on the study by Benitez et al. [1]. In their study, they performed a 3D simulation of the common carotid artery, in which the vascular walls were modeled as a linear elastic model. Tissues have a Poisson's ratio of 0.48. The healthy part of the artery has a Young's modulus of 0.6 MPa, while the calcified part has a Young's modulus of 10 MPa.

Two different sets of boundary conditions will be studied within this paper. Periodic boundary conditions will be prescribed for both sets of boundary conditions, i.e., all properties within blood flow are 2π -periodic on the azimuthal domain (e.g. $R|_{\varphi=0} = R|_{\varphi=2\pi}$). The first set of boundary conditions prescribes pressure at the inlet and applies a non-reflective boundary condition at the outlet (similar to (1.3.23)). This set of boundary

conditions lead to a non-physiological steady-state solution where blood flow vanishes (which will be covered in Section 2.2.5), and will mainly be used to study how accurate the numerical method for the 2D ROM obtains steady-state solutions.

The second set of boundary conditions represents blood flow that is more physiologically relevant on a longer time scale. This set of boundary conditions prescribes a parabolic velocity profile at the inlet and incorporates a fluid resistance boundary condition at the outlet. Figure 2.2, which is measured near the carotid bifurcation [7], depicts the velocity prescribed at the inlet. The diastolic mean axial velocity of 8.41199 cm/s will be prescribed at the inlet for researching steady-state solutions.

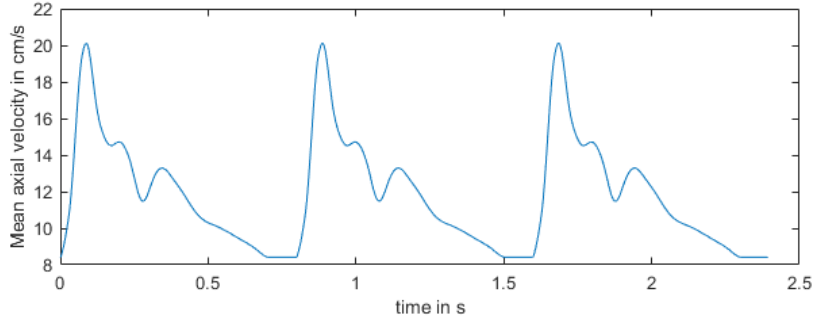


Figure 2.2: Mean axial velocity applied at the inlet for pulsatile flow.

The fluid resistance boundary condition is denoted as

$$P_{out} = P_{res} + Q_{out}R_{res} \quad (2.1.1)$$

where P_{out} is the pressure at the outlet, P_{res} is a pressure offset, Q_{out} is the flow rate at the outlet, and R_{res} is the flow resistance at the outlet. P_{res} and R_{res} are user defined parameters. The fluid resistance boundary condition will be used at the outlet because this boundary condition is one of the available boundary conditions in FEBio (which is used to simulate blood flow in 3D), and because values of P_{res} and R_{res} can be specified to match a predetermined pressure range. This study aims to match maximum and minimum pressure of 16.00 kPa (120 mm Hg) and 10.67 kPa (80 mmHg) respectively, representing systolic and diastolic blood pressure within a healthy artery.

2.2. 2D Reduced order model

For the two-dimensional reduced-order model (ROM), the dimension corresponding to the radial distance r will be eliminated from the three-dimensional domain to obtain the two-dimensional model. As a consequence, the three-dimensional domain $\Omega^{3D}(t)$ and the two-dimensional domain Ω are related by $\Omega^{3D}(t) = \Omega \times (0, R(t, x, \varphi))$. The two-dimensional domain $\Omega = (x_{in}, x_{out}) \times (0, 2\pi)$ is a rectangular domain depicted in Figure 2.3. The 2D domain has the four boundaries, which are Γ_{in} , Γ_{out} , Γ_{w_1} and Γ_{w_2} . Γ_{in} represents the in-

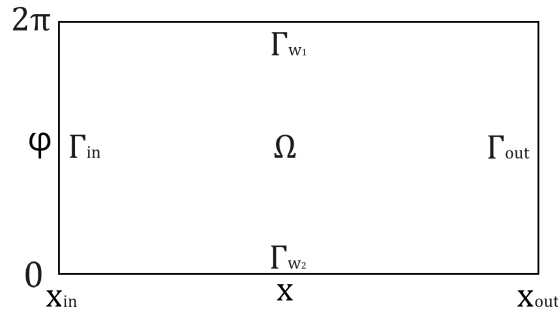


Figure 2.3: Domain of the 2D ROM

flow boundary, where blood enters the 2D domain, and Γ_{out} denotes the outflow boundary, where blood exits the 2D domain. Γ_{w_1} and Γ_{w_2} are connected by periodic boundary conditions, i.e., all properties within blood flow have the same value on Γ_{w_1} as in Γ_{w_2} (e.g. $R|_{\varphi=0} = R|_{2\pi}$).

The 2D ROM is discussed in five sections. Section 2.2.1 discusses the assumptions incorporated to obtain the 2D ROM. Two attempts are made to obtain the 2D ROM, referred to as the *axisymmetric flow model* and the *asymmetric flow model*. The first attempt is discussed in Section 2.2.2 and leads to an ill-posed model unless R becomes independent of φ , resulting in axial symmetry. The second attempt is discussed in Section 2.2.3, which allows a family of velocity profiles that eventually enables asymmetric flow. Section 2.2.4 discusses numerical methods for the 2D ROM in, and Section 2.2.5 ends with obtaining steady-state solutions for the 2D ROM.

2.2.1. Assumptions

The assumptions for the 2D ROM are almost identical to those for the 1D ROM defined in Section 1.3.2. The main difference will be that the assumption ‘axial symmetry’ will be replaced by a boundary condition. The assumptions applied to the 2D ROM are:

Assumption 1 *Radial displacement.*

The vascular walls can only be displaced radially over time. They have no longitudinal or circumferential motion.

Assumption 2 *Linear elastic deformation model.*

Pressure is obtained from the 1D deformation model:

$$P = P_0 + \frac{R - R_0}{R_0^2} \beta \quad (2.2.1)$$

where P is the pressure at the inner wall, P_0 is pressure at the outer wall, R_0 is the reference radius and $\beta = \frac{4}{3} Eh$, in which E is the artery’s Young’s elastic modulus and h is the wall thickness. P_0 is set to 0 Pa within this study. This model is derived from the linear elastic deformation model (1.3.15) applied in the 1D ROM by substituting $A = \pi R^2$ and $A_0 = \pi R_0^2$. Remark that a 1D model is applied in a two-dimensional setting, hence some terms are neglected. The relevance of these neglected terms are unknown in a 2D framework.

Assumption 3 *No body forces.*

The inclusion of gravity will be neglected.

Assumption 4 *Dominance in axial velocity.*

The velocity components orthogonal to the axial component ‘ x ’ are neglected under the assumption that the axial velocity is much larger than its orthogonal components. With $\mathbf{v} = (v_x, v_\varphi, v_r)$ the velocity of blood in 3D, the axial velocity is reduced as

$$v_x(t, x, \varphi, r) = u(t, x, \varphi) s\left(\frac{r}{R(t, x, \varphi)}\right) \quad (2.2.2)$$

in which u is the mean velocity and $s : [0, 1] \rightarrow [0, \infty)$ is the velocity profile mapped as

$$s(y) = \frac{\gamma + 2}{\gamma} (1 - y^\gamma), \quad (2.2.3)$$

where $\gamma > 0$ is chosen in advance. This velocity profile is used in the 1D ROM and satisfies the properties

$$s(1) = 0, \quad (1.3.5)$$

$$\int_0^1 y s(y) dy = \frac{1}{2}. \quad (1.3.6)$$

γ influences the shape of the velocity profile. $\gamma = 2$ represents Poiseuille flow whereas $\gamma = 9$ is used for the viscous term in large arteries [18]. Velocity profiles for $\gamma = 2$ and $\gamma = 9$ are shown in Figure 2.4. Velocity profiles within blood flow change over time. However, the velocity profiles are constant within 1D ROMs. This study aims for velocity profiles close to $\gamma = 2$, as $\gamma = 2$ and $\gamma \rightarrow \infty$ are the only velocity

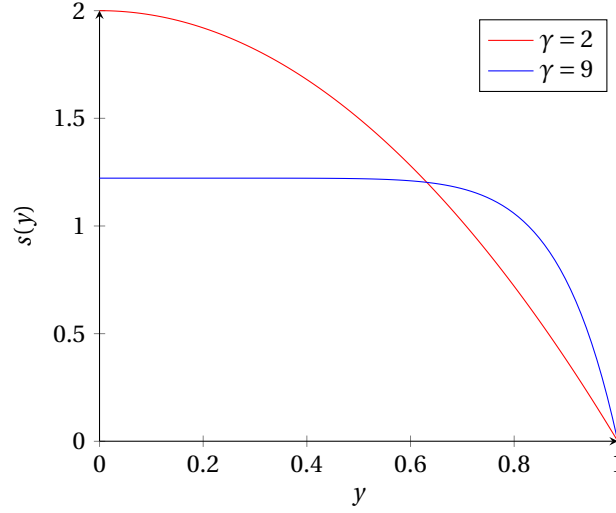


Figure 2.4: Velocity profiles for $\gamma = 2$ and $\gamma = 9$.

profiles prescribed in FEBio¹. $\gamma \rightarrow \infty$ can only be studied by neglecting the viscous source term, which will be included in this study.

Assumption 5 *Continuous axial velocity in a neighborhood near the artery's origin.*

One of the drawbacks of transforming cylindrical coordinates into Cartesian coordinates is that the mapping is not injective. Transforming cylindrical coordinates to Cartesian coordinates is done by the transformation function $\Phi(x, \varphi, r) = (x, r \cos \varphi, r \sin \varphi)$. This transformation is not injective since $\Phi(x, \varphi_1, 0) = \Phi(x, \varphi_2, 0)$ for $\varphi_1 \neq \varphi_2$. Hence, there are many ways to refer to the origin ($r = 0$) in cylindrical coordinates. Remark that the boundary $r = 0$ is an artificial boundary within the cylindrical coordinate system since radial distances are positive. The transformation from cylindrical coordinates to Cartesian coordinates yields physiological results by adding the boundary condition

$$\partial_\varphi v_x|_{r=0} = 0. \quad (2.2.4)$$

This boundary condition is referred to as the *continuity condition* since it ensures that axial velocity is continuous in a neighborhood near the artery's origin. The assumption 'axial symmetry' used in the 1D ROM automatically satisfies the continuity condition (2.2.4), whereas (2.2.4) does not always satisfy axial symmetry.

Assumption 6 *Neglect the derivative w.r.t. the axial coordinate for the viscous term.*

The variation of v_x along the axial direction is small compared to the other terms.

Importance of Assumption 5

As described in section 1.3.1, the 2D ROM can be obtained by integrating the conservation of mass and balance of momentum equation over $[0, R(t, x, \varphi)]$. Completely removing the assumption 'axial symmetry' from the 1D ROM introduces an integral to the momentum of balance equation (1.3.11), identical to

$$\int_0^R \frac{1}{r} \partial_\varphi^2 v_x dr. \quad (2.2.5)$$

This integral is unbounded if $\partial_\varphi^2 v_x|_{r=0} \neq 0$. This integral becomes bounded if $|\partial_\varphi^2 v_x|$ is asymptotic to $M r^k$ for strictly positive M and k in the neighborhood of $r = 0$, and if $\partial_\varphi^2 v_x$ is continuous. In this case, for $0 < \delta \ll$

¹It is technically possible to apply any velocity profile in FEBio by manually applying velocities to each node.

$\inf R(t, x, \varphi)$, there exists a $M > 0$ such that $|\partial_\varphi^2 v_x|$ is bounded by Mr^k for $r < \delta$. The integral

$$\begin{aligned} \int_0^R \frac{1}{r} \partial_\varphi^2 v_x dr &\leq \int_0^R \left| \frac{1}{r} \partial_\varphi^2 v_x \right| dr \\ &= \int_0^\delta \left| \frac{1}{r} \partial_\varphi^2 v_x \right| dr + \int_\delta^R \left| \frac{1}{r} \partial_\varphi^2 v_x \right| dr \\ &< \int_0^\delta Mr^{k-1} dr + \int_\delta^R \left| \frac{1}{r} \partial_\varphi^2 v_x \right| dr \\ &< \int_0^\delta Mr^{k-1} dr + \int_\delta^R \frac{1}{\delta} \left| \partial_\varphi^2 v_x \right| dr \\ &\leq \frac{M}{k} \delta^k + \frac{1}{\delta} \int_0^R \left| \partial_\varphi^2 v_x \right| dr \end{aligned}$$

is bounded since $|\partial_\varphi^2 v_x|$ is continuous. Integral (2.2.5) is unbounded if $|\partial_\varphi^2 v_x|$ is approximate to Mr^k for $M > 0$ and $k \leq 0$ in the neighborhood of $r = 0$. In this case, integral (2.2.5) is unbounded since for $0 < \delta \ll \inf R(t, x, \varphi)$ we have

$$\int_0^\delta Mr^{k-1} dr = \begin{cases} M(\ln \delta - \ln 0) \rightarrow \infty & \text{for } k = 0, \\ M(\delta^k - 0^k) \rightarrow \infty & \text{for } k < 0. \end{cases}$$

The approximation r^k for $k > 0$ is continuous around $r = 0$ and equals 0 for $r = 0$. However, for $k < 0$, r^k is not continuous in the neighborhood of $r = 0$ because $r^k \rightarrow \infty$ as $r \downarrow 0$.

Smoothness requirements for $\partial_\varphi^2 v_x$ can be obtained with the following lemma to ensure that $\int_0^R \frac{1}{r} \partial_\varphi^2 v_x dr$ is bounded.

Lemma 2.1. For $f : [0, R] \rightarrow \mathbb{R}$ bounded, $f = 0$ for $r = 0$, and f is Lipschitz continuous in a neighborhood around $r = 0$, there exist an $M > 0$ and $k > 0$ such that $|f|$ is bounded by Mr^k .

Proof This proof is trivial for $f \equiv 0$. Let f be a bounded function (with $\sup |f| > 0$), $f = 0$ for $r = 0$, and f is Lipschitz continuous in a neighborhood around $r = 0$. Choose $\delta \in (0, \min\{1, R\})$ such that f is Lipschitz continuous on $[0, \delta]$ with a Lipschitz constant $L > 0$. Let $M_1 = L$ and $k_1 = 1$. For $0 \leq r \leq \delta$ we have

$$|f(r) - f(0)| \leq L|r - 0| \implies |f(r)| \leq Lr = M_1 r^{k_1}.$$

Let $M_2 = \sup |f| + 1$ and $k_2 = \frac{1}{\ln \delta} \ln \left(\frac{\sup |f|}{\sup |f| + 1} \right)$. We have for $r \in [\delta, R]$

$$\begin{aligned} M_2 r^{k_2} &\geq M_2 \delta^{k_2} \\ &= (\sup |f| + 1) \delta^{k_2} \\ &= (\sup |f| + 1) \exp(k_2 \ln \delta) \\ &= (\sup |f| + 1) \exp \left(\frac{1}{\ln \delta} \ln \left(\frac{\sup |f|}{\sup |f| + 1} \right) \ln \delta \right) \\ &= (\sup |f| + 1) \left(\frac{\sup |f|}{\sup |f| + 1} \right) \\ &= \sup |f|. \end{aligned}$$

Hence, $|f|$ is bounded by Mr^k by taking $M = \max\{M_1, M_2\}$ and $k = \min\{k_1, k_2\}$.

Lipchitz continuity ensures that f does not have a jump discontinuity at $r = 0$. Given that $\partial_\varphi^2 v_x$ is continuous on the closure of Ω^{3D} , to ensure boundedness, $\partial_\varphi^2 v_x$ is differentiable w.r.t r , to ensure Lipschitz continuous in the neighborhood around $r = 0$, and by incorporating the boundary condition $\partial_\varphi^2 v_x|_{r=0} = 0$, Lemma 2.1 can be used to ensure that $\int_0^R \frac{1}{r} \partial_\varphi^2 v_x dr$ is bounded.

By integrating the boundary condition $\partial_\varphi^2 v_x|_{r=0} = 0$ twice with respect to φ , the boundary condition is equal to

$$v_x(t, x, \varphi, 0) = v_0(t, x) + \varphi v_1(t, x).$$

where $v_1(t, x) = 0$ due to periodic boundary condition [$v_x(t, x, \varphi, r) = v_x(t, x, \varphi + 2\pi, r)$]. Thus, axial velocity within the artery's origin is independent of φ , or rather, the continuity condition (2.2.4) should be satisfied.

The dimension corresponding to r will be removed in the 2D ROM. The requirement that $\partial_\varphi^2 v_x$ has no jump-discontinuity at $r = 0$ will be satisfied by incorporating the reduced axial velocity (2.2.2). By incorporating the reduced axial velocity, the continuity condition $\partial_\varphi^2 v_x|_{r=0} = 0$ becomes a partial differential equation that needs to be satisfied for all $t \geq 0$. If the continuity condition is not satisfied, $\partial_\varphi^2 v_x|_{r=0} = 0$ no longer holds and $\int_0^R \frac{1}{r} \partial_\varphi^2 v_x dr$ becomes unbounded. The mathematical expression for the continuity condition for the 2D ROM depends on which velocity profiles are allowed in the 2D ROM.

The following subsections show that $\int_0^R \frac{1}{r} \partial_\varphi^2 v_x dr$ is bounded by incorporating the reduced axial velocity (2.2.2) in conjunction with the continuity condition ($\partial_\varphi v_x|_{r=0} = 0$) (and sufficient smoothness requirements).

2.2.2. Axisymmetric flow model

By incorporating all assumptions denoted in Section 2.2.1, blood flow in two dimensions will be obtained in this section. The continuity condition (2.2.4) from Assumption 5 states that the axial velocity in the origin $v_x(t, x, \varphi, 0)$ is independent of φ . Due to the simplicity of velocity profile, $s(0)$ is independent of φ and $s'(0) = 0$. Applying the continuity condition shows that $\partial_\varphi u(t, x, \varphi) = 0$, meaning that $u(t, x, \varphi)$ is independent of φ . This is why this model is called the *axisymmetrical flow model*. The temporal and spatial coordinates of $R(t, x, \varphi)$, $v_x(t, x, \varphi, r)$, $u(t, x, \varphi)$ and $s(y)$ (or $s(r/R(t, x, \varphi))$) will sometimes be omitted in this section.

Compute problematic integral

Before obtaining the axisymmetric flow model, we will verify that the integral $\int_0^R \frac{1}{r} \partial_\varphi^2 v_x dr$ is bounded given that $\partial_\varphi u = 0$. Applying equation (2.2.2), the substitution $r = yR$, $\partial_\varphi u = 0$, and u is independent of y yields

$$\int_0^R \frac{1}{r} \partial_\varphi^2 v_x dr = \int_0^R \frac{1}{r} \partial_\varphi^2 \left(us \left(\frac{r}{R} \right) \right) dr = \int_0^1 \frac{1}{y} \partial_\varphi^2 (us(y)) dy = \int_0^1 \frac{1}{y} u \partial_\varphi^2 (s(y)) dy = u \int_0^1 \frac{1}{y} \partial_\varphi^2 (s(y)) dy. \quad (2.2.6)$$

From the rescale $r = yR$, we obtain $y(t, x, \varphi) = r/R(t, x, \varphi)$, so y depends on φ through R . With the chain rule, we obtain the first-order derivative

$$\partial_\varphi s(y) = \frac{\partial s}{\partial y} \frac{\partial y}{\partial \varphi}.$$

With the chain rule and product rule, we obtain the second-order derivative

$$\partial_\varphi^2 s(y) = \frac{\partial^2 s}{\partial^2 y} \left(\frac{\partial y}{\partial \varphi} \right)^2 + \frac{\partial s}{\partial y} \frac{\partial^2 y}{\partial \varphi^2} \quad (2.2.7)$$

With the chain rule and product rule, we obtain the derivatives of y

$$\frac{\partial y}{\partial \varphi} = -\frac{r \partial_\varphi R}{R^2} = -\frac{y \partial_\varphi R}{R}, \quad (2.2.8)$$

$$\frac{\partial^2 y}{\partial \varphi^2} = r \frac{2(\partial_\varphi R)^2 - R \partial_\varphi^2 R}{R^3} = y \frac{2(\partial_\varphi R)^2 - R \partial_\varphi^2 R}{R^2}. \quad (2.2.9)$$

Substituting equation (2.2.7), and equations (2.2.8) and (2.2.9) into equation (2.2.6) yields

$$\begin{aligned} \int_0^R \frac{1}{r} \partial_\varphi^2 v_x dr &= u \int_0^1 \frac{1}{y} \frac{\partial^2 s}{\partial^2 y} \left(\frac{\partial y}{\partial \varphi} \right)^2 + \frac{1}{y} \frac{\partial s}{\partial y} \frac{\partial^2 y}{\partial \varphi^2} dy \\ &= u \int_0^1 y s'' \frac{(\partial_\varphi R)^2}{R^2} + s' \frac{2(\partial_\varphi R)^2 - R \partial_\varphi^2 R}{R^2} dy \\ &= u \frac{(\partial_\varphi R)^2}{R^2} \int_0^1 y s'' dy + u \frac{2(\partial_\varphi R)^2 - R \partial_\varphi^2 R}{R^2} \int_0^1 s' dy. \end{aligned} \quad (2.2.10)$$

By applying integration by parts and equation (1.3.5) we have

$$\int_0^1 y s''(y) dy = s'(1) - \int_0^1 s'(y) dy = s'(1) - s(0) \quad (2.2.11)$$

Substituting equation (2.2.11) into (2.2.10) yields

$$\begin{aligned}
\int_0^R \frac{1}{r} \partial_\varphi^2 v_x dr &= us'(1) \frac{(\partial_\varphi R)^2}{R^2} - us(0) \frac{(\partial_\varphi R)^2 - R \partial_\varphi^2 R}{R^2} \\
&= u \left(s'(1) \frac{[(\partial_\varphi R)^2 + R \partial_\varphi^2 R] - R \partial_\varphi^2 R}{R^2} - s(0) \frac{[(\partial_\varphi R)^2 + R \partial_\varphi^2 R] - 2R \partial_\varphi^2 R}{R^2} \right) \\
&= u \left(\frac{s'(1)}{2} \frac{(\partial_\varphi^2(R^2))}{R^2} - s'(1) \frac{\partial_\varphi^2 R}{R} - \frac{s(0)}{2} \frac{\partial_\varphi^2(R^2)}{R^2} + 2s(0) \frac{\partial_\varphi^2 R}{R} \right) \\
&= u(2s(0) - s'(1)) \frac{\partial_\varphi^2 R}{R} - u \frac{s(0) - s'(1)}{2} \frac{\partial_\varphi^2(R^2)}{R^2}.
\end{aligned} \tag{2.2.12}$$

Applying the velocity profile $s(y) = \frac{\gamma+2}{\gamma}(1-y^\gamma)$ yields

$$\int_0^R \frac{1}{r} \partial_\varphi^2 v_x dr = u \frac{(\gamma+2)^2}{\gamma} \frac{\partial_\varphi^2 R}{R} - u \frac{(\gamma+1)(\gamma+2)}{2\gamma} \frac{\partial_\varphi^2(R^2)}{R^2}. \tag{2.2.13}$$

The integral is bounded if $\partial_\varphi^2 R$ is bounded.

Final model

The axisymmetric flow model is obtained with 3 steps. Control volumes are defined in the first step as

$$V_{x_1, x_2, \varphi_1, \varphi_2} = \{(x, \varphi, r) : x \in (x_1, x_2), \varphi \in (\varphi_1, \varphi_2), r \in [0, R(t, x, \varphi)]\}, \tag{2.2.14}$$

where $x_{in} < x_1 < x_2 < x_{out}$ and $0 < \varphi_1 < \varphi_2 < 2\pi$. The shape of each control volume depends on x_1 , x_2 , φ_1 , and φ_2 , as we only want to include the axial and azimuthal dimensions in the 2D ROM. The union of all possible control volumes covers the three-dimensional domain Ω^{3D} . The conservation of mass equation (1.2.5) and the balance of momentum equation (1.2.8) are satisfied for all control volumes in the second step. The third step involves obtaining the differential form by applying lemma Lagrange (2D). The second and third steps are done in Appendix A. The following equations govern the axisymmetric flow model:

$$\partial_t(R^2) + \partial_x(uR^2) = 0 \quad \text{for } (t, x, \varphi) \in (0, T) \times \Omega, \tag{2.2.15}$$

$$\begin{aligned}
\rho \partial_t(uR^2) + \rho \frac{\gamma+2}{\gamma+1} \partial_x(u^2 R^2) &= \mu \frac{\gamma+2}{\gamma} u \left(-2\gamma + 2(\gamma+2) \frac{\partial_\varphi^2 R}{R} \right. \\
&\left. - (\gamma+1) \frac{\partial_\varphi^2(R^2)}{R^2} \right) - \frac{R^2 \partial_x R}{R_0^2} \beta - R^2 \frac{R-R_0}{R_0^2} \partial_x \beta \quad \text{for } (t, x, \varphi) \in (0, T) \times \Omega,
\end{aligned} \tag{2.2.16}$$

$$\partial_\varphi u = 0. \quad \text{for } (t, x, \varphi) \in (0, T) \times \Omega \tag{2.2.17}$$

Equation (2.2.15) conserves mass within the artery, equation (2.2.16) balances momentum within the artery, and (2.2.17) satisfies the continuity condition (2.2.4). These three equations only have two unknown functions $u \in C^1(0, T) \times C^2(\Omega)$ and $R \in C^1(0, T) \times C^2(\Omega)$.

To determine if the axisymmetric flow model is well-posed, we will determine if the continuity condition (2.2.17) is superfluous given that the conservation of mass equation (2.2.15) and the balance of momentum equation (2.2.16) holds. Applying $\partial_t(R^2) = -\partial_x(uR^2)$ (from (2.2.15)) into the balance of momentum equation yields

$$\begin{aligned}
\partial_t u &= - \left(\alpha - \frac{1}{2} \right) \partial_x(u^2) - (\alpha-1) u^2 \frac{\partial_x(R^2)}{R^2} - \frac{\partial_x R}{\rho R_0^2} \beta - \frac{R-R_0}{\rho R_0^2} \partial_x \beta \\
&+ \frac{\mu}{\rho} \frac{\gamma+2}{\gamma} \frac{u}{R^2} \left(-2\gamma - 2\gamma(\partial_x R)^2 + 2(\gamma+2) \frac{\partial_\varphi(R^2)}{R^2} - (\gamma+1) \frac{\partial_\varphi^2(R^2)}{R^2} \right),
\end{aligned} \tag{2.2.18}$$

where $\alpha = \frac{\gamma+2}{\gamma+1}$. In the axisymmetric flow model, u is independent of φ . Thus, $\partial_t u$ should also be independent of φ . However, (2.2.18) clearly shows that $\partial_t u$ depends on φ since R depends on φ . The axisymmetric flow model turns into the 1D ROM once R and u are independent of φ . The continuity condition (2.2.17) is not

superfluous if R still depends on φ . For example, applying the initial conditions $u(0, x) = 0$, $R(0, x, \varphi) = 2 + \sin(x + \varphi)$ and $\beta(x, \varphi) = \beta_0 > 0$ shows that

$$\partial_t u = -\frac{\cos(x + \varphi)}{\rho R_0^2} \beta_0$$

is dependent on φ . This model should be avoided because the number of equations exceeds the number of unknown independent functions.

2.2.3. Asymmetric flow model

The axisymmetric flow model becomes either axisymmetric since the velocity profile does not depend on φ in the artery's origin or ill-posed since the two unknown functions u and R cannot always satisfy three equations. To resolve both issues, we propose to extend the velocity profile by letting $\gamma(t, x, \varphi) : [0, T] \times \Omega \rightarrow (0, \infty)$ also depends on t , x and φ , and by extending the velocity profile

$$s(y, \gamma) = \frac{\gamma + 2}{\gamma} (1 - y^\gamma) \quad (2.2.19)$$

to allow a family of velocity profiles into the 2D ROM. This proposal equalizes the number of equations with the number of unknown functions while extending the velocity profile to enable asymmetric mean velocities (see Figure 2.5). The model obtained by including this proposal is called the *asymmetric flow model*. With

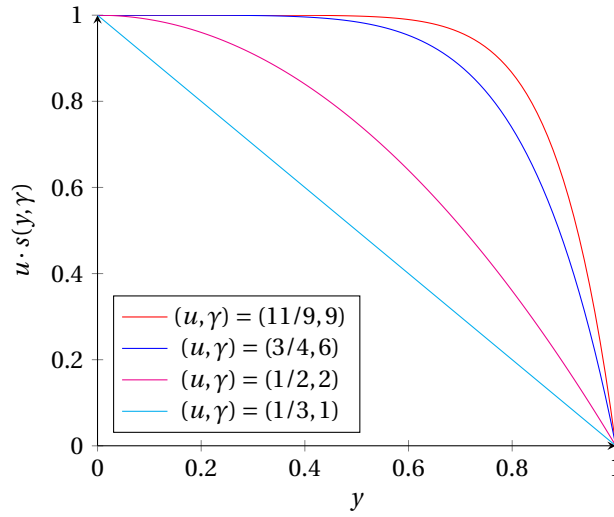


Figure 2.5: Different velocity profiles that satisfy $\partial_\varphi v_x|_{r=0} = 0$

this proposal, the continuity condition (2.2.4) becomes by substituting

$$\partial_\varphi (v_x(t, x, \varphi, 0)) = \partial_\varphi (u(t, x, \varphi) s(0, \gamma(t, x, \varphi))) = \partial_\varphi \left(u(t, x, \varphi) \frac{\gamma(t, x, \varphi) + 2}{\gamma(t, x, \varphi)} \right) = 0. \quad (2.2.20)$$

The temporal and spatial coordinates of $R(t, x, \varphi)$, $v_x(t, x, \varphi, r)$, $u(t, x, \varphi)$ and $\gamma(t, x, \varphi)$ will sometimes be omitted in this section.

Compute problematic integral

Before obtaining the asymmetric flow model, we will first verify if the integral $\int_0^R \frac{1}{r} \partial_\varphi^2 v_x dr$ is bounded given that equation (2.2.20) holds. Applying equation (2.2.3), the rescale $r = Ry$, and applying the extended velocity profile (2.2.19) yields

$$\int_0^R \frac{1}{r} \partial_\varphi^2 v_x dr = \int_0^1 \frac{1}{Ry} \partial_\varphi^2 (us(\frac{r}{R}, \gamma)) dr = \int_0^1 \frac{1}{y} \partial_\varphi^2 (us(y, \gamma)) dy = \int_0^1 \frac{1}{y} \partial_\varphi^2 \left(u \frac{\gamma + 2}{\gamma} (1 - y^\gamma) \right) dy \quad (2.2.21)$$

The continuity condition (2.2.20) indicates that $u \frac{\gamma + 2}{\gamma}$ should be independent of φ . As a consequence, we obtain

$$\partial_\varphi^2 \left(u \frac{\gamma + 2}{\gamma} (1 - y^\gamma) \right) = u \frac{\gamma + 2}{\gamma} \partial_\varphi^2 (1 - y^\gamma). \quad (2.2.22)$$

Substituting (2.2.22) into (2.2.21) yields

$$\int_0^R \frac{1}{r} \partial_\varphi^2 v_x dr = \int_0^1 \frac{1}{y} u \frac{\gamma+2}{\gamma} \partial_\varphi^2 (1-y^\gamma) dy = u \frac{\gamma+2}{\gamma} \int_0^1 \frac{1}{y} \partial_\varphi^2 (1-y^\gamma) dy \quad (2.2.23)$$

since u and γ are independent of y . The derivative $\partial_\varphi^2(1-y^\gamma)$ needs to be computed. From the rescale $r = yR$, we obtain $y(t, x, \varphi) = r/R(t, x, \varphi)$, so y depends on φ through R . From the chain rule and product rule, we obtain the first-order derivative

$$\partial_\varphi (1-y^\gamma) = \frac{\partial y}{\partial R} \frac{\partial R}{\partial \varphi} \frac{\partial}{\partial y} (1-y^\gamma) + \frac{\partial \gamma}{\partial \varphi} \frac{\partial}{\partial \gamma} (1-y^\gamma),$$

and the second-order derivative

$$\begin{aligned} \partial_\varphi^2 (1-y^\gamma) &= \left(\frac{\partial y}{\partial R} \frac{\partial R}{\partial \varphi} \right)^2 \frac{\partial^2}{\partial y^2} (1-y^\gamma) + \frac{\partial^2 y}{\partial R^2} \left(\frac{\partial R}{\partial \varphi} \right)^2 \frac{\partial}{\partial y} (1-y^\gamma) + \frac{\partial y}{\partial R} \frac{\partial^2 R}{\partial \varphi^2} \frac{\partial}{\partial y} (1-y^\gamma) \\ &+ 2 \frac{\partial y}{\partial R} \frac{\partial R}{\partial \varphi} \frac{\partial \gamma}{\partial \varphi} \frac{\partial^2}{\partial y \partial \gamma} (1-y^\gamma) + \left(\frac{\partial \gamma}{\partial \varphi} \right)^2 \frac{\partial^2}{\partial \gamma^2} (1-y^\gamma) + \frac{\partial^2 \gamma}{\partial \varphi^2} \frac{\partial}{\partial \gamma} (1-y^\gamma). \end{aligned} \quad (2.2.24)$$

Substituting (2.2.24) into (2.2.23) yields

$$\begin{aligned} \int_0^R \frac{1}{r} \partial_\varphi^2 v_x dr &= u \frac{\gamma+2}{\gamma} \int_0^1 \frac{1}{y} \left(\overbrace{\left(\frac{\partial y}{\partial R} \frac{\partial R}{\partial \varphi} \right)^2 \frac{\partial^2}{\partial y^2} (1-y^\gamma)}^i + \overbrace{\frac{\partial^2 y}{\partial R^2} \left(\frac{\partial R}{\partial \varphi} \right)^2 \frac{\partial}{\partial y} (1-y^\gamma)}^{ii} + \overbrace{\frac{\partial y}{\partial R} \frac{\partial^2 R}{\partial \varphi^2} \frac{\partial}{\partial y} (1-y^\gamma)}^{iii} \right. \\ &\left. + 2 \underbrace{\frac{\partial y}{\partial R} \frac{\partial R}{\partial \varphi} \frac{\partial \gamma}{\partial \varphi} \frac{\partial^2}{\partial y \partial \gamma} (1-y^\gamma)}_{iv} + \underbrace{\left(\frac{\partial \gamma}{\partial \varphi} \right)^2 \frac{\partial^2}{\partial \gamma^2} (1-y^\gamma)}_v + \underbrace{\frac{\partial^2 \gamma}{\partial \varphi^2} \frac{\partial}{\partial \gamma} (1-y^\gamma)}_{vi} \right) dy. \end{aligned} \quad (2.2.25)$$

A couple of intermediate results will be computed to evaluate $\int_0^R \frac{1}{r} \partial_\varphi^2 v_x dr$. y has the first- and second-order partial derivatives

$$\frac{\partial y}{\partial R} = -\frac{r}{R^2} = -\frac{y}{R}, \quad (2.2.26)$$

$$\frac{\partial^2 y}{\partial R^2} = \frac{2r}{R^3} = \frac{2y}{R^2}, \quad (2.2.27)$$

$(1-y^\gamma)$ has the first- and second-order partial derivatives

$$\begin{cases} \frac{\partial}{\partial y} (1-y^\gamma) = -\gamma y^{\gamma-1}, \\ \frac{\partial^2}{\partial y^2} (1-y^\gamma) = -\gamma(\gamma-1)y^{\gamma-2}, \\ \frac{\partial}{\partial \gamma} (1-y^\gamma) = -y^\gamma \ln y, \\ \frac{\partial^2}{\partial \gamma^2} (1-y^\gamma) = -y^\gamma (\ln y)^2, \\ \frac{\partial^2}{\partial y \partial \gamma} (1-y^\gamma) = -y^{\gamma-1} - \gamma y^{\gamma-1} \ln y. \end{cases}$$

By applying L'Hôpital's rule, we can show that for $\gamma > 0$ that

$$\lim_{y \downarrow 0} y^\gamma \ln y = \lim_{y \downarrow 0} \frac{\ln y}{y^{-\gamma}} = \lim_{y \downarrow 0} -\frac{1}{\gamma} y^\gamma = 0, \quad (2.2.28)$$

and that

$$\lim_{y \downarrow 0} y^\gamma (\ln y)^2 = \lim_{y \downarrow 0} \frac{(\ln y)^2}{y^{-\gamma}} = -\frac{2}{\gamma} \lim_{y \downarrow 0} \frac{\ln y}{y^{-\gamma}} = 0. \quad (2.2.29)$$

With (2.2.28) and integration by parts, the integral $\int_0^1 y^\gamma \ln y dy$ is for $\gamma > -1$ is equal to

$$\int_0^1 y^\gamma \ln y dy = \frac{\ln 1}{\gamma+1} - \frac{1}{\gamma+1} \int_0^1 y^\gamma dy = -\frac{1}{(\gamma+1)^2}. \quad (2.2.30)$$

With integration by parts and the previous two equations, the integral $\int_0^1 y^\gamma (\ln y)^2 dy$ is for $\gamma > -1$ is equal to

$$\int_0^1 y^\gamma (\ln y)^2 dy = \frac{(\ln 1)^2}{\gamma+1} - \frac{2}{\gamma+1} \int_0^1 y^\gamma \ln y dy = \frac{2}{(\gamma+1)^3}. \quad (2.2.31)$$

By incorporating (2.2.26), (2.2.27), (2.2.30), and (2.2.31), the integrals $i-vi$ within equation (2.2.25) are computed as

$$\begin{cases} i = -\gamma(\gamma-1) \frac{(\partial_\varphi R)^2}{R^2} \int_0^1 y^{\gamma-1} dy & = -(\gamma-1) \frac{(\partial_\varphi R)^2}{R^2}, \\ ii = -2\gamma \frac{(\partial_\varphi R)^2}{R^2} \int_0^1 y^{\gamma-1} dy & = -2 \frac{(\partial_\varphi R)^2}{R^2}, \\ iii = \gamma \frac{\partial_\varphi^2 R}{R} \int_0^1 y^{\gamma-1} dy & = \frac{\partial_\varphi^2 R}{R}, \\ iv = 2 \frac{\partial_\varphi R}{R} \partial_\varphi \gamma \int_0^1 (y^{\gamma-1} + y^{\gamma-1} \gamma \ln y) dy & = 2 \frac{\partial_\varphi R}{R} \frac{\gamma-1}{\gamma^2} \partial_\varphi \gamma, \\ v = -(\partial_\varphi \gamma)^2 \int_0^1 y^{\gamma-1} (\ln y)^2 dy & = -2 \frac{1}{\gamma^3} (\partial_\varphi \gamma)^2, \\ vi = -\partial_\varphi^2 \gamma \int_0^1 y^{\gamma-1} \ln y dy & = \frac{1}{\gamma^2} \partial_\varphi^2 \gamma. \end{cases}$$

With these results, we obtain

$$\begin{aligned} \int_0^R \frac{1}{r} \partial_\varphi^2 v_x dr &= u \frac{\gamma+2}{\gamma} \left(-\gamma \frac{(\partial_\varphi R)^2}{R^2} + \frac{R \partial_\varphi^2 R - (\partial_\varphi R)^2}{R^2} + 2 \frac{\gamma-1}{\gamma^2} \partial_\varphi \gamma \frac{\partial_\varphi R}{R} - \frac{2}{\gamma^3} (\partial_\varphi \gamma)^2 + \frac{1}{\gamma^2} \partial_\varphi^2 \gamma \right) \\ &= u \frac{\gamma+2}{\gamma} \left((\gamma+2) \frac{\partial_\varphi^2 R}{R} - \frac{\gamma+1}{2} \frac{\partial_\varphi^2 (R^2)}{R^2} + 2 \frac{\gamma-1}{\gamma^2} \partial_\varphi \gamma \frac{\partial_\varphi R}{R} - \frac{2}{\gamma^3} (\partial_\varphi \gamma)^2 + \frac{1}{\gamma^2} \partial_\varphi^2 \gamma \right), \end{aligned} \quad (2.2.32)$$

See (2.2.12) for the intermediate computations. The integral is bounded if the partial derivatives $\partial_\varphi R$, $\partial_\varphi^2 R$, $\partial_\varphi \gamma$ and $\partial_\varphi^2 \gamma$ are bounded.

Final model

The asymmetric flow model is obtained by first satisfying the conservation of mass (1.2.5) and balance of momentum (1.2.8) equations for the control volumes depicted in (2.2.14), and then by applying lemma Lagrange (2D) (see Appendix B for the entire computation). The following equations govern the asymmetric flow model:

$$\partial_t (R^2) + \partial_x (uR^2) = 0, \quad (2.2.33)$$

$$\begin{aligned} \rho \partial_t (uR^2) + \rho \frac{\gamma+2}{\gamma+1} \partial_x (u^2 R^2) &= u^2 R^2 \frac{5\gamma+4}{2\gamma(\gamma+1)^2} \partial_x \gamma + 2\mu u \frac{\gamma+2}{\gamma} \left(-\gamma + (\gamma+2) \frac{\partial_\varphi^2 R}{R} \right. \\ &\quad \left. - \frac{\gamma+1}{2} \frac{\partial_\varphi^2 (R^2)}{R^2} + 2 \frac{\gamma-1}{\gamma^2} \partial_\varphi \gamma \frac{\partial_\varphi R}{R} - \frac{2}{\gamma^3} (\partial_\varphi \gamma)^2 + \frac{1}{\gamma^2} \partial_\varphi^2 \gamma \right) - \frac{R^2 \partial_x R}{R_0^2} \beta - R^2 \frac{R-R_0}{R_0^2} \partial_x \beta, \end{aligned} \quad (2.2.34)$$

$$\partial_\varphi \left(\frac{\gamma+2}{\gamma} u \right) = 0, \quad (2.2.35)$$

where u , R , and γ are once differentiable with respect to time and twice with respect to space. Equation (2.2.33) is the continuity equation, which preserves mass in the artery, equation (2.2.34) balances momentum within the artery and equation (2.2.35) ensures that axial velocity within the artery's origin is axisymmetric.

The asymmetric flow model (which will be referred to as the 2D ROM) is quite similar to the 1D ROM. Both the 1D ROM and the 2D ROM have the continuity equation. By removing every blue-colored term from the 2D balance of momentum equation (2.2.34), i.e., all terms that have a derivative of γ and every term with a derivative w.r.t. φ , the 1D balance of momentum equation is obtained. All these terms vanish if γ is a constant within an axisymmetric setting ($\partial_\varphi u = 0$ and $\partial_\varphi R$). The continuity condition (2.2.35) is also satisfied under these conditions. Some 1D ROM also imposes viscous axisymmetric flow ($\partial_r v_x|_{r=0} = 0$). Smoothness conditions of axial velocity in a neighborhood near the artery's origin must be added to the 2D ROM to obtain a condition similar to the viscous axisymmetric flow 1.3.7. Continuity of axial velocity is satisfied in the 2D ROM, but axial velocity in the neighborhood of the artery's origin does not need to be smooth.

The asymmetric flow model can be written into the quasi-linear form

$$\partial_t \mathbf{q} + H(\mathbf{q}, \gamma; \beta) \partial_x \mathbf{q} = \mathbf{s}(\mathbf{q}, \gamma), \quad (2.2.36)$$

$$\partial_\varphi (g(\mathbf{q}, \gamma)) = 0, \quad (2.2.37)$$

where

$$\mathbf{q} = \begin{bmatrix} R^2 \\ uR^2 \end{bmatrix} = \begin{bmatrix} A \\ Q \end{bmatrix},$$

$$H = \begin{bmatrix} 0 & 1 \\ \frac{\sqrt{A}\beta}{2\rho A_0} - \frac{Q^2}{A^2} \frac{\gamma+2}{\gamma+1} & 2\frac{Q}{A} \frac{\gamma+2}{\gamma+1} \end{bmatrix},$$

$$\mathbf{s}(\mathbf{q}, \gamma) = \begin{bmatrix} 0 \\ s^x + s^\varphi \end{bmatrix},$$

$$s^x = -2(\gamma+2) \frac{\mu}{\rho} \frac{Q}{A} + \frac{Q^2}{A} \frac{5\gamma+4}{2\gamma(\gamma+1)^2} \partial_x \gamma - A \frac{\sqrt{A} - \sqrt{A_0}}{\rho A_0} \partial_x \beta,$$

$$s^\varphi = 2 \frac{\mu}{\rho} \frac{\gamma+2}{\gamma} \frac{Q}{A} \left(-\frac{\gamma+2}{4} \frac{(\partial_\varphi A)^2}{A^2} + \frac{1}{2} \frac{\partial_\varphi^2 A}{A} \right. \\ \left. + \frac{(\gamma-1)\partial_\varphi \gamma}{\gamma^2} \frac{\partial_\varphi A}{A} - \frac{2}{\gamma^3} (\partial_\varphi \gamma)^2 + \frac{1}{\gamma^2} \partial_\varphi^2 \gamma \right) \text{ and}$$

$$\mathbf{g} = \frac{\gamma+2}{\gamma} \frac{Q}{A}.$$

Equation (2.2.36) represents the 2D Navier-Stokes equation, and equation (2.2.37) represents the continuity condition. A is referred to as area since it has a dimension of cm^2 , but within the context of the 2D ROM A is a substitution for R^2 . The area of a cross section, computed as

$$\int_0^{2\pi} \int_0^R r \, dr \, d\varphi = \int_0^{2\pi} \frac{1}{2} R^2 \, d\varphi = \frac{1}{2} \int_0^{2\pi} A \, d\varphi,$$

shows that A should have been substituted with $\frac{1}{2}R^2$, not R^2 . Hence, the actual flow rate within a cross section is computed as $\frac{1}{2} \int_0^{2\pi} Q \, d\varphi$.

H can be diagonalized by $LHR = \Lambda$, where

$$R = \begin{bmatrix} 1 & 1 \\ \lambda_1 & \lambda_2 \end{bmatrix}, \quad \Lambda = \begin{bmatrix} \lambda_1 & 0 \\ 0 & \lambda_2 \end{bmatrix} \text{ and } L = R^{-1} = \frac{1}{\lambda_2 - \lambda_1} \begin{bmatrix} \lambda_2 & -1 \\ -\lambda_1 & 1 \end{bmatrix}.$$

The asymmetric flow model will be applied with periodic boundary conditions

$$\begin{cases} \mathbf{q}(t, x, 0) = \mathbf{q}(t, x, 2\pi), \\ \gamma(t, x, 0) = \gamma(t, x, 2\pi), \end{cases}$$

an axisymmetric velocity at the inlet

$$Q(t, x_{in}, \varphi) = v_{in}(t) A(t, x_{in}, \varphi) \quad (2.2.38)$$

and the fluid resistance boundary condition at the outlet

$$P(t, x_{out}, \varphi) = P_{res} + Q(t, x_{in}, \varphi) R_{res}. \quad (2.2.39)$$

For testing the numerical accuracy of the model, we will also apply an axisymmetric pressure at the inlet

$$P(t, 0, \varphi) = P_{in}(t), \quad (2.2.40)$$

and a non-reflective boundary condition at the outlet [18]

$$\mathbf{I}_1(\mathbf{q}) \left(\partial_t \mathbf{q} - \begin{bmatrix} 0 \\ s^x + s^\varphi \end{bmatrix} \right) = 0 \quad \text{for } x = x_{out} \quad (2.2.41)$$

where \mathbf{I}_1 is the left eigenvalue of H corresponding to $\lambda_1 < 0$.

2.2.4. Numerical methods

Finite volume methods will be applied to develop numerical methods for the 2D ROM the asymmetric flow model. Finite volume methods are based on Leveque's book [12]. The two-dimensional domain (Figure 2.3) is discretized in a structured mesh with n_x number of columns (or discretized cross-sections) and n_φ number of rows (or cells within a cross-section). Each cell has a width of $\Delta x = 1.5/n_x$ cm and a height of $\Delta\varphi = 2\pi/n_\varphi$. Cell $C_{i,j}$ refers to the i -th row and j -th column (see Figure 2.6). $A_{i,j}^n$ refers to the average area across cell $C_{i,j}$ at time $t = n\Delta t$, where Δt is the time step size.

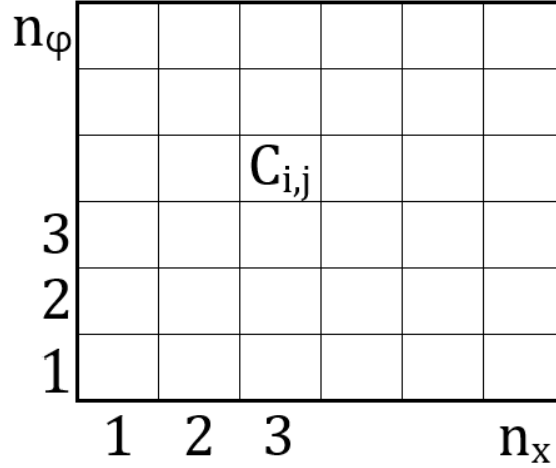


Figure 2.6: Two-dimensional structured mesh. n_x refers to the number of discretized cross-sections (or columns), and n_φ refers to the number of cells within a cross-section (or rows).

To develop a numerical method for the asymmetric flow model, equations (2.2.36) and (2.2.37) will be solved separately. Separating these equations leads to a splitting error. Dimensional splitting will be applied to develop numerical methods for equation (2.2.36) since the numerical method already has a splitting error. By applying Godunov splitting, the full problem is split into the sub-problems

$$\begin{aligned} \text{Problem A: } & \begin{cases} \partial_t \mathbf{q} = \begin{bmatrix} 0 & s^\varphi \end{bmatrix}^T, \\ \partial_t \gamma = 0, \end{cases} \\ \text{Problem B: } & \begin{cases} \partial_t \mathbf{q} + H(\mathbf{q}; \gamma, \beta) \partial_x \mathbf{q} = \begin{bmatrix} 0 & s^x \end{bmatrix}^T, \\ \partial_t \gamma = 0, \end{cases} \\ \text{Problem C: } & \partial_\varphi g(\mathbf{q}) = 0. \end{aligned}$$

Each problem will be solved within one iteration. An iteration starts by simulating Problem A, proceeds by solving Problem B analytically, and ends by changing γ to satisfy Problem C. Problem A uses the values of \mathbf{q} and γ at the beginning of the time step, Problem B uses the value of \mathbf{q} and γ after simulating problem A, and Problem C uses the value of \mathbf{q} and γ after solving Problem B. Each of these problems will be discussed separately.

Problem A

In this problem, flow rate for the first intermediate state ($Q_{i,j}^{n+1/3}$) will be obtained by performing a φ -sweep. Problem A is identical to

$$\begin{cases} \partial_t A = 0, \\ \partial_t Q = s^\varphi = h(A, \gamma)Q, \\ \partial_t \gamma = 0, \end{cases} \quad (2.2.42)$$

where

$$h = 2 \frac{\mu}{\rho} \frac{\gamma + 2}{\gamma A} \left(-\frac{\gamma + 2}{4} \frac{(\partial_\varphi A)^2}{A^2} + \frac{1}{2} \frac{\partial_\varphi^2 A}{A} + \frac{(\gamma - 1) \partial_\varphi \gamma}{\gamma^2} \frac{\partial_\varphi A}{A} - \frac{2}{\gamma^3} (\partial_\varphi \gamma)^2 + \frac{1}{\gamma^2} \partial_\varphi^2 \gamma \right).$$

Since A and γ do not change in time within this problem, h can be considered a constant, and this problem has the analytical solution

$$Q_{i,j}^{n+1/3} = Q_{i,j}^n e^{h\Delta t}. \quad (2.2.43)$$

The solution of this problem depends on the discretization of $\partial_\varphi A$, $\partial_\varphi^2 A$, $\partial_\varphi \gamma$ and $\partial_\varphi^2 \gamma$. Central difference approximations are applied, which yields

$$\partial_\varphi f_{i,j} = \frac{-f_{i,j-1} + f_{i,j+1}}{2\Delta\varphi}, \quad (2.2.44)$$

$$\partial_\varphi^2 f_{i,j} = \frac{f_{i,j-1} - 2f_{i,j} + f_{i,j+1}}{\Delta\varphi^2}, \quad (2.2.45)$$

where f can be substituted with either A or γ .

Problem B

In this problem, area and flow rate for the second intermediate state $\mathbf{q}_{i,j}^{n+2/3}$ will be obtained by performing an x -sweep. Problem B is identical to

$$\partial_t \mathbf{q} + H(\mathbf{q}; \gamma, \beta) \partial_x \mathbf{q} = [0 \quad s^x]^T, \quad (2.2.46)$$

where both γ and β are independent of t . A high-resolution method will be applied. Cell averages for the next intermediate step are computed as

$$\mathbf{q}_{i,j}^{n+1} = \mathbf{q}_{i,j}^n - \frac{\Delta t}{\Delta x} \left(\mathcal{A}_{i-\frac{1}{2},j}^+ + \mathcal{A}_{i+\frac{1}{2},j}^- \right) - \frac{\Delta t}{\Delta x} \left(\tilde{F}_{i+\frac{1}{2},j} - \tilde{F}_{i-\frac{1}{2},j} \right) + \Delta t s_{i,j}^x$$

where $\mathcal{A}_{i+\frac{1}{2},j}^+$ and $\mathcal{A}_{i+\frac{1}{2},j}^-$ are fluctuations, $\tilde{F}_{i+\frac{1}{2},j}$ limited second-order correction terms, and

$$s_{i,j}^x = s^x(A_{i,j}^n, Q_{i,j}^n, \gamma_{i,j}^n)$$

is the discretized source term. Both fluctuations and second-order correction terms are obtained by linearizing the matrix H at the cell interface $(x, \varphi) = (x_{i+1/2}, \varphi_j)$. At an internal cell interface, H is linearized as

$$\hat{H}_{i+\frac{1}{2},j} = \begin{bmatrix} 0 & 1 \\ \hat{R}_{i+\frac{1}{2},j} \frac{\hat{\beta}_{i+\frac{1}{2},j}}{2\rho A_0} - \hat{\alpha}(\hat{u}_{i+\frac{1}{2},j})^2 & 2\hat{\alpha}_{i+\frac{1}{2},j} \hat{u}_{i+\frac{1}{2},j} \end{bmatrix}$$

where the averages are evaluated as

$$\begin{aligned} \hat{u}_{i+\frac{1}{2},j} &= \frac{\frac{Q_{i+1,j}}{\sqrt{A_{i+1,j}}} + \frac{Q_{i,j}}{\sqrt{A_{i,j}}}}{\sqrt{A_{i+1,j}} + \sqrt{A_{i,j}}}, \\ \hat{R}_{i+\frac{1}{2},j} &= \frac{2}{3} \frac{A_{i+1,j} + \sqrt{A_{i+1,j}A_{i+1,j}} + A_{i,j}}{\sqrt{A_{i+1,j}} + \sqrt{A_{i+1,j}}}, \\ \hat{\beta}_{i+\frac{1}{2},j} &= \frac{\beta_{i+1,j} + \beta_{i,j}}{2}, \\ \hat{\alpha}_{i+\frac{1}{2},j} &= \frac{\gamma_{i+1,j} + \gamma_{i,j} + 4}{\gamma_{i+1,j} + \gamma_{i,j} + 2}. \end{aligned}$$

This linearization is identical to Roe's linearization if β and γ are constant (see Appendix C). Roe's linearization cannot be applied if either β or γ is not a constant since equation (2.2.46) does not have a compact form. After linearizing H into \hat{H} at cell interfaces, the jump discontinuities $W_{i+\frac{1}{2},j}^p$ are computed as described in equation (1.4.3). Fluctuations are computed according to the upwind method (1.4.14). Lax-Wendroff (1.4.17) in conjunction with van Leer limiter (1.4.18) is applied for the limited second-order correction term.

Fluxes at the boundary

Dealing with fluxes at the inlet and outlet slightly differs from internal fluxes. The values of A , Q and γ are known at each boundary and used to linearize H . Ghost cells are incorporated to store the values of \mathbf{q} outside the domain. Only one ghost cell is necessary outside each boundary. Ghost cells left of the inlet is evaluated as

$$\mathbf{q}_{i_{in}-\frac{1}{2},j}^n = 2\mathbf{q}_{i_{in},j}^n - \mathbf{q}_{i_{in}+\frac{1}{2},j}^n$$

and right of the outlet as

$$\mathbf{q}_{i_{out}+\frac{1}{2},j}^n = 2\mathbf{q}_{i_{out},j}^n - \mathbf{q}_{i_{out}-\frac{1}{2},j}^n.$$

W^P at each boundary are evaluated identical to internal cell interfaces (see (1.4.3)) once ghost cells are evaluated and H is linearized. The upwind method is forced for waves entering and leaving the domain.

Values at the boundary must be updated every timestep. An axisymmetric velocity boundary condition is applied at the inlet (2.2.38) and the fluid resistance boundary condition (2.1.1) is applied at the outlet. Compatibility conditions at the inlet (1.3.24) and outlet (1.3.25) are applied to obtain both the flow rate and area at each boundary. The eigenvalues and eigenvectors from the previous timestep will be used since the matrix H is linearized, which yields the compatibility conditions

$$\mathbf{l}_1(\mathbf{q}_{i_{in},j}^{n-1}) \left(\partial_t \mathbf{q}_{i_{in},j}^n + \lambda_1(\mathbf{q}_{i_{in},j}^{n-1}) \partial_x \mathbf{q}_{i_{in},j}^n - \begin{bmatrix} 0 & s^x(\mathbf{q}_{i_{in},j}^n) \end{bmatrix}^T \right) = 0 \quad \text{for } x = x_{in}, \quad (2.2.47)$$

$$\mathbf{l}_2(\mathbf{q}_{i_{out},j}^{n-1}) \left(\partial_t \mathbf{q}_{i_{out},j}^n + \lambda_2(\mathbf{q}_{i_{out},j}^{n-1}) \partial_x \mathbf{q}_{i_{out},j}^n - \begin{bmatrix} 0 & s^x(\mathbf{q}_{i_{out},j}^n) \end{bmatrix}^T \right) = 0 \quad \text{for } x = x_{out}. \quad (2.2.48)$$

By applying forward discretization for both temporal and spatial derivatives, the inlet compatibility condition is discretized as

$$\lambda_2(\mathbf{q}_{i_{in},j}^{n-1}) A_{i_{in},j}^{n+1} - Q_{i_{in},j}^{n+1} = \left[\lambda_2(\mathbf{q}_{i_{in},j}^{n-1}) \quad -1 \right] \left(\begin{bmatrix} Q_{i_{in},j}^n + \Delta t s^x(\mathbf{q}_{i_{in},j}^n) \\ A_{i_{in},j}^n \end{bmatrix} - 2 \frac{\lambda_1(\mathbf{q}_{i_{in},j}^{n-1}) \Delta t}{\Delta x} \begin{bmatrix} A_{i_{in},j}^n - A_{i_{in}+\frac{1}{2},j}^n \\ Q_{i_{in},j}^n - Q_{i_{in}+\frac{1}{2},j}^n \end{bmatrix} \right) \quad (2.2.49)$$

By substituting the velocity boundary condition ($Q_{i_{in},j}^{n+1} = v_j^{n+1} A_{i_{in},j}^{n+1}$), area for the new time step is computed as

$$A_{i_{in},j}^{n+1} = \frac{1}{\lambda_2(\mathbf{q}_{i_{in},j}^{n-1}) - v_j^{n+1}} \left[\lambda_2(\mathbf{q}_{i_{in},j}^{n-1}) \quad -1 \right] \left(\begin{bmatrix} Q_{i_{in},j}^n + \Delta t s^x(\mathbf{q}_{i_{in},j}^n) \\ A_{i_{in},j}^n \end{bmatrix} - 2 \frac{\lambda_1(\mathbf{q}_{i_{in},j}^{n-1}) \Delta t}{\Delta x} \begin{bmatrix} A_{i_{in},j}^n - A_{i_{in}+\frac{1}{2},j}^n \\ Q_{i_{in},j}^n - Q_{i_{in}+\frac{1}{2},j}^n \end{bmatrix} \right)$$

By applying forward discretization for time and backward discretization for space, the outlet compatibility condition is discretized as

$$\lambda_1(\mathbf{q}_{i_{out},j}^{n-1}) A_{i_{out},j}^{n+1} - Q_{i_{out},j}^{n+1} = c_1, \quad (2.2.50)$$

where

$$c_1 = \left[\lambda_1(\mathbf{q}_{i_{out},j}^{n-1}) \quad -1 \right] \left(\begin{bmatrix} Q_{i_{out},j}^n + \Delta t s^x(\mathbf{q}_{i_{out},j}^n) \\ A_{i_{out},j}^n \end{bmatrix} - 2 \frac{\lambda_2(\mathbf{q}_{i_{out},j}^{n-1}) \Delta t}{\Delta x} \begin{bmatrix} A_{i_{out}-\frac{1}{2},j}^n - A_{i_{out},j}^n \\ Q_{i_{out}-\frac{1}{2},j}^n - Q_{i_{out},j}^n \end{bmatrix} \right).$$

Substituting the fluid resistance boundary condition into the linear elastic deformation model (1.3.15) yields

$$\begin{aligned} A_{i_{out},j}^n &= \left(\sqrt{A_0} + (P_{i_{out},j}^n - P_0) \frac{A_0}{\beta_{i_{out},j}} \right)^2 \\ &= \left(\sqrt{A_0} + (P_{res} - P_0) \frac{A_0}{\beta_{i_{out},j}} + Q_{i_{out},j}^n R_{res} \frac{A_0}{\beta_{i_{out},j}} \right)^2 \\ &= a_2 \left(Q_{i_{out},j}^n \right)^2 + b_2 Q_{i_{out},j}^n + c_2, \end{aligned} \quad (2.2.51)$$

where

$$\begin{aligned} a_2 &= \left(R_{res} \frac{A_0}{\beta_{i_{out},j}} \right)^2, \\ b_2 &= 2R_{res} \frac{A_0}{\beta_{i_{out},j}} \left(\sqrt{A_0} + (P_{res} - P_0) \frac{A_0}{\beta_{i_{out},j}} \right), \\ c_2 &= \left(\sqrt{A_0} + (P_{res} - P_0) \frac{A_0}{\beta_{i_{out},j}} \right)^2. \end{aligned}$$

Substituting (2.2.51) into (2.2.50) leads to the quadratic equation $\lambda_1 a_2 (Q_{i_{out},j}^{n+1})^2 + (\lambda_1 b_2 - 1) Q_{i_{out},j}^{n+1} + \lambda_1 c_2 - c_1 = 0$. This equation has two solutions. The solution

$$Q_{i_{out},j}^{n+1} = \frac{(1 - \lambda_1 b_2) - \sqrt{(\lambda_1 b_2 - 1)^2 - 4\lambda_1 a_2 (\lambda_1 c_2 - c_1)}}{2\lambda_1 a_2}$$

gives physiological results and is used to update the flow rate at the outlet.

The 2D ROM will also be prescribed with pressure at the inlet (2.2.40) and the non-reflective boundary condition at the outlet for testing purposes. These boundary conditions must also be discretized and connected with the compatibility conditions. From the linear deformation model (1.3.15), we obtain

$$A_{i_{in},j}^{n+1} = \left(\frac{A_0}{\beta} P_{in}((n+1)\Delta t) + \sqrt{A_0} \right)^2. \quad (2.2.52)$$

$Q_{i_{in},j}^{n+1}$ is obtained by substituting (2.2.52) into (2.2.49). The non-reflective boundary condition is for Problem B identical to

$$\mathbf{I}_1(\mathbf{q}) \left(\partial_t \mathbf{q} - \begin{bmatrix} 0 \\ s^x \end{bmatrix} \right) = 0 \quad \text{for } x = x_{out} \quad (2.2.53)$$

By applying forward discretization for the time derivative, the non-reflective boundary condition is discretized as

$$Q_{i_{out},j}^{n+1} = Q_{i_{out},j}^n + \lambda_2 (\mathbf{q}_{i_{out},j}^{n-1}) (A_{i_{out},j}^{n+1} - A_{i_{out},j}^n) + \Delta t s^x (\mathbf{q}^{n-1}). \quad (2.2.54)$$

Substituting (2.2.54) in (2.2.50) yields

$$A_{i_{out},j}^{n+1} = A_{i_{out},j}^n - \frac{2\lambda_2 (\mathbf{q}_{i_{out},j}^{n-1}) \Delta t}{(\lambda_2 (\mathbf{q}_{i_{out},j}^{n-1}) - \lambda_1 (\mathbf{q}_{i_{out},j}^{n-1})) \Delta x} \begin{bmatrix} -\lambda_1 (\mathbf{q}_{i_{out},j}^{n-1}) & 1 \end{bmatrix} \begin{bmatrix} A_{i_{out},j}^n - A_{i_{out}-\frac{1}{2},j}^n \\ Q_{i_{out},j}^n - Q_{i_{out}-\frac{1}{2},j}^n \end{bmatrix}.$$

Discretization of $\partial_x \gamma$ and $\partial_x \beta$

$\partial_x \beta$ and $\partial_x \gamma$ need to be discretized for the source terms for Problem B. $\partial_x \beta$ is set to its analytical value. $\partial_x \gamma$ is discretized with central difference approximation (2.2.44) for cells that are not located at the boundary or not adjacent to the boundary. $\partial_x \gamma$ is discretized at the inlet with the first-order forward discretization

$$\partial_x \gamma_{\frac{1}{2},j}^n = 2 \frac{\gamma_{\frac{1}{2},j}^n - \gamma_{1,j}^n}{\Delta x},$$

and discretized at the outlet with the first-order backward discretization

$$\partial_x \gamma_{n_x+\frac{1}{2},j}^n = 2 \frac{\gamma_{n_x,j}^n - \gamma_{n_x+\frac{1}{2},j}^n}{\Delta x}.$$

These discretizations are first-order accurate and do not incorporate ghost cells. For the cell adjacent to the inlet, $\partial_x \gamma$ is discretized as

$$\partial_x \gamma_{1,j}^n = \frac{-4\gamma_{\frac{1}{2},j}^n + 3\gamma_{1,j}^n + \gamma_{2,j}^n}{3\Delta x}$$

where $\gamma_{\frac{1}{2},j}^n$ is γ at the inlet. For the cell adjacent to the outlet $\partial_x \gamma$ is discretized as

$$\partial_x \gamma_{n_x,j}^n = \frac{-\gamma_{n_x-1,j}^n - 3\gamma_{n_x,j}^n + 4\gamma_{n_x+\frac{1}{2},j}^n}{3\Delta x}$$

where $\gamma_{n_x+\frac{1}{2},j}^n$ is γ at the outlet. These discretizations are second-order accurate and do not incorporate ghost cells. Ghost cells are avoided for the discretization of $\partial_x \gamma$ since the continuity condition (2.2.37) is not satisfied for ghost cells.

Problem C

In this problem, the continuity condition (2.2.4) will be satisfied at the end of each iteration after simulating the Navier-Stokes equation in 2D. Problem C is identical to

$$\partial_\varphi \left(\frac{\gamma+2}{\gamma} \frac{Q}{A} \right) = 0.$$

Problem C does not have a unique solution. By integrating both sides with respect to φ , we obtain

$$\frac{\gamma+2}{\gamma} \frac{Q}{A} = D$$

where $D = v_x|_{r=0}$ does not depend on φ . Our approach to satisfy the continuity condition is to first decide a value for D within each cross section and then correct γ as

$$\gamma_{i,j} = \frac{2u_{i,j}}{D_i - u_{i,j}} \quad (2.2.55)$$

where $u_{i,j} = Q_{i,j}/A_{i,j}$. Three different ways to compute D have been considered.

1) Averaging D is computed as the average

$$D_i = \frac{1}{n_\varphi} \sum_{j=1}^{n_\varphi} D_{i,j}, \quad D_{i,j} := \frac{\gamma_{avg} + 2}{\gamma_{avg}} u_{i,j}, \quad (2.2.56)$$

where γ_{avg} is determined in advance. $\gamma_{i,j}^n = \gamma_{avg}$ leads to an axisymmetric velocity profile. Since a parabolic velocity profile is applied at the inlet, γ_{avg} is set to 2 within this study. From studying the 2D ROM numerically by averaging D , the following was observed:

- Averaging applied to an axial velocity close to 0 m/s leads to negative values for γ if calcification is incorporated.
- γ can obtain negative values if the range of axial velocity within a cross-section is extensive.

2) Maximizing D is computed as the maximum

$$D_i = \max_j D_{i,j}, \quad D_{i,j} := \frac{\gamma_{i,j} + 2}{\gamma_{i,j}} u_{i,j}, \quad (2.2.57)$$

Maximizing D has the following properties:

- γ remains strictly positive if axial velocity within a cross-section is strictly positive.
- γ cannot increase if axial velocity within a cross-section is strictly positive.

These two properties are verified from equation (2.2.55). If axial velocity within a cross-section is strictly positive (or strictly negative), $\text{sgn}(D_{i,j}) = \text{sgn}(u_{i,j})$, and if $|D_{i,j}| < |u_{i,j}|$ (to ensure that γ is strictly positive), we obtain

$$\gamma_{i,j} = \frac{2u_{i,j}}{D_{i,j} - u_{i,j}} \geq \frac{2u_{i,j}}{\max_j \{D_{i,j}\} - u_{i,j}} > 0.$$

These properties were observed by simulating the 2D ROM with calcification and can lead to infinitesimal axial velocity if the calcification is too severe. As a result, obtaining D by maximizing should be avoided.

3) Minimization D is obtained by minimizing

$$f_i := \sum_j \left\| v_{i,j}^c(y) - v_{i,j}(y) \right\|_{L^2(0,1)}$$

where $v_{i,j}^c(y)$ is the corrected velocity profile

$$v_{i,j}^c(y) = D_i(1 - y^{\gamma_{i,j}^c}), \quad \gamma_{i,j}^c = \frac{2u_{i,j}}{D_i - u_{i,j}} > 0,$$

and

$$v_{i,j}(y) = \frac{\gamma_{i,j} + 2}{\gamma_{i,j}} u_{i,j} (1 - y^{\gamma_{i,j}})$$

is the velocity profile before correcting γ . Essentially, γ will be corrected by minimizing the distance between the current velocity profiles and the corrected velocity profiles that satisfy the continuity condition.

This minimization problem is solved by using matlab's built-in function *fmincon*. *fmincon* severely increased the simulation time. The minimization problem was avoided as a consequence. Obtaining D from solving the minimization problem could be used if terms obtained from the problematic integral (2.2.32) could be neglected.

The 2D numerical method cannot deal with zero velocity. Updating γ according to equation (2.2.55) leads to $\gamma = 0$ when the velocity is zero within a cross section. $\gamma = 0$ is not within the solution space since the 2D Navier-Stokes equation (2.2.36) and the continuity condition (2.2.37) are singular for $\gamma = 0$. Remark that the normalization property $\int_0^1 y s(y, \gamma) dy = \frac{1}{2}$ cannot even be satisfied for $\gamma \downarrow 0$ since $\lim_{\gamma \downarrow 0} s(y, \gamma) \equiv 0$.

Problem C is being solved heuristically. Problem C is akin to conserving mass for the 3D Navier-Stokes equation within a rigid body. Only satisfying the balance of momentum equation leads to velocity that does not conserve mass. A pressure-correction method can be applied for the 3D Navier-Stokes equation [5] to satisfy the conservation of mass equation. Predictor-corrector methods, similar to the pressure-correction method for the Navier-Stokes equations, should more accurately simulate the 2D ROM.

Dealing with discontinuities

The described numerical methods cannot properly deal with discontinuities in β . However, medial calcification will be modeled as

$$\beta = \begin{cases} \beta_C & \text{for } (x, \varphi) \in I_C, \\ \beta_H & \text{for } (x, \varphi) \notin I_C, \end{cases}$$

where $I_C = [x_1, x_2] \times [\varphi_1, \varphi_2] \subset \Omega$ is a rectangular calcified region and β_C / β_H contains mechanical properties of calcification/healthy artery respectively. A modeling error is made by smoothing the discontinuity to simulate blood flow with medial calcification. This smoothing process is done one-way, by letting the smooth transition only occur in the healthy region of the artery. Let $\Delta\xi$ be the length of the smooth transition, and let

$$d(\mathbf{x}, I_C) = \min_{(y, \theta) \in I_C} \sqrt{\left(\frac{x-y}{\xi^x}\right)^2 + \left(\frac{\varphi-\theta}{\xi^\varphi}\right)^2}$$

be a mapping that measures the distance between $\mathbf{x} \in \Omega$ and I_C , in which ξ^x and ξ^φ are strictly positive scalars determined in advanced. For every $(x, \varphi) \in \Omega$, there exist a unique $(x_{min}, \varphi_{min}) \in I_C$ such that

$$d(\mathbf{x}, I_C) = \sqrt{\left(\frac{x-x_{min}}{\xi^x}\right)^2 + \left(\frac{\varphi-\varphi_{min}}{\xi^\varphi}\right)^2}. \quad (2.2.58)$$

Furthermore, x_{min} and φ_{min} ¹ are determined as

$$x_{min} = \begin{cases} x_1 & \text{for } x \leq x_1, \\ x & \text{for } x_1 < x \leq x_2, \\ x_2 & \text{for } x_2 \leq x, \end{cases} \quad \text{and} \quad \varphi_{min} = \begin{cases} \varphi_1 & \text{for } \varphi \leq \varphi_1, \\ \varphi & \text{for } \varphi_1 < \varphi \leq \varphi_2, \\ \varphi_2 & \text{for } \varphi_2 \leq \varphi. \end{cases}$$

The one-way smooth transition $\beta_T : [0, \Delta\xi] \rightarrow [\beta_H, \beta_C]$ is the decreasing mapping

$$\beta_T(\xi) = \frac{\beta_H + \beta_C}{2} - \frac{\beta_H - \beta_C}{2} \cos\left(\frac{\pi\xi}{\Delta\xi}\right). \quad (2.2.59)$$

¹ φ_{min} is determined without caring about wrapping. This only works if calcification is placed in the center of the azimuthal domain. Due to periodic boundary conditions, φ can always be translated to centralize the calcification.

Calcification with the one-way smooth transition error is evaluated as

$$\beta(\mathbf{x}) = \begin{cases} \beta_C & \text{for } d(\mathbf{x}, I_C) = 0, \\ \beta_T(d(\mathbf{x}, I_C)) & \text{for } 0 < d(\mathbf{x}, I_C) < \Delta\xi, \\ \beta_H & \text{for } d(\mathbf{x}, I_C) \geq \Delta\xi, \end{cases} \quad (2.2.60)$$

and has the derivative

$$\partial_x \beta(\mathbf{x}) = \begin{cases} 0 & \text{for } d(\mathbf{x}, I_C) = 0, \\ (\xi^x)^{-2} \frac{x-x_{min}}{d(\mathbf{x}, I_C)} \frac{\pi}{\Delta\xi} \frac{\beta_H - \beta_C}{2} \sin\left(\frac{\pi d(\mathbf{x}, I_C)}{\Delta\xi}\right) & \text{for } 0 < d(\mathbf{x}, I_C) < \Delta\xi, \\ 0 & \text{for } d(\mathbf{x}, I_C) \geq \Delta\xi. \end{cases} \quad (2.2.61)$$

Except for unique cases $\Delta\xi$ will be set to 1. The smoothening area depends on the variables ξ^x and ξ^φ . $\beta(\mathbf{x})$ is sketched in Figure 2.7.

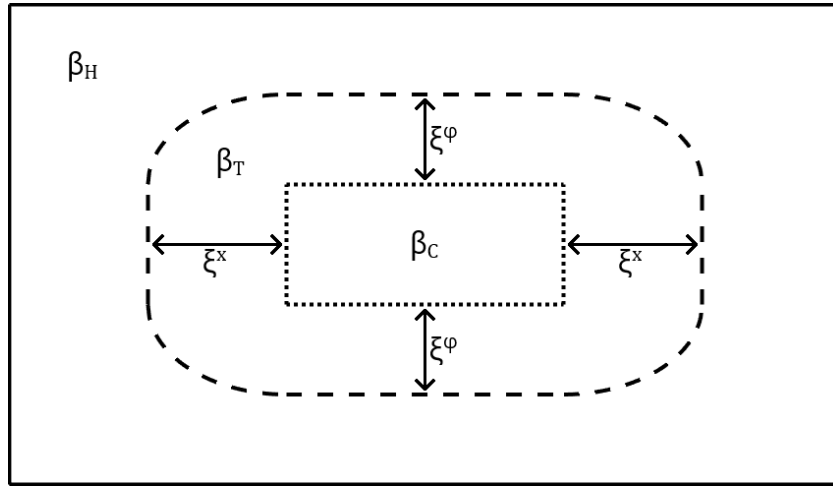


Figure 2.7: Sketch of $\beta(\mathbf{x})$ by smoothening the jump discontinuity. The dotted line shows the boundary of the calcified area I_C and the dashed line is parameterized by $d(\mathbf{x}, I_C) = 1$. β_H , β_T , and β_C contain mechanical properties of the artery within the healthy, smoothening, and calcified regions, respectively.

2.2.5. Steady-state solutions

The last course of action for the 2D ROM is investigating steady-state solutions. A system of differential equations is said to be steady if time does not affect the system's state. Hence, the asymmetric flow model is steady if $\partial_t A = \partial_t Q = \partial_t \gamma = 0$. The steady-state solution depends on the boundary condition applied at the system. Two steady-state problems will be investigated for the asymmetric flow model since two sets boundary conditions are studied.

Prescribe pressure at the inlet

By applying pressure at the inlet and the non-reflective boundary condition at the outlet, the asymmetric flow model has the following steady-state problem:

Find $A \in C^2(\Omega)$, $Q \in C^1(\Omega)$ and $\gamma \in C^2(\Omega)$ such that

$$\begin{cases} H(\mathbf{q}, \gamma; \beta) \partial_x \mathbf{q} = \begin{bmatrix} 0 \\ s^x + s^\varphi \end{bmatrix}, \\ \partial_\varphi(g(\mathbf{q}, \gamma)) = 0, \\ A = \left(\sqrt{A_0} + (P_{in} - P_0) \frac{A_0}{\beta} \right)^2 \text{ for } x = 0, \\ s^x + s^\varphi = 0 \text{ for } x = x_{out}, \\ \mathbf{q}|_{\varphi=0} = \mathbf{q}|_{\varphi=2\pi}, \\ \gamma|_{\varphi=0} = \gamma|_{\varphi=2\pi}. \end{cases} \quad (2.2.62)$$

The conservation of mass equation is steady if $\partial_x Q = 0$, and the non-reflective boundary condition is steady if $Q = 0$ for $x = x_{out}$. Combining these two equations leads to a vanishing volumetric flow rate for the steady state problem (2.2.62). For $Q = 0$, the balance of momentum equation is steady if $\partial_x P = 0$. By applying the linear elastic deformation model, a steady-state solution is found for (2.2.62) if $Q = 0$ and

$$A(x, \varphi) = \left(\sqrt{A_{in}(\varphi)} \frac{\beta(0, \varphi)}{\beta(x, \varphi)} + \sqrt{A_0} \left(1 - \frac{\beta(0, \varphi)}{\beta(x, \varphi)} \right) \right)^2. \quad (2.2.63)$$

This steady-state solution is not unique within the solution space, since this steady state solution is satisfied for all $\gamma \in C^2(\Omega)$. However, the shape of the velocity profile does not affect blood flow for $Q = 0$.

Prescribe velocity at the inlet

By prescribing mean axial velocity at the inlet and the fluid resistance boundary condition (2.1.1) at the outlet, the asymmetric flow model has the following steady-state problem:

Find $A \in C^2(\Omega)$, $Q \in C^1(\Omega)$ and $\gamma \in C^2(\Omega)$ such that

$$\begin{cases} H(\mathbf{q}, \gamma; \beta) \partial_x \mathbf{q} = \begin{bmatrix} 0 \\ s^x + s^\varphi \end{bmatrix}, \\ \partial_\varphi(g(\mathbf{q}, \gamma)) = 0, \\ Q = v_{in} A \text{ for } x = 0, \\ P_0 + \frac{\sqrt{A} - \sqrt{A_0}}{A_0} \beta = P_{res} + QR_{res} \text{ for } x = x_{out}, \\ \mathbf{q}|_{\varphi=0} = \mathbf{q}|_{\varphi=2\pi}, \\ \gamma|_{\varphi=0} = \gamma|_{\varphi=2\pi}. \end{cases} \quad (2.2.64)$$

A steady state solution can be obtained for (2.2.64) if $\partial_x \beta = 0$ within an axisymmetric setting, i.e. A , Q , and γ are independent of φ . In these settings and by taking $\gamma = 2$, equation (2.2.64) is reduced into

$$\partial_x Q = 0,$$

$$\left(\frac{\beta \sqrt{A}}{2\rho A_0} - \frac{4}{3} \frac{Q^2}{A^2} \right) \partial_x A = -8 \frac{\mu}{\rho} \frac{Q}{A}, \quad (2.2.65)$$

$$A = A_{in}(Q) := \frac{Q}{v_{in}} \text{ for } x = x_{in}, \quad (2.2.66)$$

$$A = A_{out}(Q) := \left(\sqrt{A_0} + (P_{res} - P_0) \frac{A_0}{\beta} + QR_{res} \frac{A_0}{\beta} \right)^2 \text{ for } x = x_{out}. \quad (2.2.67)$$

An analytical expression for the steady-state problem of the balance of momentum equation (2.2.65) can be found by applying separation of variables, which yields

$$\begin{aligned} & \int_0^x \left(\frac{\beta}{2\rho A_0} A^{\frac{3}{2}} - \frac{4}{3} \frac{Q^2}{A} \right) \partial_x A dx = - \int_0^x 8 \frac{\mu}{\rho} Q dx \\ \Rightarrow & \frac{\beta}{5\rho A_0} \left(A^{\frac{5}{2}}(x) - A^{\frac{5}{2}}(Q) \right) - \frac{4}{3} Q^2 (\ln A(x) - \ln A_{in}(Q)) = -8 \frac{\mu}{\rho} Qx. \end{aligned} \quad (2.2.68)$$

Satisfying (2.2.68) for $x = x_{out}$ yields

$$\frac{\beta}{5\rho A_0} \left(A_{out}^{\frac{5}{2}}(Q) - A_{in}^{\frac{5}{2}}(Q) \right) - \frac{4}{3} Q^2 (\ln A_{out}(Q) - \ln A_{in}(Q)) = -8 \frac{\mu}{\rho} Q x_{out}. \quad (2.2.69)$$

Q is the only unknown in (2.2.69), however Q cannot be obtained analytically. Once if Q is known, $A(x)$ can be obtained numerically from (2.2.68). The steady-state solution of the balance of momentum equation (2.2.68) will be used to determine the numerical error.

Steady-state solutions are obtained numerically with $A_0 = 0.0625 \text{ cm}^2$ ($R_0 = 0.25 \text{ cm}$), $\rho = 1.060 \text{ g/cm}^3$, $\mu = 0.03 \text{ P}$ ($0.003 \text{ Pa}\cdot\text{s}$), $v_{in} = 8.41199 \text{ cm/s}$, $P_0 = 0 \text{ kPa}$, $P_{res} = 9330 \text{ Pa}$ and $R_{res} = 1.358 \text{ E9 Pa s / m}^3$, $\beta = \frac{4}{3} E h$, $h = 0.05 \text{ cm}$ and $E = 0.6 \text{ MPa}$. Incorporating matlab's built in function 'vpasolve' to solve (2.2.68) and (2.2.69) numerically yields two real solutions. One steady-state solution leads to a volumetric flow rate of $1398 \text{ cm}^3/\text{s}$ and inner wall radii larger than 27500 cm . This non-physiological solution has been neglected from this study. The other steady-state solution has a volumetric flow rate of $0.5982 \text{ cm}^3/\text{s}$. It is depicted in Figure 2.8¹. The physiological steady-state solution is obtained with a maximum error of $5.392\text{E-}13$.

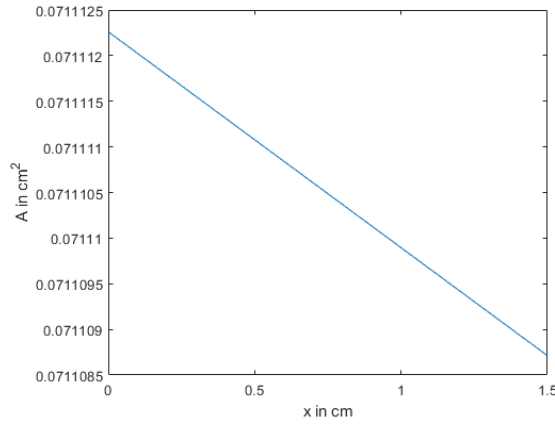


Figure 2.8: Steady-state solutions without calcification by prescribing mean axial velocity at the inlet. $A = R^2$ corresponds to the steady-state solution in the 2D framework.

2.3. 3D simulations

Simulations in 3D will be used as a benchmark to determine the accuracy of the 2D ROM. The open-source finite element software package FEBio (version 2.8.1) [13] is utilized to conduct 3D FSI simulations. FEBio incorporates biphasic-theory, that allows for flow within a porous medium. As a consequence, fluids used for FSI simulations within FEBio have a fluid and a solid component, leading to fluid and solid meshes. However, FEBio only includes the solid mesh. The fluid mesh is related with the solid mesh by incorporating a fluid 'bulk modulus'. Readers interested in FEBio are advised to read [13] and [24].

This section describes the process of constructing an FSI model and performing simulations in FEBio.

2.3.1. Mesh

The artery consists of two parts: the lumen and the vascular wall. Both parts are discretized as structured meshes. The lumen is created as a cylinder with a radius of 0.25 cm and a height of 1.5 cm . A wedge-centered mesh is constructed with a ratio of 0.5 , 12 slices (azimuthal domain is split into 48 parts), 15 segments (radial domain is split into 15 parts), 120 stacks (axial dimension is split into 120 parts), a z -bias of 1 (all stacks have an equal size), and an r -bias of 1 (all segments have an equal size). The mesh is shown in Figure 2.9a. The vascular wall has a thickness of 0.05 cm and is split into three segments (see figure 2.9b). No sensitivity analysis has been conducted on this mesh. Hence, results from the 3D simulations should be taken with a grain of salt.

¹Values within the steady-state solutions are given within the context of the 2D ROM.

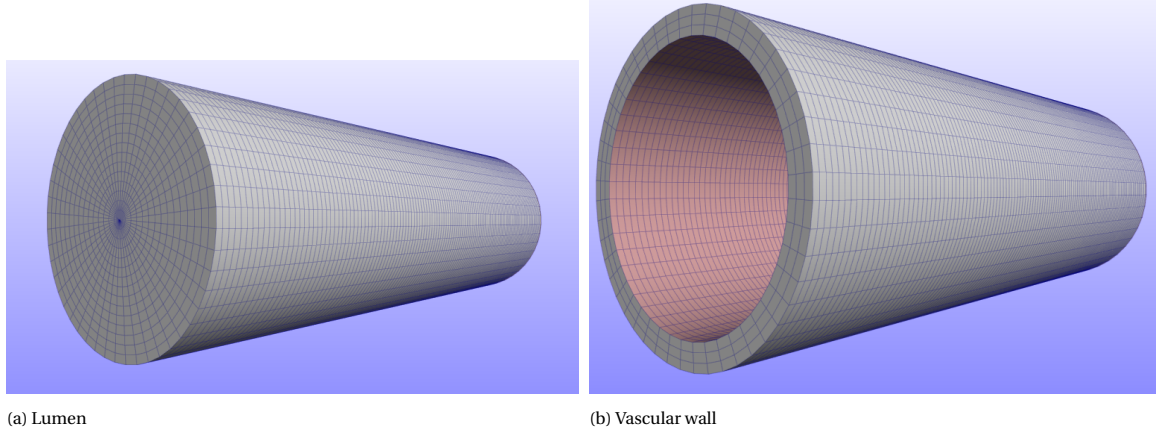


Figure 2.9: Mesh used in FEBio

2.3.2. Calcification

Calcification is applied for $z \in [0.5, 1]^1$, which is located in the middle of the artery. If calcification is applied, it is either applied axially (see Figure 2.10a) or locally for $\varphi \in [\frac{3}{4}\pi, \frac{5}{4}\pi]$ (see Figure 2.10b). Only the tunica media is calcified for medial calcification, whereas all layers within the vascular wall are calcified within the 2D and 3D models. The 3D model calcifies all layers because the 2D ROM cannot apply Young's modulus across different layers in the vascular wall.

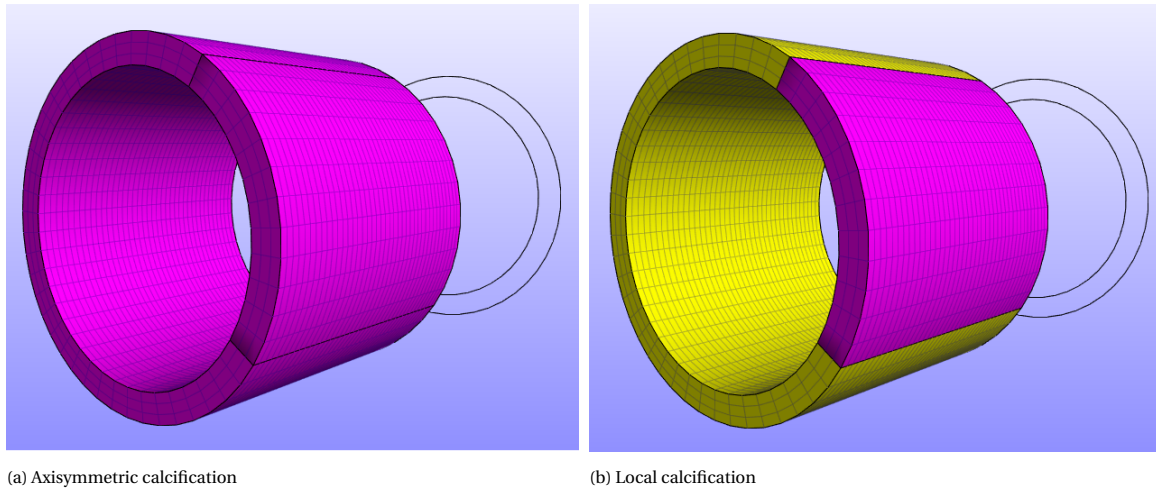


Figure 2.10: Calcification of vascular wall. Yellow and purple colored elements are vascular tissue and calcification.

2.3.3. Materials

Blood in FEBio is configured identically to Ramya's study [20]. Blood is modeled as a fluid-FSI material, containing a solid and fluid parts. The solid part of blood is modeled as a Neo-Hookean model, with a density of 0 kg/m^3 , a Young's modulus of $1\text{e-}15 \text{ Pa}$, and a Poisson ratio of 0. The fluid part of blood has a density of 1060 kg/m^3 and a bulk modulus of $2.2\text{e}9 \text{ Pa}$. Its viscosity is modeled as a Newtonian fluid, with a bulk viscosity of 0 Pa s , and a shear viscosity of 0.0035 Pa s .

The linear elastic model will be used to model the three dimensional deformations due to its simplicity while also being used to research calcification [1]. The vascular wall is modeled as a linear isotropic elastic material. Both healthy tissue and calcification have a density of 1000 kg/m^3 and a Poisson's ratio of 0.48. Healthy tissue has a Young's modulus of 0.6 MPa whereas calcification has a Young's modulus of 10 MPa [1].

¹The z -axis is the axial coordinate in FEBio. The 2D and 1D ROM described in this paper uses the x -axis as axial coordinate.

2.3.4. Boundary conditions

A parabolic velocity profile will be applied at the inlet and a fluid resistance boundary condition will be applied at the outlet. The load curve

$$l(t; t_{start}, t_{end}, y_{start}, y_{end}) = \begin{cases} y_{start} & \text{for } t < 0, \\ \frac{y_{end} + y_{start}}{2} - \frac{y_{end} - y_{start}}{2} \cos\left(\pi \frac{t - t_{start}}{t_{end} - t_{start}}\right) & \text{for } t_{start} < t < t_{end}, \\ y_{end} & \text{for } t > t_{end}, \end{cases} \quad (2.3.1)$$

where $t_{start} = 0$, $t_{end} = 0.2$, $y_{start} = 0$ and $y_{end} = 1$ is applied to P_{res} and R_{res} . This load curve is multiplied with P_{res} and R_{res} to ensure that $P_{res}(t)$ and $R_{res}(t)$ are slowly increasing, which prevents elements to become non-physiological.

The kinematic and dynamic coupling conditions also need to be implemented. Applying a non-slip boundary condition is sufficient for the kinematic coupling condition. A zero fluid velocity boundary condition is applied to every node that is an element of both lumen and the vascular wall. The dynamic coupling condition is applied as a fluid-FSI traction load to every faces that is an element of both lumen and the vascular wall.

Assumption 1 *Radial displacement* will also be implemented. This is done by adding a zero y-displacement to every node in the vascular wall with an x position of 0 and a zero x-displacement to every node in the vascular wall with a y position of 0.

The last set of boundary conditions are incorporated to ensure that the 2D mesh can be reconstructed with the 3D mesh. This is done by adding a zero z-displacement to all nodes and a zero x-displacement and a zero y-displacement to every node within the artery's origin, i.e., every node with an x-position and a y-position of zero.

2.3.5. Simulation

The simulation has a time step size of 0.001s. All remaining properties are identical to FEBio's default setting. The following tables depict all simulation configurations.

Table 2.1: Common control parameters

Parameter	Value
analysis	DYNAMIC
time_steps	2592
step_size	0.001 s
adaptor_resolve	1
Auto time stepper	(none)

Table 2.2: Common solver parameters

Parameter	Value
dtol	0.001
vtol	0.001
ftol	0.001
etol	0.01
rtol	0.001
rhoi	(none)
predictor	0
min_volume_ratio	0
order	2
linear_solver	(none)

Table 2.3: Linear system parameters

Parameter	Value
matrix format	preferred
equation_scheme	default
optimize_bw	false

Table 2.4: Line search parameters

Parameter	Value
lstol	0.9
lsmin	0.01
lsiter	5
ls_check_jacobians	false

Table 2.5: Nonlinear solver parameters

Parameter	Value
max_refs	5
check_zero_diagonal	false
zero_diagonal_tol	0
force_partition	0
reform_each_rime_step	false
reform_augment	false
diverge_reform	false
min_residual	1e-20
max_residual	1e20

Table 2.6: Quasi-Newton solver parameters

Parameter	Value
Quasi-Newton method	Broydon
max_ups	50
max_buffer_size	0
cycle_buffer	true
cmax	1e5

3

Results

This chapter uses three different calcification models to discuss the 2D and 3D simulation results. Unless stated otherwise, all calcification models have identical properties except for the location of calcification (I_C). All arteries have a length of 1.5 cm and a reference radius of 0.25 cm ($A_0 = 0.0625 \text{ cm}^2$). Their walls have a thickness of 0.05 cm, a Poisson's ratio of 0.48, and a Young's modulus of either 0.6 MPa if $(x, \varphi) \notin I_C$ or 10 MPa if $(x, \varphi) \in I_C$. I_C depends on the calcification model. This study focuses on the following three calcification models:

Model 1 *No calcification*: $I_C = \emptyset$.

Model 2 *Axisymmetric calcification*: $I_C = [0.5, 1] \times [0, 2\pi]$.

Model 3 *Local calcification*: $I_C = [0.5, 1] \times [\frac{3}{4}\pi, \frac{5}{4}\pi]$.

This chapter starts by investigating 2D simulations without pulsatile flow, in which each calcification model is discussed in a separate section. It then proceeds to compare 2D and 3D simulations with pulsatile flow.

3.1. Simulations without calcification

This section focuses on 2D simulations without calcification and without a pulsatile flow. The 2D model becomes axisymmetric once the inlet and calcification models are axisymmetric. The 1D theory will be applied to determine how well the 2D numerical method solves a 1D problem.

3.1.1. Upwind, Lax-Wendroff, and high-resolution methods

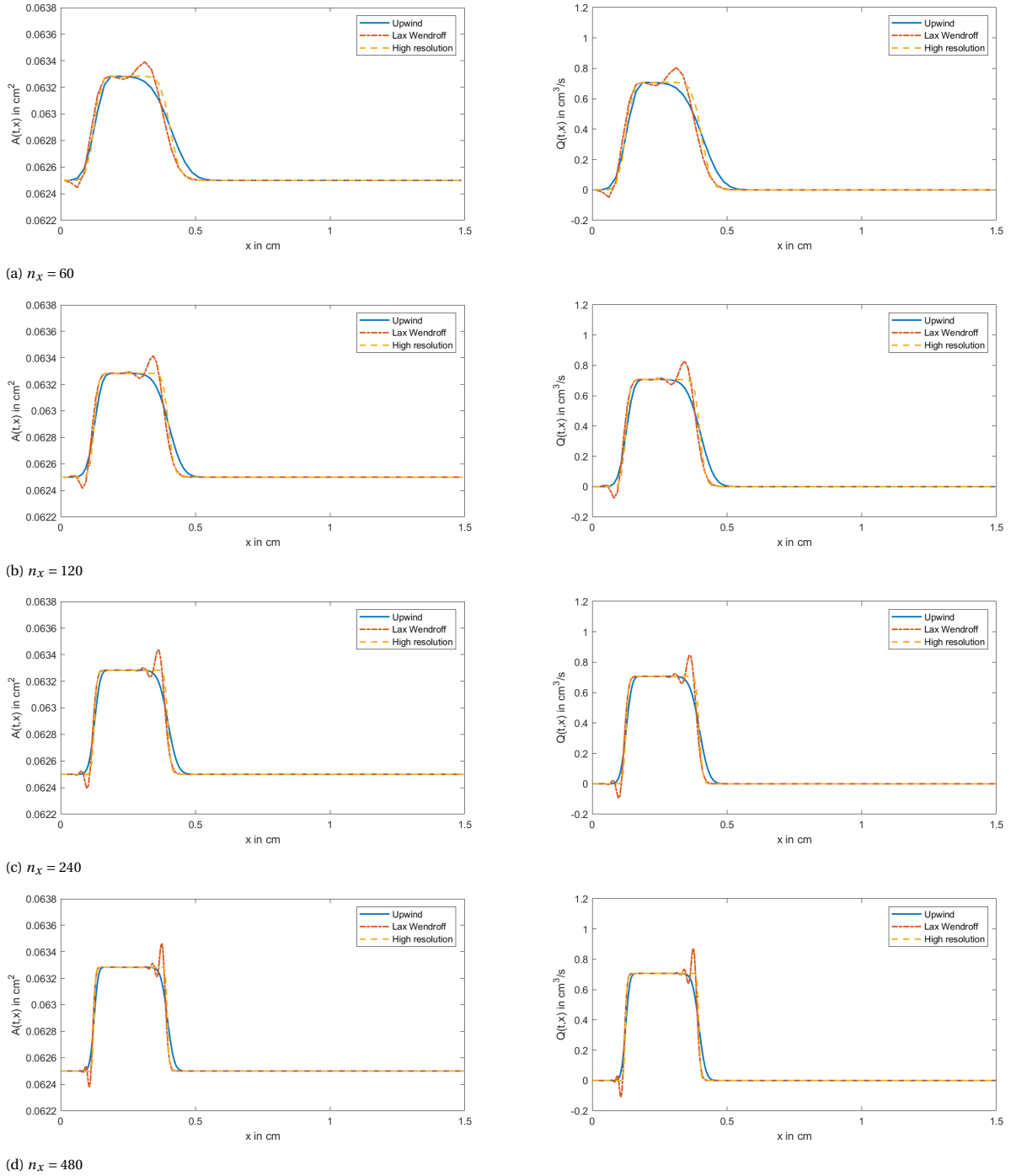
The x -sweep is simulated by a high-resolution method, which combines the upwind method as a lower-order method and Lax-Wendroff as a higher-order correction (see Problem B in Section 2.2.4). In this section, we will verify if the three methods yield the expected results from theory. The numerical methods for the upwind and Lax-Wendroff are obtained by applying the high-resolution method while fixing the limiter function to 0 or 1, respectively.

Theory dictates that the upwind method is first-order accurate and that the Lax-Wendroff is second-order accurate, which leads to numerical diffusion for the upwind method and numerical dispersion for the Lax-Wendroff method. These traits also occur for the 2D simulations with the following specifications:

- $n_x = 60 \cdot 2^r$ and $\Delta x = 1.5/n_x = 0.025 \cdot 2^{-r}$ cm where $r \in \{0, 1, 2, 3, 4, 5, 6\}$.
- $\Delta t = 17.5 \cdot 2^{-r}$ μs where $r \in \{0, 1, 2, 3, 4, 5, 6\}$.
- $n_\varphi = 24$.
- Initial solution: $A|_{t=0} = A_0$ and $Q|_{t=0} = 0 \text{ cm}^3/\text{s}$.
- A pressure block pulse at the inlet described as

$$P_{in}(t) = \begin{cases} 10 \text{ kPa} & \text{for } 0 \leq t < 0.3 \text{ ms,} \\ 0 \text{ kPa} & \text{for } t \geq 0.3 \text{ ms.} \end{cases} \quad (3.1.1)$$

Figure 3.1 shows the simulation at $t = 0.46$ ms and Figure 3.2 shows the simulation at $t = 1.3$ ms. The pulse block wave propagates from the inlet towards the outlet for all simulations. The speed of the pulse block is identical across the three numerical schemes. For the upwind method, the pulse block diffuses. The diffusion is less noticeable for larger values of n_x than lower values. The pulse block wave shows numerical dispersion for the Lax-Wendroff; wiggles are formed on the left side of each jump discontinuity since the pulse block wave is moving right. The magnitude of these wiggles increases as n_x increases. The high-resolution method will be used for all future simulations. This numerical scheme diffuses less than the upwind method without showing signs of wiggles.



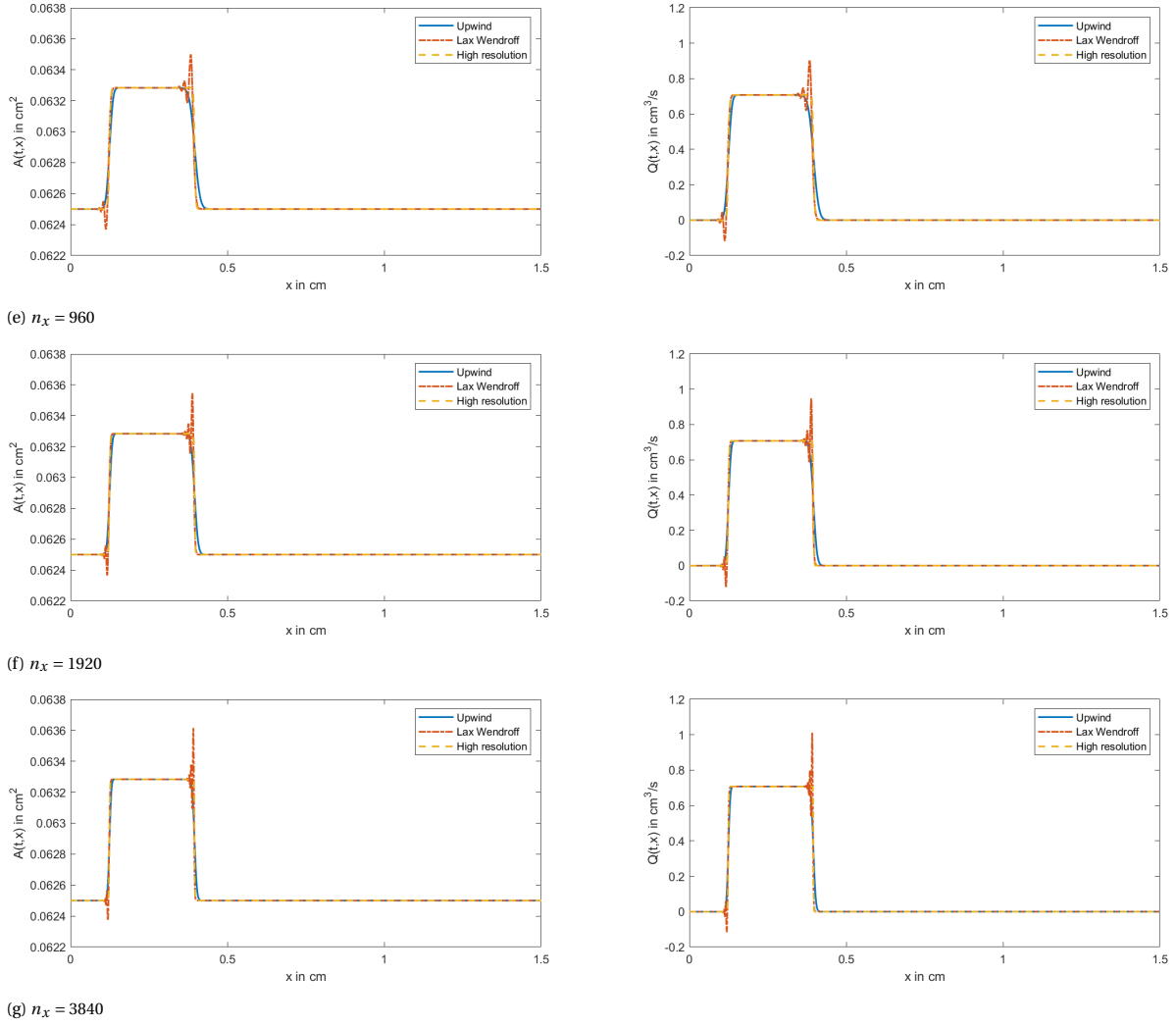


Figure 3.1: Simulations for the upwind, Lax-Wendroff, and high-resolution method at $t = 0.46\text{ms}$. n_x denotes the total number of discrete cross-sections.

3.1.2. Numerical stability

Theory dictates that the high-resolution method applied to a linear hyperbolic problem is stable if the Courant number is smaller than or equal to 1 [12]. In this section, we will study the stability of the high-resolution method applied to the 2D ROM without calcification. The following numerical specifications are used:

- $A|_{t=0} = A_0$ and $Q|_{t=0} = 0$ as initial solution.
- A pressure of 10 kPa at the inlet and non-reflective boundary conditions at the outlet.
- $n_x = 60$ ($\Delta x = 0.25$ mm).
- $n_\varphi = 1$ (since the system is axisymmetric).
- $10\ \mu\text{s} \leq \Delta t \leq 40\ \mu\text{s}$, with a step-size of $0.1\ \mu\text{s}$.
- Simulated for 8 ms. This is enough time for the wave from the inlet to propagate to the outlet, back to the inlet, and then back to the outlet.

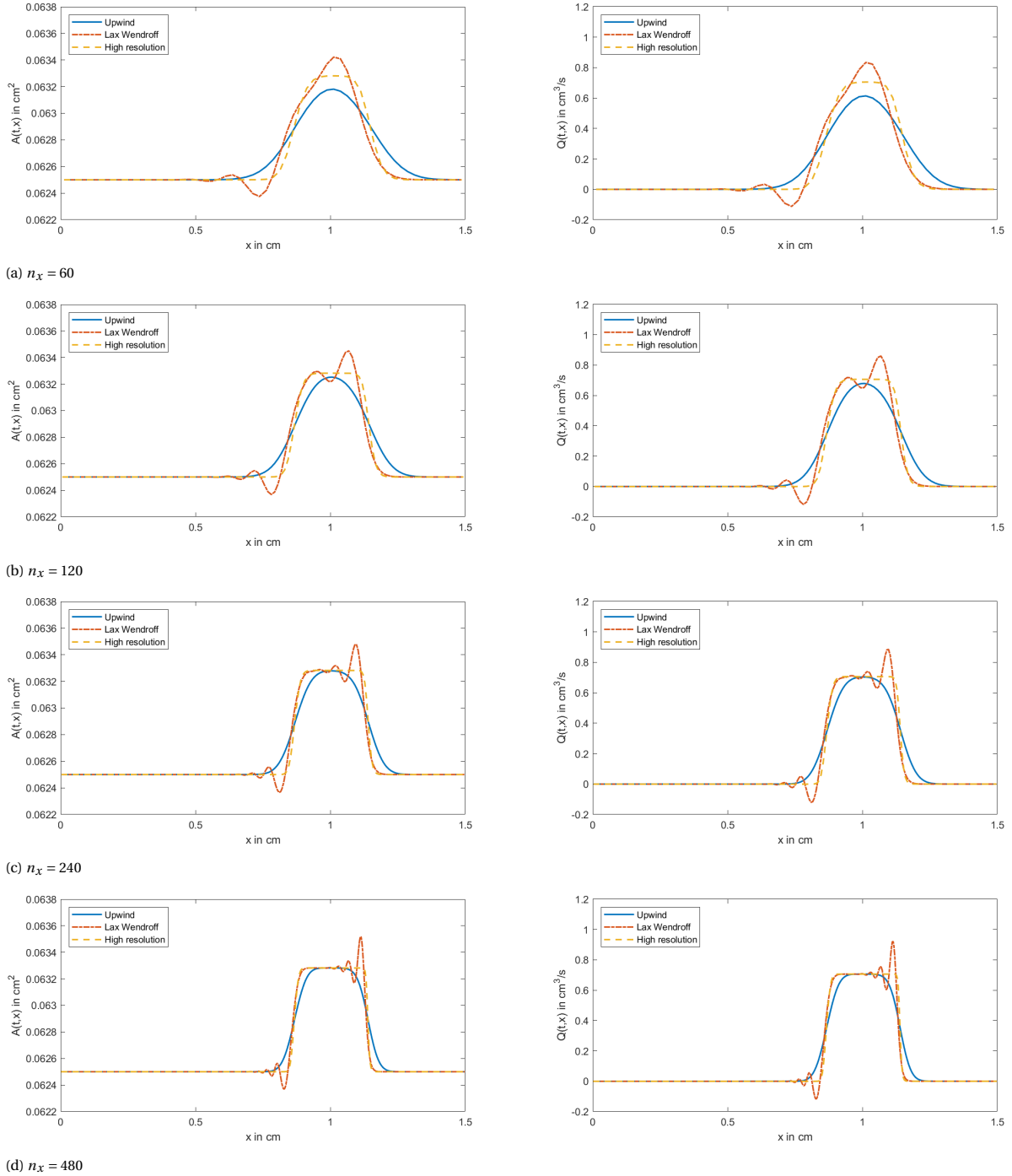
Figure 3.3 shows how the maximum observed Courant number depends on Δt . The numerical method remains stable if $\Delta t \leq 23.2\ \mu\text{s}$, which leads to a Courant number less than or equal to 0.999. The maximum observed Courant number depends linearly on Δt for $\Delta t \leq 21.5\ \mu\text{s}$. The maximum observed Courant number oscillates for Δt between $21.5\ \mu\text{s}$ and $23.2\ \mu\text{s}$. The numerical method was unstable for $\Delta t \geq 23.3\ \mu\text{s}$.

The discretization of the boundary and compatibility conditions at the inlet leads to an oscillating right-going wave if Δt is too large (see Figure 3.4a). However, the amplitude of this oscillating wave reduces if the

Courant number is smaller than 1 (see Figure 3.4b) and increases if the Courant number is significantly larger than 1 (see Figure 3.5). The right-going wave did not oscillate for $\Delta t \leq 1.5 \mu\text{s}$ (see Figure 3.6). Oscillations in maximum Courant number (see in Figure 3.3 for Δt between $21.5 \mu\text{s}$ and $23.2 \mu\text{s}$) most likely occur due to the right-going oscillating waves not being damped before reaching the outflow boundary condition. In those cases, the maximum observed Courant number depends on how the oscillating wave reaches the outflow boundary condition.

3.1.3. Steady-state solutions

Lastly, we will verify if the numerical method for the 2D ROM can obtain a steady-state solution and how accurate the steady-state solution is obtained. Steady-state solutions are numerically obtained by simulating



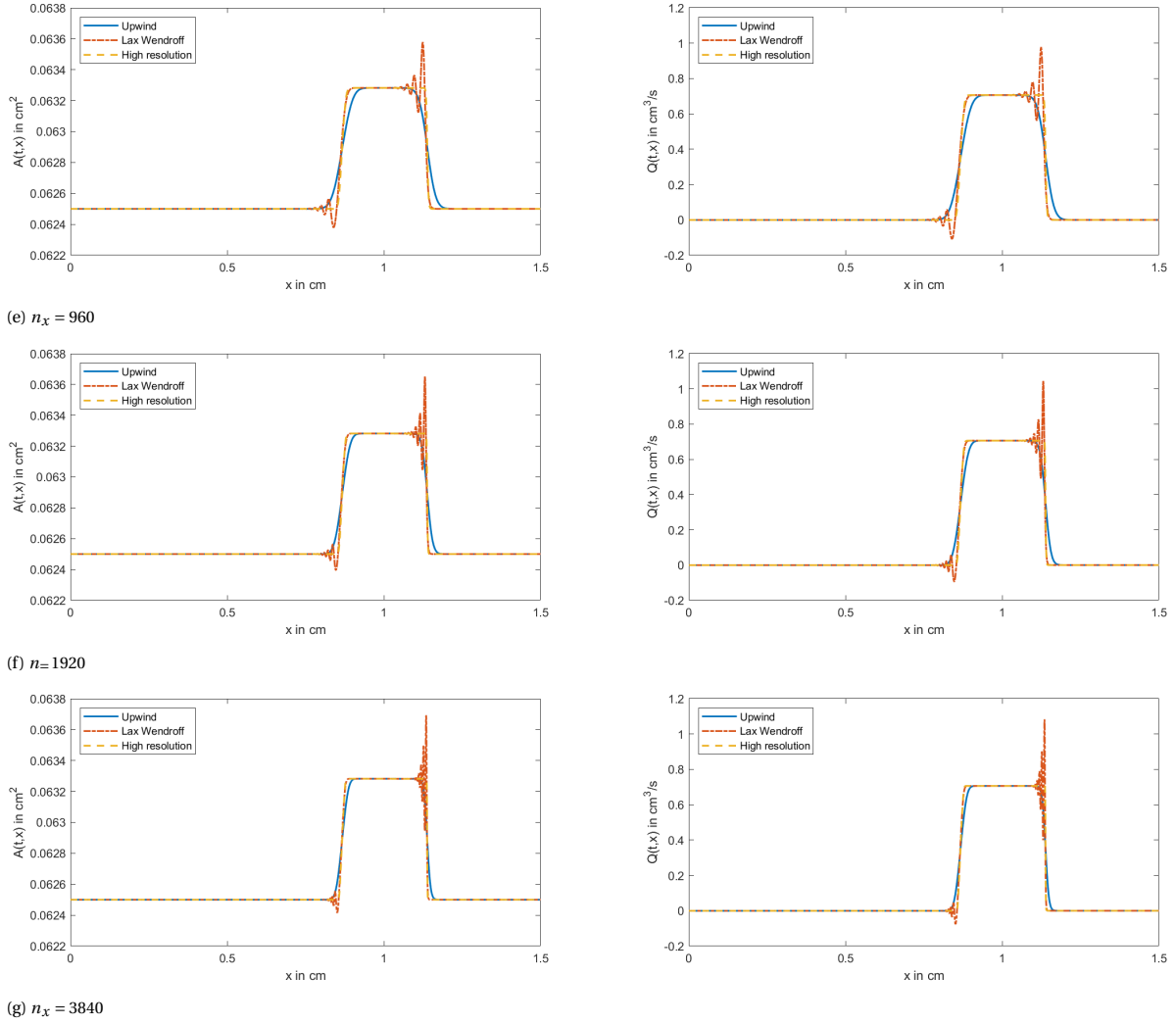


Figure 3.2: Simulations for the upwind, Lax-Wendroff, and high-resolution method at $t = 1.3\text{ms}$. n_x denotes the total number of discrete cross-sections.

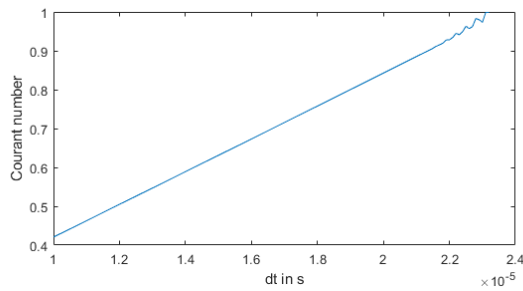


Figure 3.3: Maximum observed Courant number dependent on timestep size (no calcification).

the time dependent problem until the margin of error is small enough. Numerical steady-state solutions are studied for two different sets of boundary conditions. The first set of boundary conditions combines a fixed pressure of 10 kPa at the inlet with a non-reflective boundary condition at the outlet. The second set of boundary conditions prescribes a fixed mean axial velocity of 8.41199 cm/s at the inlet and a fluid resistance boundary condition (2.1.1) at the outlet with $P_{res} = 9330\text{ Pa}$ and $R_{res} = 1.358\text{ E9 Pa s / m}^3$. A mean axial velocity of 8.41199 cm/s is used since this velocity is the minimum prescribed velocity for simulations with pulsatile flow (see Figure 2.2). The following numerical specifications are used:

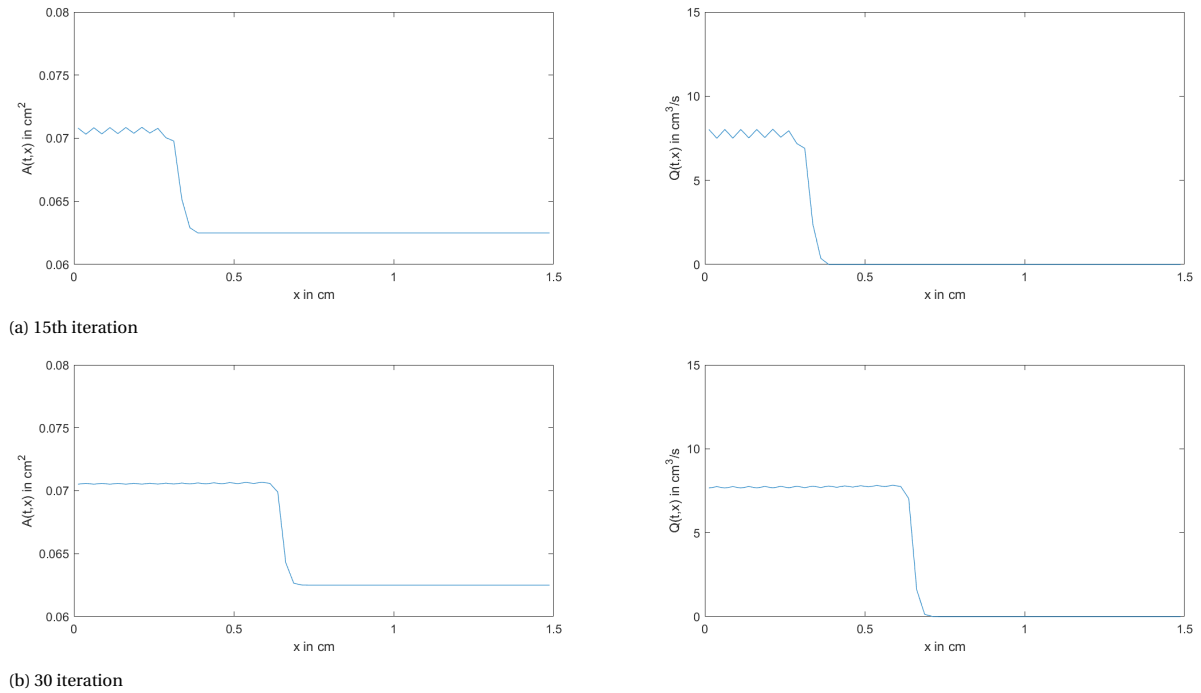


Figure 3.4: Blood flow without calcification simulated with a time step size of 22.5 μ s.

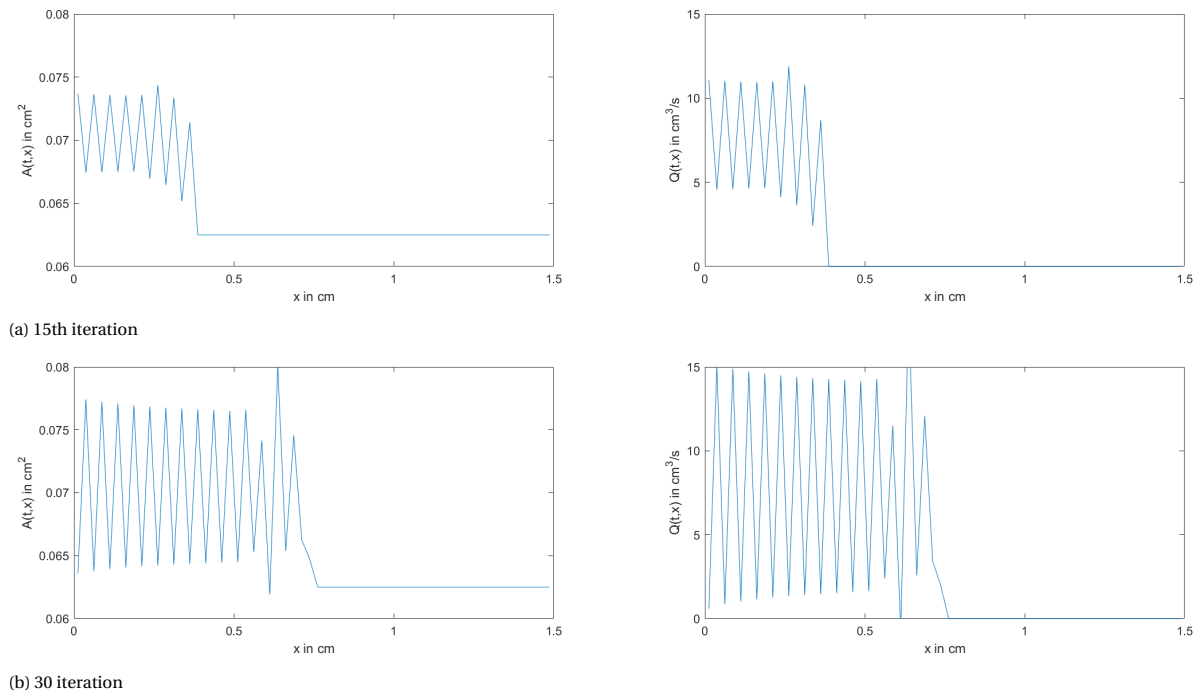


Figure 3.5: Blood flow without calcification simulated with a time step size of 24.5 μ s.

- $A|_{t=0} = A_0$ and $Q|_{t=0} = 0$ as initial solution.
- $n_x \in \{30, 60, 90, 120, 150, 180, 210, 240\}$.
- $n_\varphi = 1$ (since the system is axisymmetric).
- $\Delta t = 22 \cdot 60 / n_x \mu$ s (such that the Courant number is independent of n_x).
- Simulations stops if four stopping criteria have been satisfied with $\varepsilon = 10^{-4}$. The first three stopping criteria

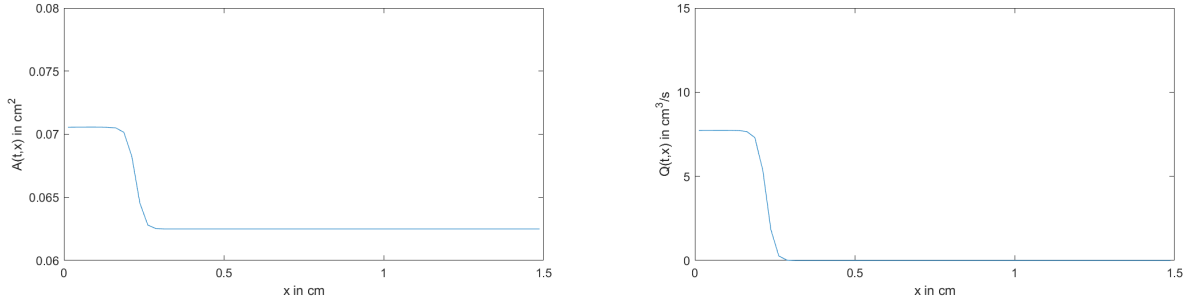


Figure 3.6: The 15th iteration of blood flow without calcification simulated with a time step size of 15 μ s.

are denoted as

$$\max_{i,j} \left\{ \left| \frac{A_{i,j}^n - A_{i,j}^{n-1}}{A_{i,j}^{n-1}} \right| \right\} < \varepsilon, \quad (3.1.2)$$

$$\max_{i,j} \left\{ \left| Q_{i,j}^n - Q_{i,j}^{n-1} \right| \right\} < \varepsilon, \quad (3.1.3)$$

$$\frac{\Delta\varphi}{2} \left| \sum_j Q_{in,j} - \sum_j Q_{out,j} \right| < \varepsilon. \quad (3.1.4)$$

The first two stopping criteria ensure that the simulation has reached numerical convergence. The third criterion ensures that mass is preserved within the artery. In the 2D ROM A has been substituted with R^2 , not $\frac{1}{2}R^2$. Hence, flow rate within a cross-section is computed as $\sum_j \Delta\varphi \frac{1}{2} u_{i,j} R_{i,j}^2 = \frac{\Delta\varphi}{2} \sum_j Q_{i,j}$. The fourth stopping criterion depends on which boundary conditions are applied since the steady-state solution depends on the boundary condition. With the first set of boundary conditions, the fourth stopping criterion becomes

$$\max \left\{ \left| \frac{\Delta\varphi}{2} \sum_j Q_{in,j} \right|, \left| \frac{\Delta\varphi}{2} \sum_j Q_{out,j} \right| \right\} < \varepsilon. \quad (3.1.5)$$

With the second set of boundary conditions, the analytical expression for the steady-state solution (2.2.68) is applied to obtain the fourth stopping criteria

$$\max_i \left\{ \frac{\beta}{5\rho A_0} \left((A_i^n)^{\frac{5}{2}} - (A_{in}^n)^{\frac{5}{2}} \right) - \frac{4}{3} (Q_i^n)^2 (\ln A_i^n - \ln A_{in}^n) + 8 \frac{\mu}{\rho} Q_i^n x_i \right\} < \varepsilon. \quad (3.1.6)$$

Stopping criterion (3.1.6) is only valid if β is constant across the artery. Hence, it can only be applied to steady-state solutions without calcification. Stopping criteria (3.1.3), (3.1.4) and (3.1.5) are computed with an absolute error since flow rate vanishes for the analytical steady-state solution.

Prescribed pressure at inlet

Independent of the choice of n_x , $A(x)$ is constant across the artery (with an inner wall radius of 0.2516 cm) in the numerical steady-state solution if no calcification is present. The numerical steady-state solution is identical to the analytical solution (2.2.63).

Prescribed velocity at inlet

Steady-state solutions without calcification and with a prescribed fixed mean velocity at the inlet are depicted in Figure 3.7. Like the analytical steady-state solution shown in Figure 2.8, the numerical steady-state solution of A is a decreasing function. The steady-state solution of Q should be a constant. However, due to the stopping criteria, the numerical methods have been stopped before Q is constant. Hence, the numerical steady-state solution has an error of $\varepsilon = 10^{-4}$.

These simulation starts with an initial area $A|_{t=0} = A_0$ and an initial flow rate of $Q|_{t=0} = 0 \text{ cm}^3/\text{s}$, while prescribing a pressure of $P_{res} = 9330 \text{ Pa}$ at the outlet (due to the fluid resistance boundary condition). An initial area of A_0 leads to a pressure within the artery lower than the pressure prescribed at the outflow boundary

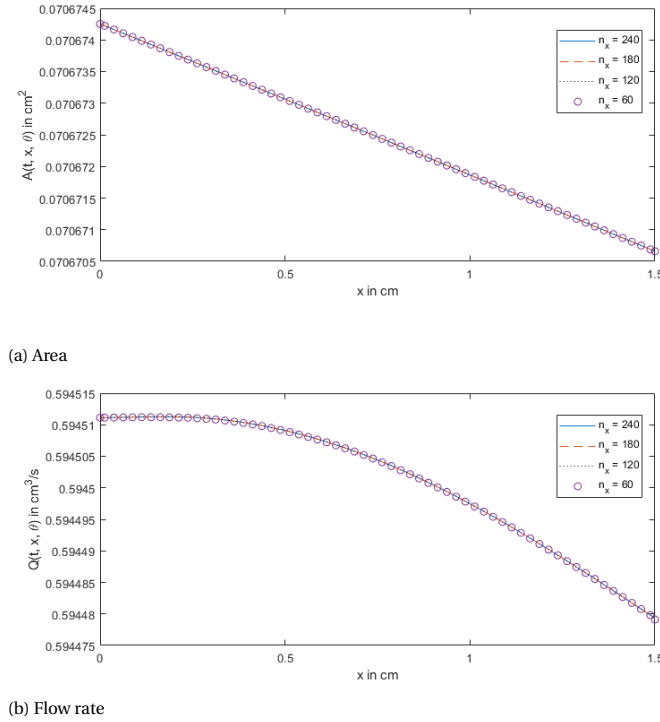


Figure 3.7: Steady-state solution without calcification with a mean velocity of 8.412 cm/s is prescribed at the inlet. n_x is the number of discrete cross-sections .

condition. These simulations start with a left-going wave at the outlet with a positive displacement and a negative flow rate since pressure differences propagate blood flow (see Figure 3.8). The left-going wave with a negative flow rate is irrelevant to the steady-state solution without calcification. However, it influences how the steady-state solution with local calcification is obtained (see Section 3.3).

3.2. Simulations with axisymmetric calcification

The 2D ROM with axisymmetric calcification, axisymmetric inflow, and axisymmetric outflow leads to axisymmetric blood flow, where A and Q are independent of φ . Hence, 2D simulations with these settings are effectively 1D simulations. By incorporating axisymmetry, there is a jump discontinuity in β . The numerical method deals with this discontinuity by smoothing the discontinuity across several cells (see Figure 2.7). However, the 2D ROM does not have a compact form within those smoothing regions, which leads to numerical errors. The error of the numerical steady-state solution can depend on the smoothing length (ξ^x for axisymmetric calcification) and the number of cells within the smoothing length ($\xi^x/\Delta x$ for axisymmetric calcification).

This section focuses on how well the high-resolution method can deal with axisymmetric calcification. The section starts by discussing issues by prescribing a fixed pressure at the inlet, proceeds by investigating how accurately the high-resolution method obtains the steady-state solution of blood flow with axisymmetric calcification, and ends by examining when the numerical method is stable.

3.2.1. Simulations with fixed inlet

The high-resolution methods, which are applied to simulate the x-sweep, should be able to deal with discontinuities in A and Q . However, the 2D numerical method fails to converge with the following specifications:

- $A|_{t=0} = A_0$ and $Q|_{t=0} = 0$ as initial solution.
- $n_x = 60$ and $n_\varphi = 1$.
- $\Delta t = 6.25 \mu\text{s}$.
- A fixed pressure of 10 kPa at the inlet and the non-reflective boundary condition at the outlet.
- $\beta(x, \varphi)$ set as (2.2.60) with $\Delta\xi = 1$ and $\xi^x = 1/4$. ξ^φ does not affect the metric d (2.2.58) in an axisymmetric

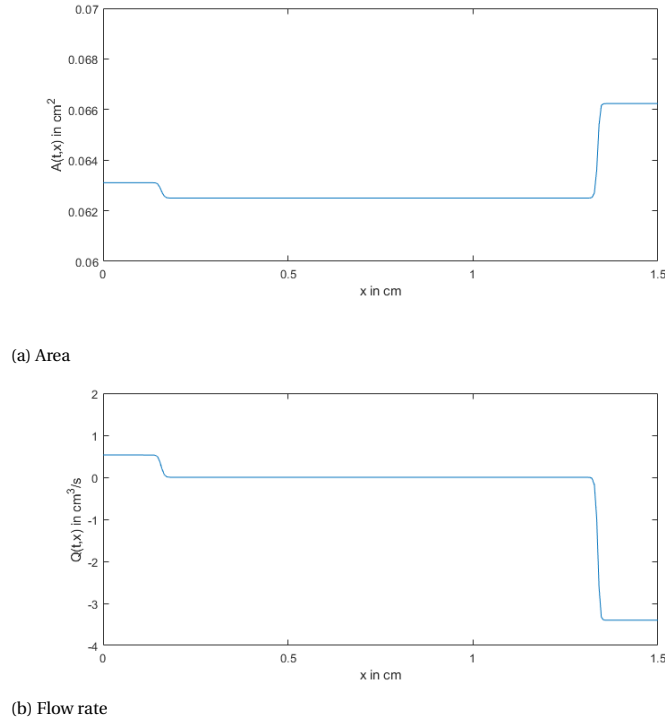


Figure 3.8: Simulation at $t = 176 \mu\text{s}$ with a mean velocity of 8.412 cm/s is prescribed at the inlet.

setting.

Both A and Q oscillate during this simulation due to wave reflections from the inlet and when the right-going wave reaches the calcified area. The amplitude of these oscillations increases and eventually leads to a negative area (see Figure 3.9). Oscillations in the 2D numerical methods are prevented by applying a load curve (2.3.1). The location where A becomes negative lies within the region where the discontinuity in the artery's Young's modulus is smoothing out. Error within the 2D simulations are mainly located in this smoothing region.

The 2D numerical methods is convergent by changing the boundary conditions to a fixed mean velocity (u_{in}) of 8.41199 cm/s and a fluid resistance boundary condition (2.1.1), with $P_{res} = 9330 \text{ Pa}$ and $R_{res} = 1.358 \text{ E9 Pa s / m}^3$. However, steady-state solutions with axisymmetric calcification can be obtained faster by applying a load curve to P_{res} and u_{in} . These steady-state solutions will be studied in the following section.

3.2.2. Steady-state solutions

This section investigates how well the high-resolution method deals with axisymmetric calcification by investigating numerical steady-state solutions. Steady-state solutions are numerically obtained by simulating the time dependent problem until the margin of error is small enough. Steady-state solutions will be obtained for two different sets of boundary conditions. The first set of boundary conditions prescribes pressure at the inlet and applies a non-reflective boundary condition at the outlet. The second set prescribes a mean axial velocity of 8.41199 cm/s at the inlet and incorporates the fluid resistance boundary condition (2.1.1) at the outlet, with $P_{res} = 9330 \text{ Pa}$ and $R_{res} = 1.358 \text{ E9 Pa s / m}^3$. Except for the choice of boundary conditions, steady-state solutions with axisymmetric calcification have been obtained with the following numerical specification:

- $A|_{t=0} = A_0$ and $Q|_{t=0} = 0$ as initial solution.
- $n_x = 30 \cdot r$ for $r \in \{1, 2, 3, 4, 5, 6, 7, 8\}$.
- $n_\varphi = 1$ (since the system is axisymmetric).
- $\Delta t = 6.25 \cdot 60 / n_x \mu\text{s}$ (such that the Courant number is independent of n_x).
- $\beta(x, \varphi)$ set as (2.2.60) with $\Delta\xi = 1$ and ξ^x either $1/4$ or $5\Delta x$.
- The stopping criteria depend on the boundary conditions applied on the 2D ROM. The stopping criteria (3.1.2), (3.1.3) and (3.1.4) are always applied independent of the choice of boundary condition. The stopping

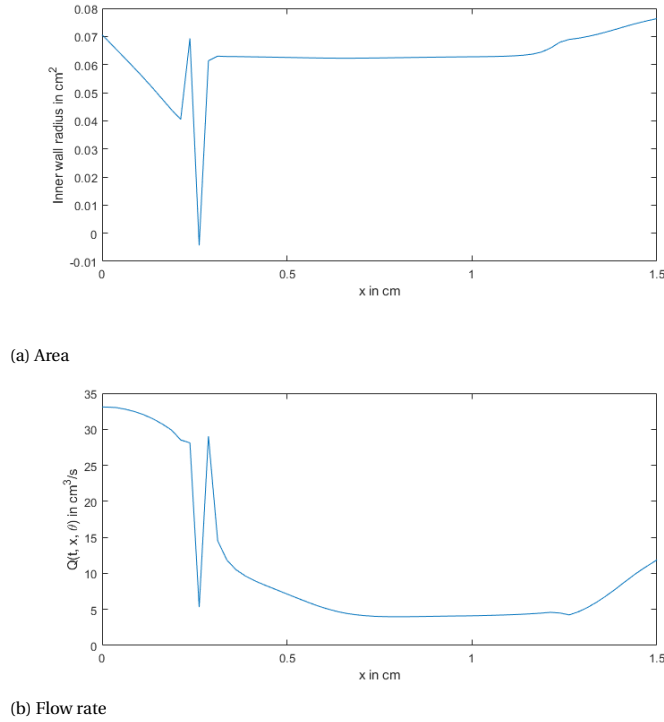


Figure 3.9: Negative area obtained from simulation with axisymmetric calcification and a fixed pressure of 10 kPa at the inlet.

criterion (3.1.5) is added if pressure is prescribed as an inlet boundary condition.

Discontinuous Young's modulus

Simulations with a discontinuous Young's modulus are done by fixing $\Delta\xi$ to 0; in all other cases, $\Delta\xi$ is set to 1. Similar to the simulations without calcification, the numerical method obtains a steady state where A is constant (with $A_i \approx 6.328 \text{ mm}^2$). However, this numerical steady-state solution is incorrect (see Figure 3.10). The analytical solution shows that A should be lower in the calcified region. The numerical method cannot obtain correct solutions if β is discontinuous. $\partial_x \beta = 0$ for the numerical method in the discontinuous case since $\partial_x \beta$ is set to its analytical value at the center of the cells. Consequently, the numerical method cannot deal with the jump discontinuity at cell interfaces. We advise the reader to study the papers of Toro and Siviglia [26] and Pimentel-García et al. [17] for numerical methods for blood flow that deal with discontinuous mechanical properties of arteries.

Continuous Young's modulus and prescribing pressure at the inlet

The numerical steady-state solutions with $\xi^x = \frac{1}{4}$ and a pressure boundary condition of 1 kPa are depicted in Figure 3.11. For $n_x = 30 \cdot r$, the number of cells that fit into the smoothening region of 0.25 cm is precisely 5r cells. The choice of n_x does not significantly affect A within the numerical steady-state solution (see Figure (3.11a)). Q is constant for the analytical steady-state solution. However, Q is not constant for the numerical steady-state solution (see Figure 3.11b). The numerical steady-state solution shows visible bumps and dents where the artery's elasticity is not constant. Errors within the numerical solutions in the smoothening region can be expected since the 2D ROM has no compact form in those regions. The size of these humps and dents decreases as Δx decreases.

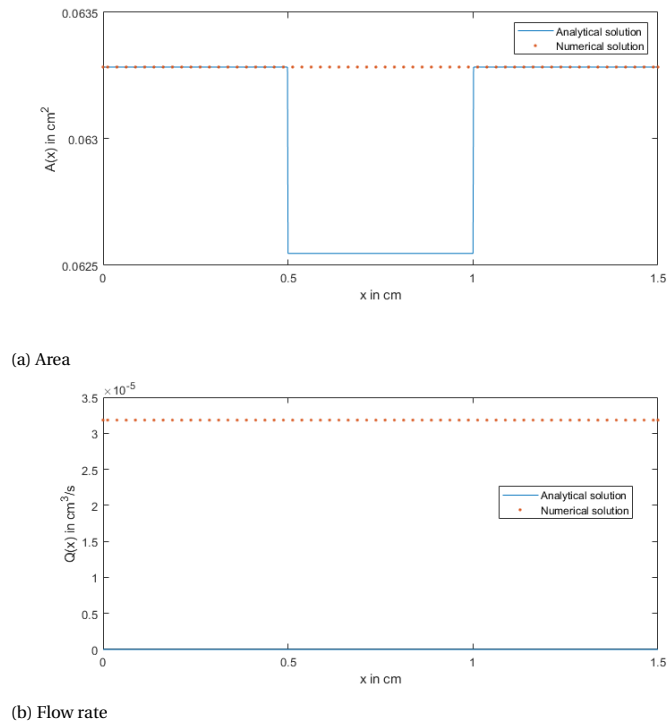


Figure 3.10: Analytical and numerical steady-state solutions with discontinuous E and 1 kPa pressure as inlet boundary condition.

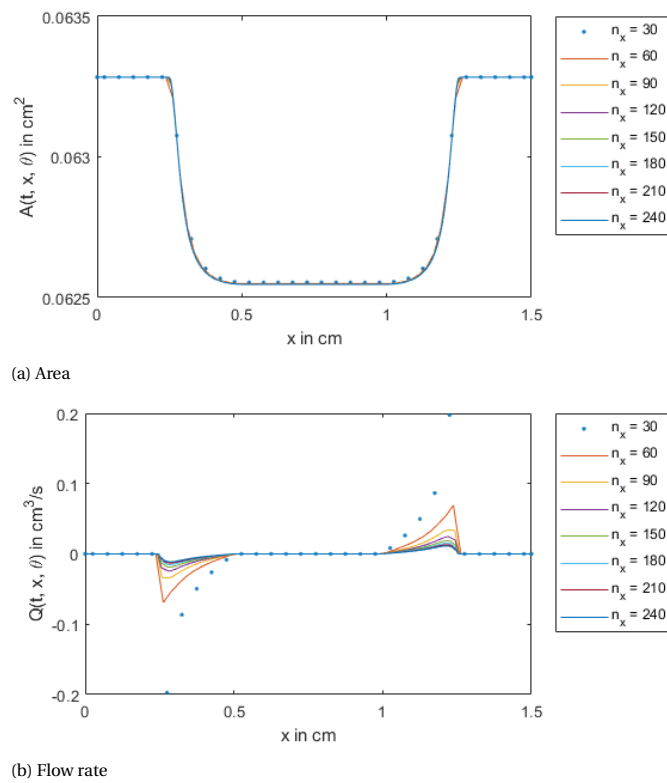


Figure 3.11: Steady-state solutions with axisymmetric calcification, $\xi^x = \frac{1}{4}$ and 1 kPa pressure applied at the inlet. n_x is the number of discrete cross-sections.

For the numerical analysis, error will be computed as

$$\varepsilon_Q = \max_{i,j} Q - \min_{i,j} Q, \quad (3.2.1)$$

$$\varepsilon_2 = \frac{\|A - A_{Steady}\|_2}{\|A_{Steady}\|_2}, \text{ and} \quad (3.2.2)$$

$$\varepsilon_\infty = \frac{\|A - A_{Steady}\|_\infty}{\|A_{Steady}\|_\infty}, \quad (3.2.3)$$

where A_{Steady} the analytical steady-state solution (2.2.63) corresponding to $Q = 0$. These numerical errors are depicted in Figure 3.12 and Table 3.1. The least squares method yields that $\varepsilon_2 = \mathcal{O}(\Delta x^{1.500})$, $\varepsilon_\infty = \mathcal{O}(\Delta x^{0.9386})$, and $\varepsilon_Q = \mathcal{O}(\Delta x^{1.374})$. Figure (3.12) indicates that ε_2 , ε_∞ and ε_Q are well approximated. Regression analysis shows that the approximation of ε_2 , ε_∞ , and ε_Q have a correlation coefficient of 0.9990, 0.9840, and 0.9961, respectively. All errors are well approximated since these correlation coefficients are close to 1.

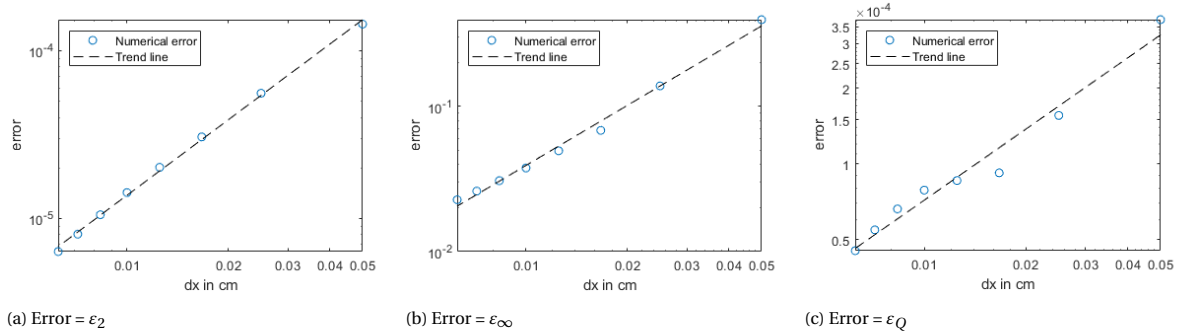


Figure 3.12: Numerical error in log scale from simulations with a fixed smooth transition length and prescribed pressure at the inlet.

Table 3.1: Numerical error with a fixed smooth transition length and applying pressure at the inlet.

n_x	ε_2	ε_∞	ε_Q
30	143.9 E-6	37.37 E-5	39.48 E-2
60	55.75 E-6	15.57 E-5	13.82 E-2
90	30.62 E-6	9.207 E-5	6.827 E-2
120	20.17 E-6	8.586 E-5	4.938 E-2
150	14.62 E-6	7.866 E-5	3.760 E-2
180	10.53 E-6	6.624 E-5	3.076 E-2
210	8.064 E-6	5.470 E-5	2.607 E-2
240	6.352 E-6	4.522 E-5	2.273 E-2

Table 3.1 and Figure 3.12c show that the approximated error is not a very good fit even though ε_Q is approximated with a correlation coefficient of 0.9961. ε_Q roughly decreases three-fold by doubling n_x from 30 to 60, whereas ε_Q roughly decreases two-fold by doubling n_x from 120 to 240. Hence, approximated error ε_Q cannot be extrapolated for large values of n_x . Table 3.1 might indicate that $\varepsilon_Q = \mathcal{O}(\Delta x)$ for small values for Δx . However, additional simulations are needed to confirm this.

Steady-state solutions will be investigated by setting $\xi^x = 5\Delta x$ and increasing the pressure at the inlet to 10 kPa. For $n_x = 30$, the smoothing region has a size of $\xi^x = 5\Delta x = \frac{1}{4}$ cm, identical to the smoothing region corresponding to the steady-state solutions depicted in Figure (3.11). The steady-state solutions are depicted in Figure (3.13) and their numerical errors are depicted in Table 3.2.

The steady-state solutions clearly show that area and flow rate are constant outside of the smoothing area, while they are not constant inside of the smoothing area. Table 3.2 shows that ε_Q and ε_∞ are independent of Δx , indicating that ε_Q and ε_∞ depend on the number of cells in the smoothing area. ε_2 still decreases as Δx decreases, but clearly less the error with fixed ξ^x . Regression analysis shows that ε_2 has a numerical error of $\mathcal{O}(\Delta x^{0.3011})$ with a correlation coefficient of 0.9924.

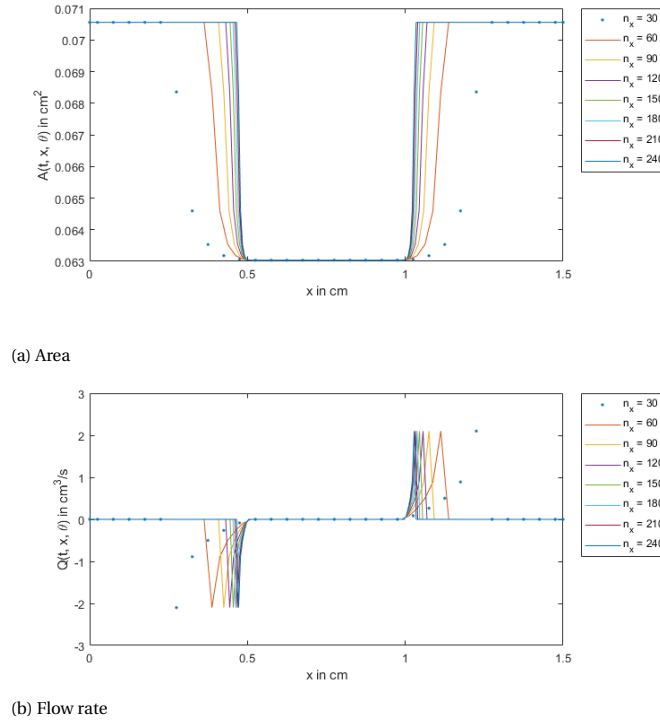


Figure 3.13: Steady-state solutions with axisymmetric calcification, $\xi^x = 5\Delta x$ and 10 kPa pressure applied at the inlet. n_x is the number of discrete cross-sections.

Table 3.2: Numerical error with $\xi^x = 5\Delta x$ and applying pressure at the inlet.

n_x	ε_2	ε_∞	ε_Q
30	13.29 E-4	3.325 E-3	4.199
60	10.18 E-4	3.324 E-3	4.199
90	8.925 E-4	3.324 E-3	4.199
120	8.230 E-4	3.324 E-3	4.199
150	7.786 E-4	3.324 E-3	4.199
180	7.475 E-4	3.324 E-3	4.199
210	7.246 E-4	3.324 E-3	4.199
240	7.069 E-4	3.324 E-3	4.199

Decrease error in flow rate

All steady-state solutions in the preceding section are applied with the non-reflective boundary condition. The analytical steady-state solution with the non-reflective boundary condition should have a flow rate of 0 cm^3/s . However, Q is non-zero within the smoothing region for the numerical steady-state solutions (see Figure (3.11b) and Figure (3.13b)). One possibility to decrease ε_Q is to change the smooth transition function β_T (2.2.59). $\beta_T(\xi)$ becomes an odd function after applying the transformation

$$\xi \mapsto \beta_T\left(\xi - \frac{1}{2}\Delta\xi\right) - \beta_T\left(\frac{1}{2}\Delta\xi\right) = \frac{\beta_H - \beta_C}{2} \sin\left(\frac{\pi\xi}{\Delta\xi}\right),$$

where β_H and β_C contain mechanical properties of a healthy artery and calcification. However, Figure (3.11b) and Figure (3.13b) shows that the error in Q is larger near the healthy region of the artery than the calcified region of the artery. Changing the smooth transition function β_T such that the change within $\beta_T(\xi)$ is more significant near the calcified region ($\xi = 0$) than the healthy region ($\xi = \Delta\xi$) could lower the error in ε_Q .

Continuous Young's modulus and prescribing velocity at the inlet

In this section we will study the steady-state solution by smoothing out the discontinuity in the artery's Young's modulus across several cells, by prescribing a mean axial velocity of 8.41199 cm/s at the inlet, and

by applying the fluid resistance boundary condition (2.1.1) at the outlet, with $P_{res} = 9330$ Pa and $R_{res} = 1.358$ E9 Pa s / m³. The analytical steady station solution for this problem is not known. However, mass is conserved if Q is constant across the artery. Hence, this section will only focus on the numerical error ε_Q (3.2.1). The numerical steady-state solutions with $\xi^x = \frac{1}{4}$ are shown in Figure 3.14, and with $\xi^x = 5\Delta x$ are shown in Figure 3.15, whereas Table 3.3 depicts the error ε_Q .

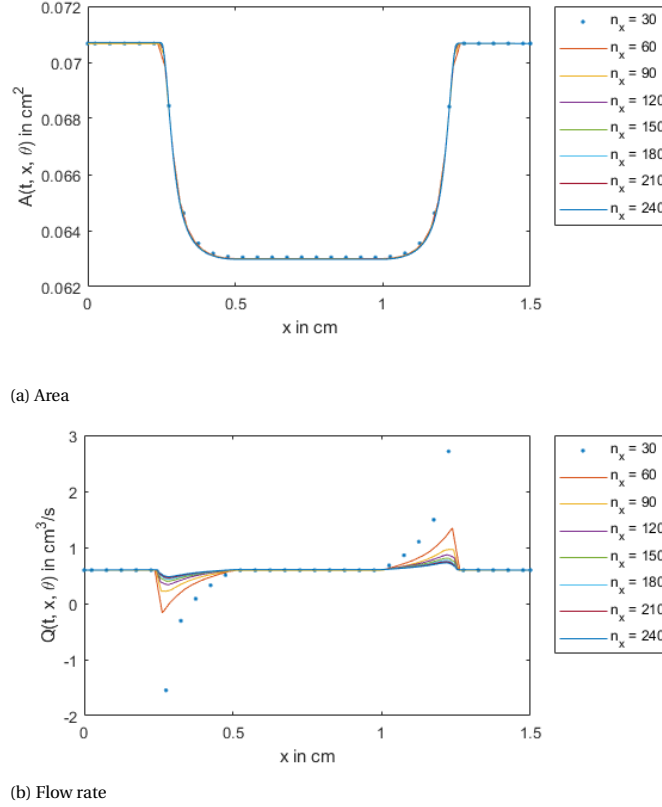


Figure 3.14: Steady-state solutions with axisymmetric calcification, $\xi^x = \frac{1}{4}$ and 8.412 cm/s mean velocity applied at the inlet. n_x is the number of discrete cross-sections.

The numerical steady-state solution has many similar properties to the steady-state solution that prescribes pressure at the inlet. Area and flow rate are (nearly) constant where $\partial_x \beta = 0$, and there are clear humps and dents in flow rate where $\partial_x \beta \neq 0$. For $\xi^x = 1/4$, A is independent of the choice of n_x . ε_Q clearly decreases for $\xi^x = 1/4$, while it remains relatively constant for $\xi^x = 5\Delta x$. The only clear difference between these steady-state solutions and those obtained by pressure prescribed at the inlet is that blood flows for this numerical steady-state solution. The least squares method for $\xi^x = 1/4$ even approximates the error ε_Q similar with $\varepsilon_Q = \mathcal{O}(\Delta x^{1.374})$. Table 3.3 also indicates that the approximated error ε_Q is not a good fit. ε_Q for $\xi^x = 1/4$ roughly decreases three-fold by doubling n_x from 30 to 60, whereas ε_Q roughly decreases two-fold by doubling n_x from 120 to 240. Hence, approximated error ε_Q cannot be extrapolated for large values of n_x .

3.2.3. Numerical stability

Lastly, we will investigate how the Courant number influences the stability of the high-resolution method by simulating blood flow with axisymmetric calcification. Numerical stability is studied by prescribing a mean axial velocity u_{in} of 8.41199 cm/s at the inlet and by applying the fluid resistance boundary condition (2.1.1) at the outlet, with $P_{res} = 9330$ Pa and $R_{res} = 1.358$ E9 Pa s / m³. u_{in} and P_{res} are multiplied with the load curve $l(t; 0, t_{end}, 0, 1)$ (2.3.1), with $t_{end} = 8$ ms, to prevent oscillations. The simulations are done with the following numerical specifications:

- $A|_{t=0} = A_0$ and $Q|_{t=0} = 0$ as initial solution.
- $n_x = 60$ ($\Delta x = 0.25$ mm).
- $n_\varphi = 1$.

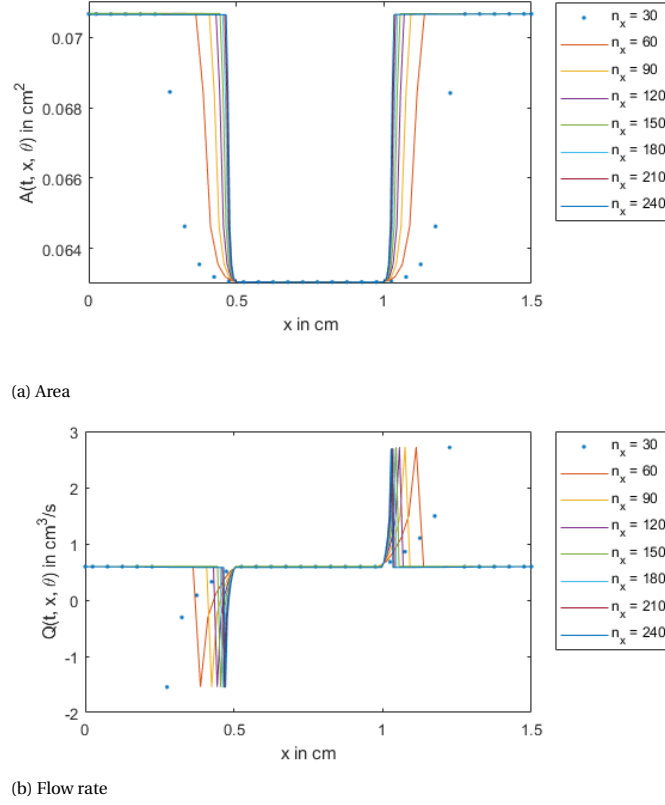


Figure 3.15: Steady-state solutions with axisymmetric calcification, $\xi^x = 5\Delta x$ and 8.412 cm/s mean velocity applied at the inlet. n_x is the number of discrete cross-sections.

- $1 \mu\text{s} \leq \Delta t \leq 10 \mu\text{s}$, with a step-size of $0.1 \mu\text{s}$.
- $\beta(x, \varphi)$ set as (2.2.60), with $\Delta\xi = 1$ and $\xi^x = \frac{1}{4}$. ξ^φ does not affect the metric d for axisymmetric calcification.
- Simulated until the stopping criteria (3.1.2), (3.1.3) and (3.1.4) are satisfied with $\varepsilon = 10^{-3}$, or $t > 0.5$ s.

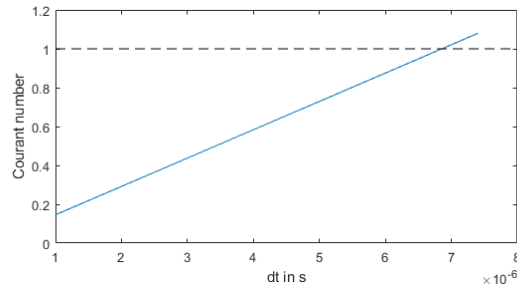


Figure 3.16: Maximum observed Courant number with axisymmetric calcification.

Figure 3.16 shows that the maximum observed Courant number depends linearly on the time step size. The high-resolution method converges numerically if $\Delta t \leq 7.3 \mu\text{s}$, and is unstable for $\Delta t \geq 7.4 \mu\text{s}$. Courant numbers larger than 1 are observed with $\Delta t \geq 6.9 \mu\text{s}$. The numerical method can still converge despite having Courant numbers slightly larger than 1. This happens because the Courant number is much higher in the calcified area, which is located in the middle of the artery. Once they leave the calcified area, the oscillating waves are damped, stabilizing the numerical method for Courant numbers slightly larger than 1.

Table 3.3: Numerical error from steady-state simulation by prescribing the velocity at the inlet.

n_x	$\varepsilon_Q (\xi^x = 1/4)$	$\varepsilon_Q (\xi^x = 5\Delta x)$
30	4.259	4.259
60	1.515	4.266
90	0.7457	4.265
120	0.5362	4.264
150	0.4092	4.264
180	0.3330	4.250
210	0.2835	4.250
240	0.2464	4.251

3.3. Simulations with local calcification

Simulations with local calcification are asymmetrical. The continuity condition applied to the 2D ROM (2.2.35) will affect blood flow with local calcification. This equation was superfluous for blood flow without calcification and blood flow with axisymmetrical calcification since blood flow was axisymmetric. Several issues can occur with the continuity condition by simulating blood flow with local calcification. This section addresses the issues surrounding the continuity conditions and proceeds with investigating steady-state solutions with local calcification.

3.3.1. Issues with continuity condition

The continuity condition $\partial_\varphi v_x|_{r=0} = 0$ is satisfied if axial velocity within the artery's origin does not depend on φ . However, while simulating the 2D ROM with local calcification, it is possible that the continuity condition cannot be satisfied. Recall that the 2D ROM only includes the family of velocity profiles $s(y, \gamma) = \frac{\gamma+2}{\gamma}(1-y^\gamma)$, where $y \in [0, 1]$ is the rescaled radius and $\gamma(t, x, \varphi)$ is a strictly positive function that influences the shape of the velocity profile. By reducing axial velocity with these velocity profiles, the continuity condition is identical to

$$v_x|_{r=0} = u \frac{\gamma+2}{\gamma}, \quad (3.3.1)$$

where $v_x|_{r=0}$ is independent of φ and $u(t, x, \varphi)$ is the mean axial velocity. The continuity condition (3.3.1) cannot be satisfied if $|u|$ is larger than $|v_x|_{r=0}|$ or if sign of u is different than the sign of $v_x|_{r=0}$.

Example 1: pressure prescribed at the inlet and non-reflective boundary condition at the outlet

Simulating the 2D ROM with local calcification, $A|_{t=0} = A_0$, $Q|_{t=0} = 0$, $\gamma|_{t=0} = \gamma|_{x=0} = 2$, $P|_{x=0} = P_{in} > 0$, and non-reflective boundary condition at the outlet will be unable to satisfy the continuity condition after a certain amount of time. Simulations under these conditions start with a right-going wave at the inlet, while there is no left-going wave at the outlet (see Figure 3.6). The speed of the right-going wave is identical to the corresponding eigenvalue, which is larger within the calcified region than in the healthy region. This leads to a cross-section with non-zero axial velocity within the calcified region and zero axial velocity within the healthy region. The continuity condition (3.3.1) cannot be satisfied within this cross-section. Velocity profiles that have their maximum not located within the origin need to be included in the 2D ROM to simulate this problem.

This problem can be alleviated by starting the simulation with a strictly positive volumetric flow rate and applying a load curve (2.3.1) to P_{in} . However, the steady-state solution cannot be obtained by incorporating these fixes. Similar to simulations with axisymmetric calcification (see Figure 3.11b), simulations with local calcification will also have humps and dents within the smoothing region. Q vanishes for the analytical steady-state solution with a non-reflective boundary condition at the outlet (2.2.63). As the numerical method approaches the steady-state solution, axial velocity within the dents becomes negative, resulting in cross-sections with positive and negative axial velocity. The continuity condition (3.3.1) cannot be satisfied for these cross-sections. Velocity profiles that allow backflow need to be included in the 2D ROM to obtain this steady-state solution numerically.

Example 2: velocity prescribed at the inlet and fluid-resistance boundary condition at the outlet

Simulating the 2D ROM with local calcification, $A|_{t=0} = A_0$, $Q|_{t=0} = 0$, $\gamma|_{t=0} = \gamma|_{x=0} = 2$, $u|_{x=0} = u_{in} = 8.41199$ cm/s, and the fluid-resistance boundary condition (2.1.1), with $P_{res} = 9330$ Pa and $R_{res} = 1.358 \text{ E9 Pa s / m}^3$, fails to satisfy the continuity condition (3.3.1) after a certain amount of time. This simulation starts with a right-going wave with a strictly positive axial velocity at the inlet and a left-going wave with a strictly negative axial velocity at the outlet (see Figure 3.8b). The location where these waves hit depends on the eigenvalues within the system since the speed of each wave depends on their corresponding eigenvalue. These waves meet each other earlier within the calcified region than within the healthy region since eigenvalues within the calcified region have larger magnitudes than within the healthy region. This leads to cross sections with positive and negative axial velocities, which cannot be satisfied with the velocity profiles included in the 2D ROM.

This problem can be alleviated by prescribing a load curve to u_{in} and P_{res} , and by starting with a strictly positive volumetric flow rate to keep Q strictly positive at all times. The arduous task of finding a suitable load curve and initial flow rate depends on the parameters of the fluid-resistance boundary conditions, which is why we use a different strategy to obtain a steady-state solution with local calcification.

3.3.2. Steady-state solutions

Steady-state solutions for the 2D ROM are only obtained by prescribing a mean axial velocity at the inlet and a fluid-resistance boundary condition at the outlet. Steady-state solutions for local calcification are numerically obtained by taking the steady-state solution without calcification as an initial value and slowly adding calcification. Calcification is added to the system by applying a load curve to β as

$$\beta(t, x, \varphi) = l(t; 0, t_{end}, \beta_{WC}(x, \varphi), \beta_{LC}(x, \varphi)), \quad (3.3.2)$$

where $t_{end} = 80$ ms, β_{WC} and β_{LC} specify the mechanical properties without calcification and with local calcification, respectively, and

$$l(t; t_{start}, t_{end}, y_{start}, y_{end}) = \begin{cases} y_{start} & \text{for } t < 0, \\ \frac{y_{end} + y_{start}}{2} - \frac{y_{end} - y_{start}}{2} \cos\left(\pi \frac{t - t_{start}}{t_{end} - t_{start}}\right) & \text{for } t_{start} < t < t_{end}, \\ y_{end} & \text{for } t > t_{end}. \end{cases} \quad (2.3.1)$$

Remark that β depends on time does not affect the 2D ROM denoted in (2.2.36) and (2.2.37) and $\partial_t \beta = 0$ for $t > t_{end}$.

With this approach, the steady-state solution can be obtained numerically, given that the velocity profiles incorporated in the 2D ROM can replicate the analytical steady-state solution. The numerical steady-state solution without calcification has a strictly positive flow rate (see 3.7b). The numerical steady-state solution with axisymmetric calcification has a negative flow rate if $\xi^x / \Delta x$ (the number of cells within the smoothing region) is less than or equal to 10 (see 3.14b). The numerical method fails to obtain a steady-state solution with local calcification if $\xi^x / \Delta x \leq 10$. It fails because cross-sections within the numerical steady-state solution have positive and negative axial velocity; thus, the continuity condition (3.3.1) cannot be satisfied.

In this section will only focus on obtaining steady-state solutions with the following specifications:

- Mean axial velocity of 8.41199 cm/s prescribed at the inlet.
- $P_{res} = 9330$ Pa and $R_{res} = 1.358 \text{ E9 Pa s / m}^3$ (see fluid-resistance boundary condition (2.1.1)).
- $n_x = 120$ and $n_\varphi \in \{12, 24, 36, 48, 60, 72, 84, 96\}$.
- β_{LC} set as (2.2.60), with $\xi^x = \frac{1}{4}$ and ξ^φ either $\frac{1}{2}\pi$ or $3\Delta\varphi$. Remark that for $n_\varphi = 12$, $3\Delta\varphi = 3 \cdot 2\pi/12 = \frac{1}{2}\pi$.

- The simulation stops once the following stopping criteria are satisfied with $\varepsilon = 10^{-4}$:

$$\max_{i,j} \left\{ \frac{|A_{i,j}^n - A_{i,j}^{n-1}|}{|A_{i,j}^{n-1}|} \right\} < \varepsilon, \quad (3.1.2)$$

$$\max_{i,j} \left\{ \frac{|Q_{in,j}^n - Q_{in,j}^{n-1}|}{|Q_{in,j}^{n-1}|} \right\} < \varepsilon, \quad (3.3.3)$$

$$\max_{i,j} \left\{ \frac{|Q_{out,j}^n - Q_{out,j}^{n-1}|}{|Q_{out,j}^{n-1}|} \right\} < \varepsilon, \quad (3.3.4)$$

$$\frac{\Delta\varphi}{2} \left| \sum_j Q_{in,j} - \sum_j Q_{out,j} \right| < \varepsilon. \quad (3.1.4)$$

The stopping criteria (3.1.2) and (3.1.4) have also been applied to obtain steady-state solutions without calcification and with axisymmetric calcification. The stopping criteria (3.3.3) and (3.3.4) have replaced the stopping criterion (3.1.3). Criterion (3.1.3) is not satisfied within the smoothening region for some simulations, so we currently only satisfy its relative counterpart at the inlet and the outlet.

Table 3.4 shows how the error ε_Q (3.2.1) depends on ξ^φ and n_φ . This table indicates that $\xi^\varphi/\Delta\varphi$ should be as small as possible to minimize ε_Q . By fixing ξ^φ to $\pi/2$, ε_Q obtains its minimum if $n_\varphi = 12$, while it increases and decreases as n_φ increases. For $\xi^\varphi = 3\Delta\varphi$, ε_Q oscillates between 0.5349 and 0.5448. For n_φ divisible by 24, the calcification area $I_C = [0.5, 1] \times [\frac{3}{4}\pi, \frac{5}{4}\pi]$ is well meshed, i.e. the boundary of the calcified region is located at cell interfaces. While for $n_\varphi \bmod 24 = 12$, the boundary of the calcified region goes through the center of some cells. As a consequence, β within the smoothening region is significantly different between n_φ divisible by 24 and $n_\varphi \bmod 24 = 12$, which explains the oscillatory behavior for $\xi^\varphi = 3\Delta\varphi$. ε_Q with $\xi^\varphi = 3\Delta\varphi$ is slightly smaller for $n_\varphi \bmod 24 = 12$.

Table 3.4: Numerical error from steady-state simulation with local calcification. n_φ is the number of cells within a cross-section, $\Delta\varphi = 2\pi/n_\varphi$ is the height of a cell, and ξ^φ is a parameter that influences the smoothening region (see Figure 2.7).

n_φ	$\varepsilon_Q (\xi^\varphi = \pi/2)$	$\varepsilon_Q (\xi^\varphi = 3\Delta\varphi)$
12	0.5349	0.5349
24	0.6933	0.5447
36	0.8052	0.5349
48	0.6657	0.5448
60	0.6230	0.5350
72	0.6928	0.5448
84	0.7423	0.5350
96	0.7775	0.5448

Surprisingly, for $\xi^\varphi = \pi/2$ ε_Q does not decrease as $\Delta\varphi$ decreases. It can very well be that ε_Q depends significantly more on $\xi^x/\Delta x$ than $\xi^\varphi/\Delta\varphi$. However, Table 3.4 only gives minor information about the numerical steady-state solutions. The analytical steady-state solutions are not even known for these simulations. Steady-state solutions for $\xi^\varphi = \pi/2$, for $(\xi^\varphi, n_\varphi) = (3\Delta\varphi, 84)$, for $(\xi^\varphi, n_\varphi) = (\pi/2, 96)$, and for $(\xi^\varphi, n_\varphi) = (3\Delta\varphi, 96)$ are depicted in Figure 3.17, Figure 3.18, Figure 3.19, and Figure 3.20 as heatmaps to study the numerical steady-state solutions more appropriately.

Figure 3.17 shows the inner wall radius within the numerical steady-state solutions. The inner wall radius is (nearly) constant within the healthy and calcified regions. Its maximum is located in the healthy region, and its minimum is in the calcified region. The inner wall radius increases in the smoothening region as the distance d (2.2.58) increases.

Figure 3.18 shows the volumetric flow rate within the numerical steady-state solutions. Q is nearly constant where $\partial_x\beta = 0$, i.e., in the healthy region, the smoothening region where $x \in (0.5, 1)$, and the calcified region. At the same time, it has a dent in the smoothening region for $x < 0.5$ and a hump in the smoothening region

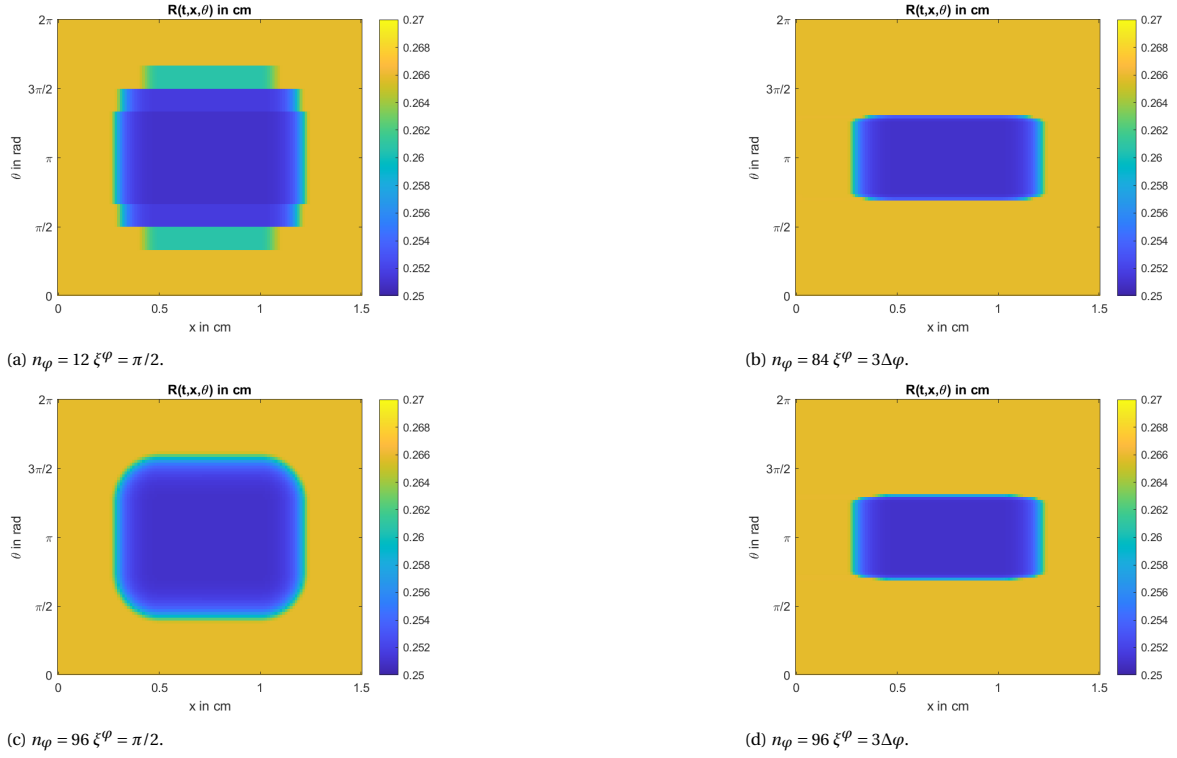


Figure 3.17: Inner wall radius within steady-state solutions with local calcification. n_φ is the number of cells within a cross-section, $\Delta\varphi = 2\pi/n_\varphi$ is the height of a cell, and ξ^φ is a parameter that influences the smoothening region (see Figure 2.7).

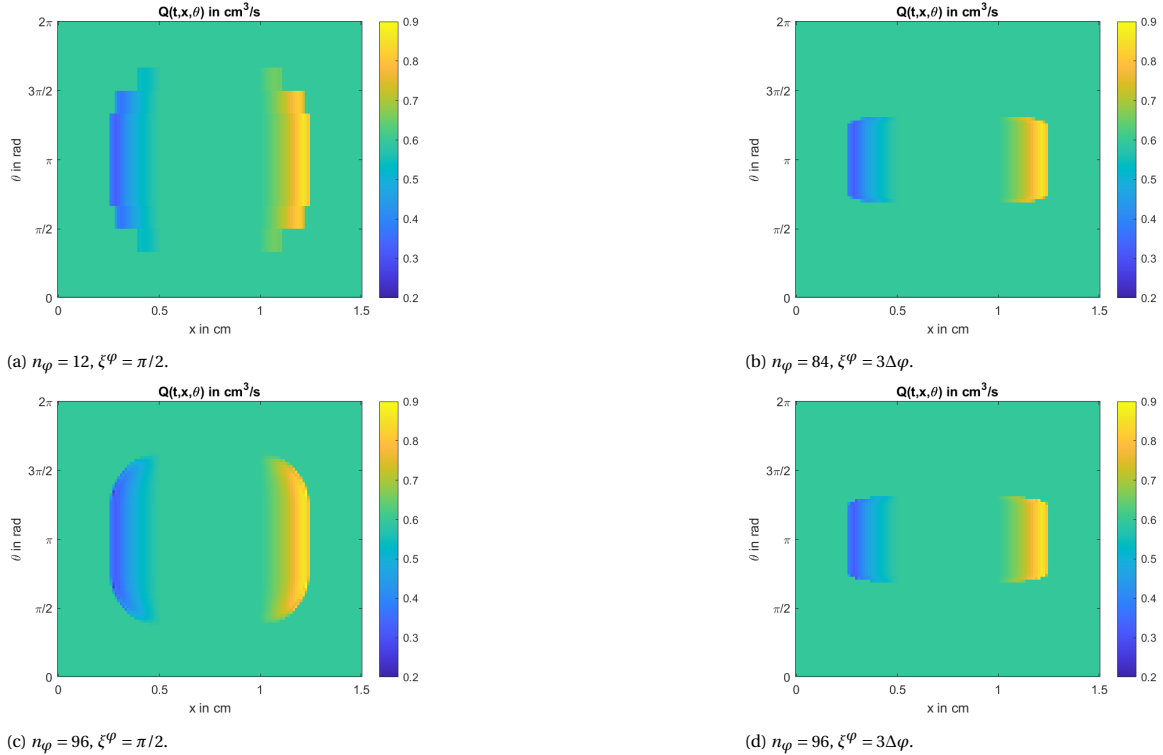


Figure 3.18: Volumetric flow rate within steady-state solutions with local calcification. n_φ is the number of cells within a cross-section, $\Delta\varphi = 2\pi/n_\varphi$ is the height of a cell, and ξ^φ is a parameter that influences the smoothening region (see Figure 2.7).

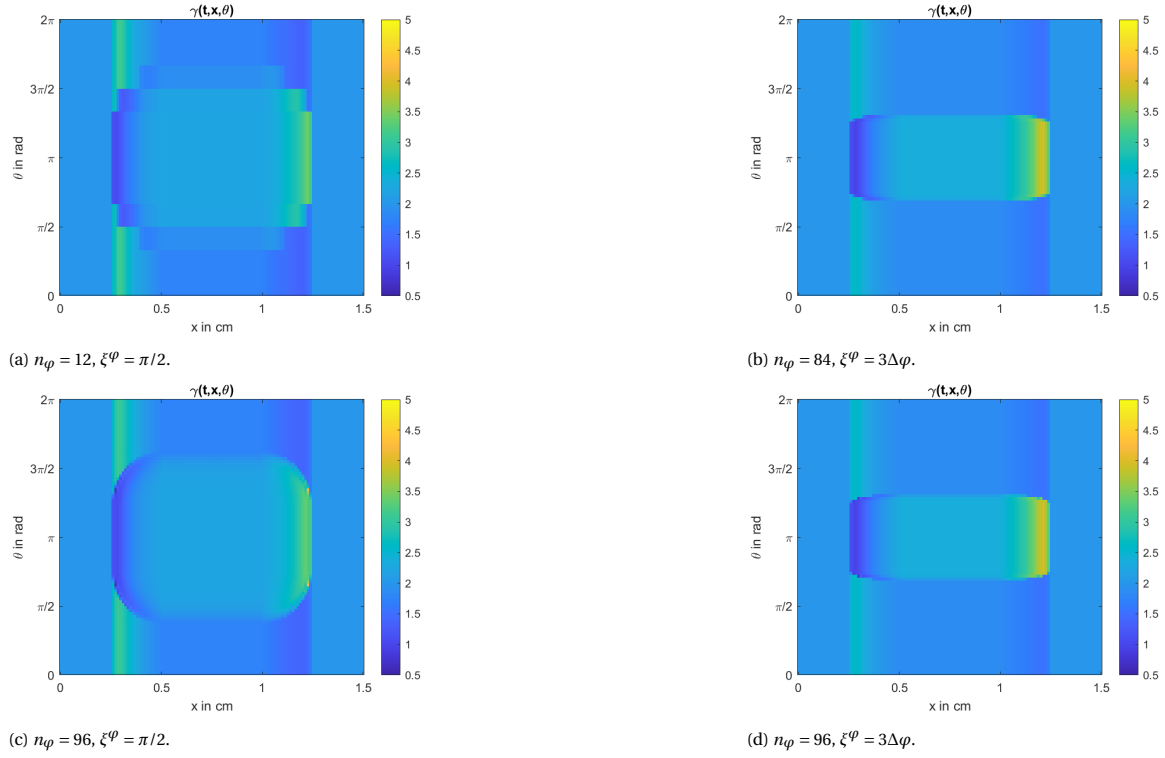


Figure 3.19: γ within steady-state solutions with local calcification. n_ϕ is the number of cells within a cross-section, $\Delta\phi = 2\pi/n_\phi$ is the height of a cell, and ξ^ϕ is a parameter that influences the smoothing region (see Figure 2.7).

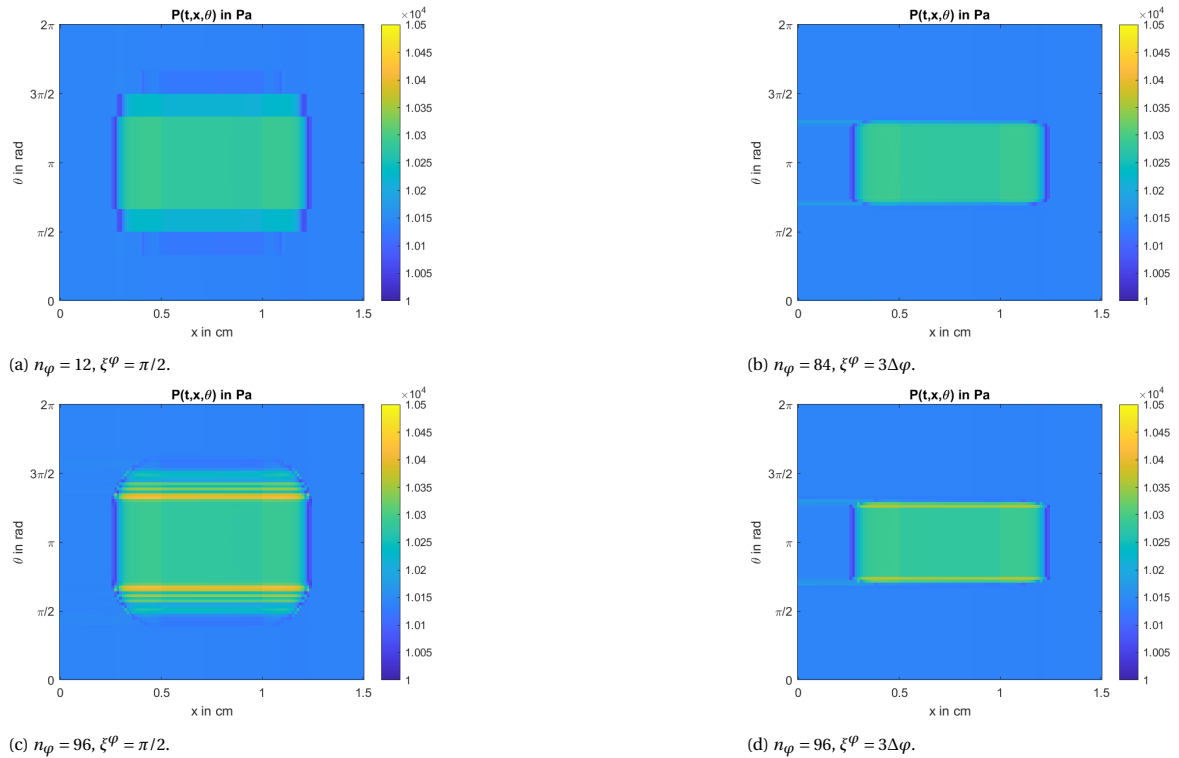


Figure 3.20: Pressure within steady-state solutions with local calcification. n_ϕ is the number of cells within a cross-section, $\Delta\phi = 2\pi/n_\phi$ is the height of a cell, and ξ^ϕ is a parameter that influences the smoothing region (see Figure 2.7).

for $x > 1$. Information obtained from simulations without calcification and with calcification can be extended to explain this. For $\varphi < \frac{3}{4}\pi - \xi^\varphi$ and $\varphi > \frac{5}{4}\pi + \xi^\varphi$, $\partial_x \beta = 0$ and thus flow rate without calcification shows that Q is nearly constant for the numerical steady-state solutions without calcification (Figure (3.7b)). The solutions behave similarly to the solution with axisymmetric calcification for $\varphi \in (\frac{3}{4}\pi - \xi^\varphi, \frac{5}{4}\pi + \xi^\varphi)$. That is, Q is constant where $\partial_x \beta = 0$, while has dents where $\partial_x \beta > 0$ and humps where $\partial_x \beta < 0$.

Figure 3.19 displays γ within the numerical steady-state solutions. Since R and Q are known, γ is computed with R and Q by equations (2.2.55) and (2.2.56), where $\gamma_{avg} = 2$. γ is (nearly) constant in cross sections without calcification, i.e., $x < 0.5 - \xi^x$ and $x > 1 + \xi^x$, since R and Q are constant within those cross sections. For $0.5 < x < 1$, γ is only dependent R since Q is nearly constant. γ attains its largest value where R is large (healthy region), whereas it attains its smallest value where R is small (calcified region). For $0.5 - \xi^x < x < 0.5$ and $1 < x < 1 + \xi^x$ γ is heavily affected by the humps and dents in Q . For $0.5 - \xi^x < x < 0.5$, Q has a dent within the smoothing region, which leads to lower values of γ within the smoothing region and higher values of γ in the healthy region. For $1 < x < 1 + \xi^x$, Q has a hump within the smoothing region, which leads to higher values of γ within the smoothing region and lower values of γ in the healthy region.

Figure 3.20 displays pressure within the numerical steady-state solutions computed by (2.2.1), with $P_0 = 0$ Pa and $R_0 = 0.25$ cm. Pressure seems nearly constant inside the calcified and healthy area, with a higher value inside the calcified area than inside the healthy area. Pressure within the smoothing region is dubious. For $\varphi \in (\frac{3}{4}\pi - \xi^\varphi, \frac{5}{4}\pi + \xi^\varphi)$, β is independent on φ , and the artery has a pressure drop in the smoothing region adjacent to the healthy region. These pressure drops are most likely linked to the humps and dents in flow rate since blood flow is propagated through pressure differences.

Figure 3.20d shows that pressure undergoes oscillation within the smoothing regions despite the inner wall radius and β being smooth. This oscillatory behavior could be linked to how the 2D numerical method performs the φ -sweep. The φ -sweep solves the problem analytically (see (2.2.43)), however the analytical solution still depend on $\partial_\varphi A$ and $\partial_\varphi \gamma$. Within finite volume methods, it is advised to incorporate fluxes to deal with first-order derivatives [12]. However, the analytical solution is used since the φ -sweep yields a triple-zero eigenvalue. It is more likely that β within the smoothing region should be computed differently to prevent these oscillations.

From the simulations performed, the simulation with $n_\varphi = 84$ and $\xi^\varphi = 3\Delta\varphi$ should be used to emulate blood flow with local calcification. The smoothing region is relatively small, while oscillations do not occur. However, simulations with $\xi^x = 3\Delta x$ for $n_\varphi = 84$ and $n_\varphi = 96$ include an artifact in pressure. There is a clear spike in pressure in certain regions within the healthy area (see Figure 3.20d and Figure 3.21).

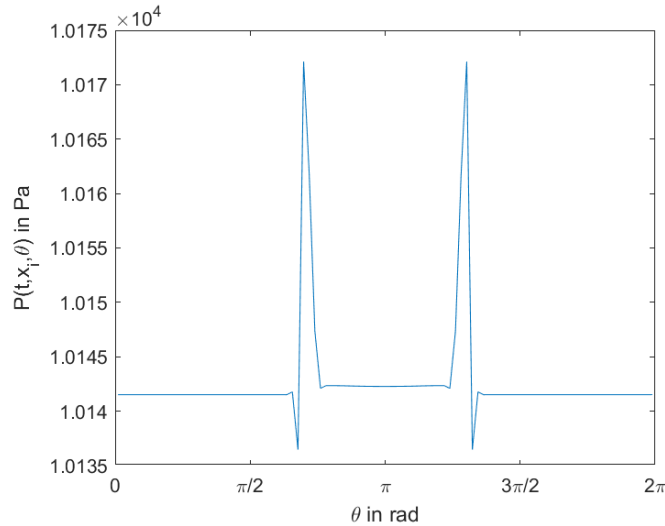


Figure 3.21: Pressure adjacent to the inlet for steady-state solutions with local calcification, $n_\varphi = 96$ and $\xi^\varphi = 3\Delta\varphi$.

3.4. Simulations with pulsatile flow

In the previous section, we only looked into simulations where velocity or pressure is fixed (after a certain amount of time) at the inlet. This section will study and compare 2D- and 3D simulations for a pulsatile flow. The parabolic mean axial velocity prescribed at the inlet is shown in Figure 3.22.

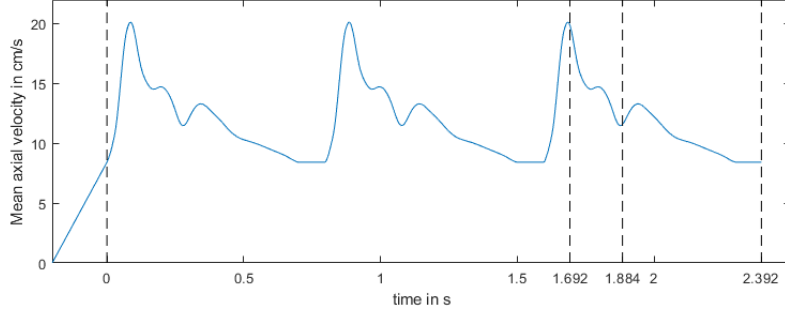


Figure 3.22: Mean axial velocity applied at the inlet for pulsatile flow.

The 2D and 3D simulations are performed differently. Their key differences are depicted in Table 3.5. The 3D simulations are performed with FEBio, which uses finite element methods in their simulation, while the 2D ROM is simulated with finite volume methods. The type of simulation affects the time step size. The 2D ROM incorporates an explicit time integration scheme, which has to satisfy the CFL condition. FEBio incorporates an implicit time integration scheme that allows for a time step size of 1 ms, the time step size for the data shown in Figure (3.22). Linear interpolation is used to obtain the mean axial velocity between two data points for the 2D simulation.

Table 3.5: Differences between 3D- and 2D simulation set up.

Simulation	3D	2D
Numerical solver	Finite element methods	Finite volume methods
Time integration method	Implicit	Explicit
Time step size	1000 μ s	3.125 μ s
Pres	9330 Pa	7205.2 Pa
Qres	1.358 E9 Pa s / m ³	5.7817 E9 Pa s / m ³
Change in Young's modulus	Discontinuous	Smooth
Velocity applied at inlet (for $t < 0$)	See Figure 3.22	Obtain steady-state solution

The properties of the fluid resistance boundary condition are set up differently between the two simulations. The fluid resistance boundary condition is set up such that the systolic pressure should be 120 mmHg (≈ 16.00 kPa) and the diastolic pressure should be 80 mmHg (≈ 10.67 kPa). For the 3D simulation P_{res} and R_{res} chosen identically to [20]. The 2D simulations have lower volumetric flow rates than 3D simulations. Due to the fluid resistance boundary condition, a lower flow rate leads to a lower pressure range within the simulation. Values of P_{res} and Q_{res} have been fitted for the 2D ROM to match systolic and diastolic pressure of 16.00 kPa and 10.67 kPa.

The most significant difference between the 3D and 2D simulations is modeling the artery's Young's modulus. The 3D model has jump discontinuity in the artery's Young's modulus. This jump discontinuity has been smoothed out for the 2D model. The smoothing process is computed by (2.2.60), where $\Delta\xi = 1$, $\xi^x = 1/4$ and $\xi^\varphi = \frac{3}{8}\pi$. Remark that these simulations were performed before the research within Section 3.3. A different choice for ξ^φ would better match the 3D simulations.

The least significant difference is how the initial value (state at $t = 0$) is obtained. The 3D simulation applies a load curve (2.3.1) to R_{res} , Q_{res} and incorporates a mean axial velocity depicted in Figure 3.22. The 2D ROM starts the simulation with pulsatile flow by taking the steady-state solution as an initial condition.

This section starts with studying the simulations without calcification and proceeds to simulations with axisymmetric calcification and local calcification. These simulations focus on the results of 15 different cells, where $i \in \{1, 39, 61, 82, 120\}$ and $j \in \{4, 15, 25\}$ (see Figure 2.6 for the 2D mesh). $i = 1$ and $i = 120$ are the columns neighboring the inlet and outlet. $i = 61$ is the column in the middle of the calcified area (if present). There is only one column between $i = 39/i = 82$ and the calcified area (if present). The rows are only relevant for the local calcification model. $j = 25$ is a row in the middle of the calcified area, $j = 15$ is located in the middle of the smooth transition, and $j = 4$ is far outside the calcified area.

3.4.1. No Calcification

Simulation of blood flow without calcification are shown in Figure (3.23), Figure (3.24) and Figure (3.25). Pressure within the last periodic cycle is between the range of 16.09 kPa and 12.03 kPa for the 3D simulation (see Figure 3.23a) and between 15.88 kPa and 10.66 kPa for the 2D simulation (see Figure 3.23b). The 3D simulation overshoots the diastolic pressure by 1.36 kPa. The diastolic pressure for the 2D simulation and systolic pressure are sufficiently close to the specified target. The pressure difference across the artery seems neglectable. The maximum pressure difference is 43.59 Pa for the 3D simulation and 39.52 Pa for the 2D simulation.

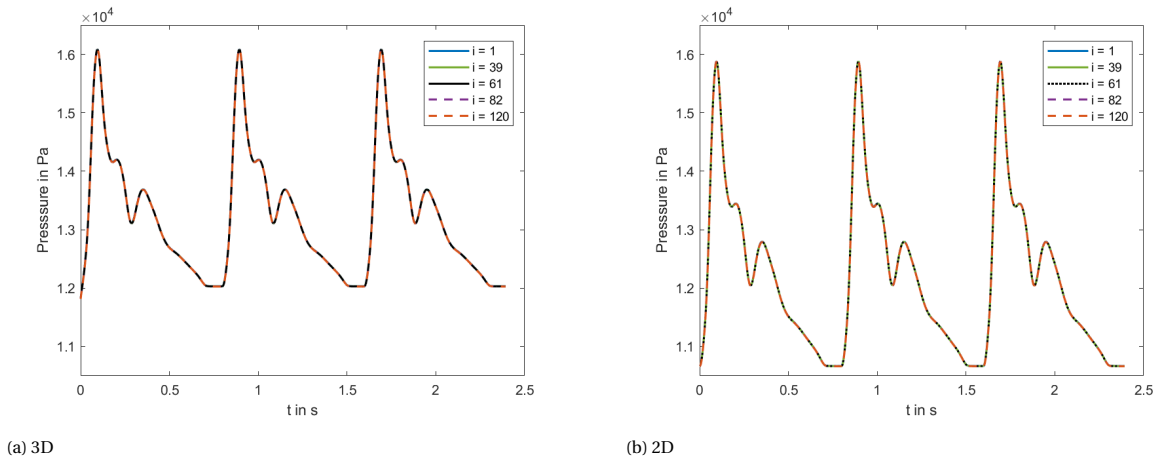


Figure 3.23: Pressure observed for the 3D and 2D simulations without calcification.

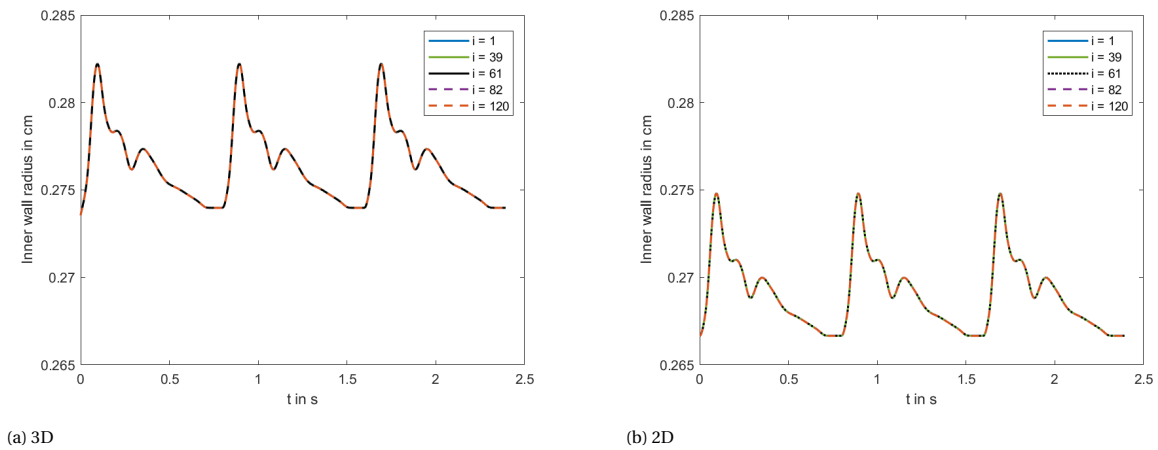


Figure 3.24: Inner wall radius observed for the 3D and 2D simulations without calcification.

The inner wall radius for the 3D simulation is about 70 μm higher during the 2D simulation. The inner wall radius has a range between 0.2822 cm and 0.2740 cm for the 3D simulation (see Figure 3.24a) and a

range between 0.2748 cm and 0.2677 cm for the 2D simulation (see Figure 3.23b). The maximum observed fluctuation radius (for a fixed time) is 0.8342 μm for the 3D simulation and is 0.7056 μm for the 2D simulation.

Velocity profiles are shown Figure 3.25 at three different times. The maximum velocity at the inlet occurs at $t = 1.692$ s, the second local minimum (for the third periodic cycle) occurs at $t = 1.884$ s, and the simulation ends at $t = 2.393$ s. Figure 3.25a and Figure 3.25b indicates that information travels faster in the 2D simulation. These figures show that the velocity profile across the artery is nearly identical to the 2D simulation. Meanwhile, 3D simulations have different velocity profiles across the artery. The larger the distance between the measured cells and the inlet, the more each velocity profile lags behind the inlet. At time $t = 2.393$ s, the inlet has been constant for enough time that all velocity profiles are nearly identical.

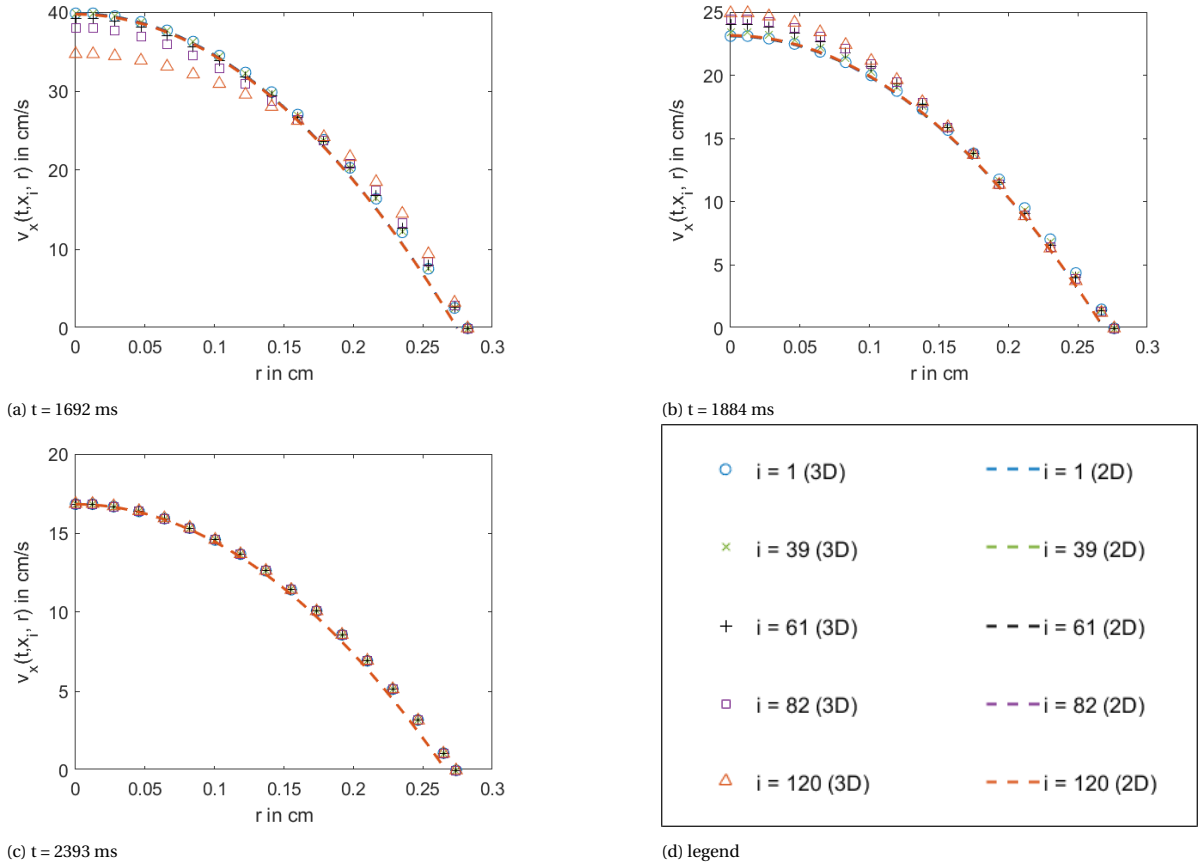


Figure 3.25: Velocity profile observed for the 3D and 2D simulations without calcification.

Table 3.6 shows the volumetric flow rate at each cross section i for the 3D and 2D simulation. The volumetric flow rate in the 3D simulation is numerically obtained with Matlab's 'trapsz'. The volumetric flow rate within for 2D simulation is evaluated as $\frac{1}{2} \sum_j Q_{i,j}$, since A has been substituted with R^2 (not $\frac{1}{2}R^2$). The volumetric flow rate is about 5% higher in the 3D simulation. Mass within the artery seems to be conserved at time $t = 2.393$ s for both simulations.

Figure 3.26 shows the relative error (in 2-norm) between the velocity profile from the 3D simulation and its closest velocity profile included in the 2D ROM (see (2.2.2) where u is computed with the least squares method). Figure 3.26a and Figure 3.26b clearly show that not all velocity profiles in the 3D simulations are parabolic. For $t = 1.692$ the 3D velocity profiles becomes more flat ($\gamma \rightarrow \infty$) as i increases, whereas for $t = 1.884$ they become more linear ($\gamma \downarrow 1$) as i increases. For $t = 2.393$ s, all 3D velocity profiles are parabolic.

Table 3.6: Flow rate $Q(t, x_i)$ in cm^3/s observed from the 3D and 2D simulation without calcification.

t (in s)	Simulation	i = 1	i = 39	i = 61	i = 82	i = 120
1.693	3D	4.959	4.954	4.950	4.945	4.936
	2D	4.725	4.721	4.719	4.716	4.711
1.884	3D	2.754	2.756	2.758	2.760	2.763
	2D	2.622	2.624	2.625	2.626	2.628
2.393	3D	1.974	1.974	1.974	1.974	1.974
	2D	1.879	1.879	1.879	1.879	1.879

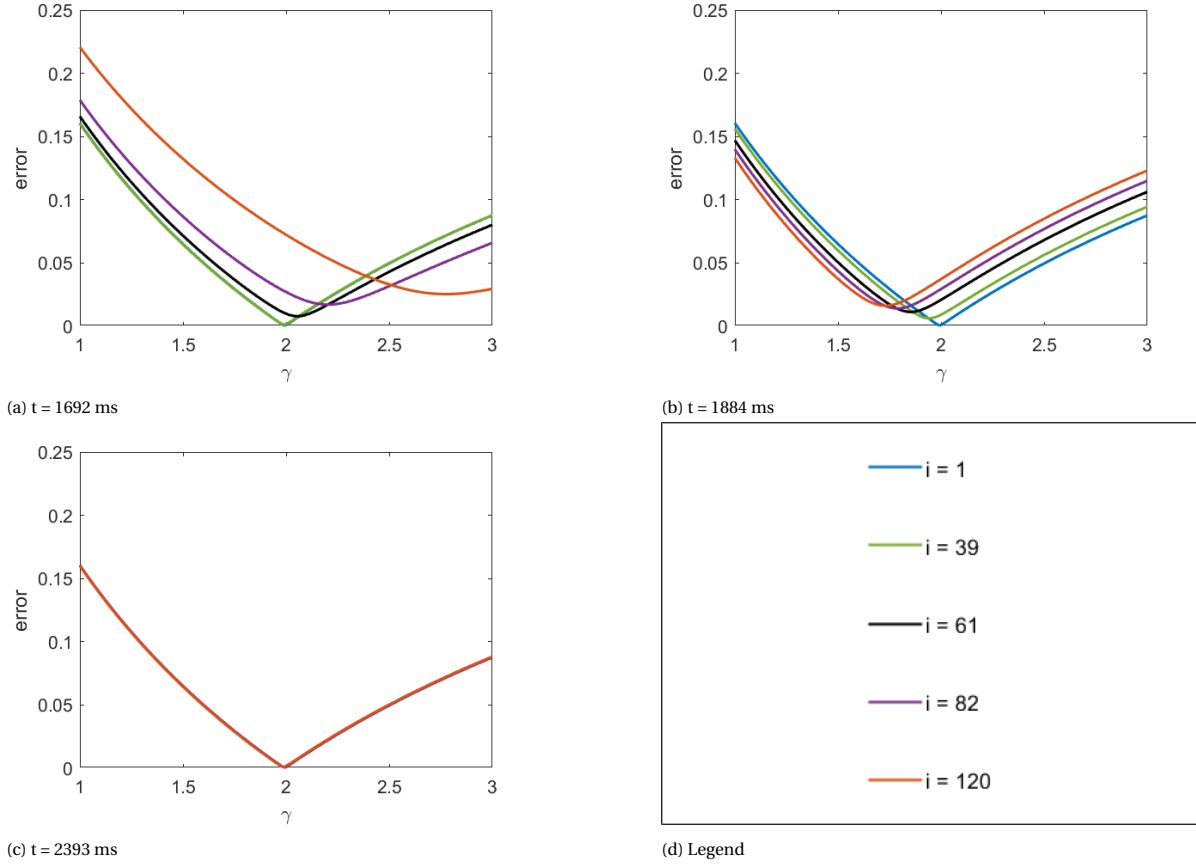


Figure 3.26: Relative error measured between the velocity profiles obtained from the 3D simulations without calcification and its closest velocity profile allowed in the 2D ROM.

3.4.2. Axisymmetric Calcification

Simulation of blood flow with axisymmetric calcification are shown in Figure 3.27, Figure 3.28 and Figure 3.29. Pressure has a range between 16.10 kPa and 12.00 kPa for the 3D simulation (see Figure 3.27a) and a range between 16.21 kPa and 10.66 kPa (see Figure 3.27b). For the 3D simulation, the arterial pressure observed with axisymmetric calcification is comparable to that without calcification. The 2D simulation with axisymmetric calcification overshoots pressure near and in the calcified area. Pressure near the inlet and outlet is comparable to pressure without calcification. This phenomenon most likely occurs since the 2D model smooths the jump discontinuity of the artery's Young's modulus over 10 cells. The pressure difference (at a fixed time during the third cycle) is 56.07 Pa and 244.0 Pa for the 3D and 2D simulations. The pressure difference is much higher for the 2D ROM since the 2D simulation overshoots pressure in and near the calcified area.

The inner wall radius of the 3D and 2D simulations are depicted in Figure 3.28. The radii at the inlet and outlet with axisymmetric calcification are comparable with radii without calcification for both simulations.

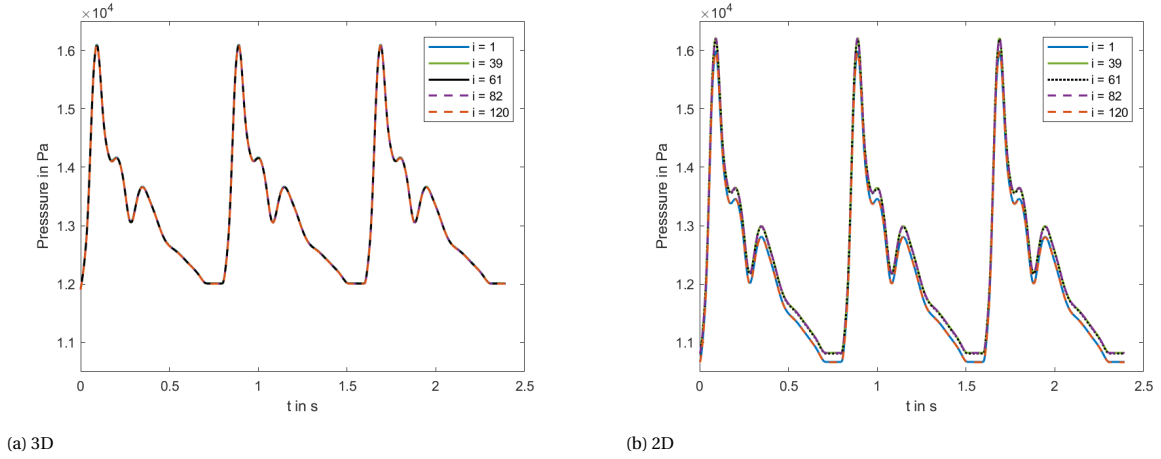


Figure 3.27: Pressure observed for the 3D and 2D simulations with axisymmetric calcification.

The inner wall radius inside the calcified area is significantly smaller (with a maximum fluctuation of $52.31 \mu\text{m}$) than the inner wall radius near the calcified area for the 3D simulation. However, for the 2D simulation, the inner radius inside of the calcified area is slightly lower (with a maximum fluctuation of $0.22 \mu\text{m}$) than the radius near the calcified region. This difference between the 3D and 2D simulation is a direct consequence of different Young's modulus near the calcified region between the 3D model and the 2D ROM.

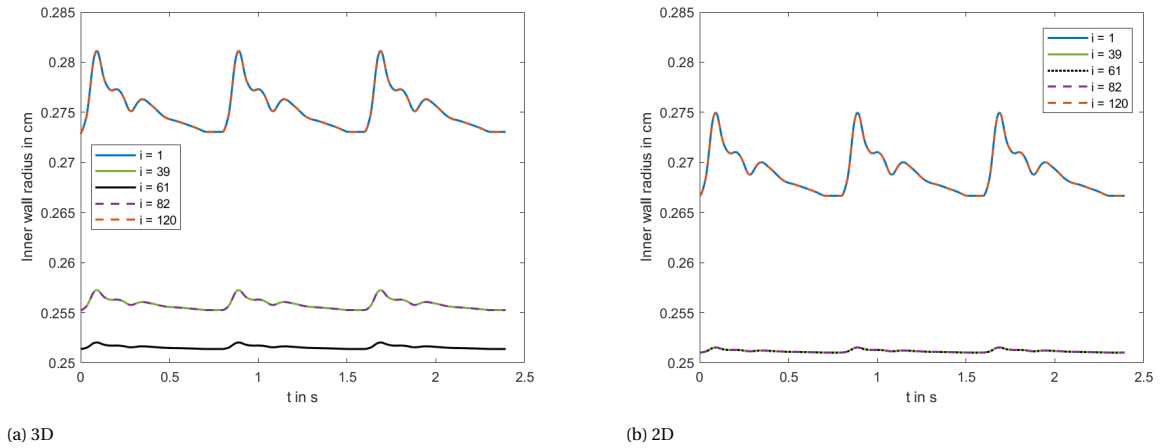


Figure 3.28: Inner wall radius observed for the 3D and 2D simulations with axisymmetric calcification.

The velocity profile for each cell is depicted in Figure 3.29 at three different times, and their corresponding flow rate is depicted in Table 3.7. The 2D velocity profiles are parabolic; the inlet and outlet velocity profiles are comparable and have a lower mean axial velocity than those near and in the calcified area. For the 3D simulation, the velocity at the artery's origin is always higher near and in the calcified region. Counterintuitive to our judgment, the volumetric flow rate at the inlet is lower at $t = 1.693 \text{ s}$ and (slightly) higher at $t = 1.884 \text{ s}$ to the volumetric flow rate at the outlet. They are both similar at $t = 2.393 \text{ s}$, indicating that mass is (almost) conserved within the artery at the end of the simulation. Remark that the 2D simulation always has dents in the volumetric flow rate before the calcified region and humps after the calcified region. The actual flow rate at $i = 39$ and $i = 82$ should be higher and lower than the simulated flow rate. Flow rates within the 3D simulation are about $1.89\% \sim 6.69\%$ larger than flow rates within the 2D simulation.

Relative error (in 2-norm) between the velocity profile obtained in the 3D simulation and its closest approximated velocity profile included in the 2D ROM are shown in Figure 3.30. These figures show that not all velocity profiles within the 3D simulation are parabolic. The velocity profiles in and near the calcified area

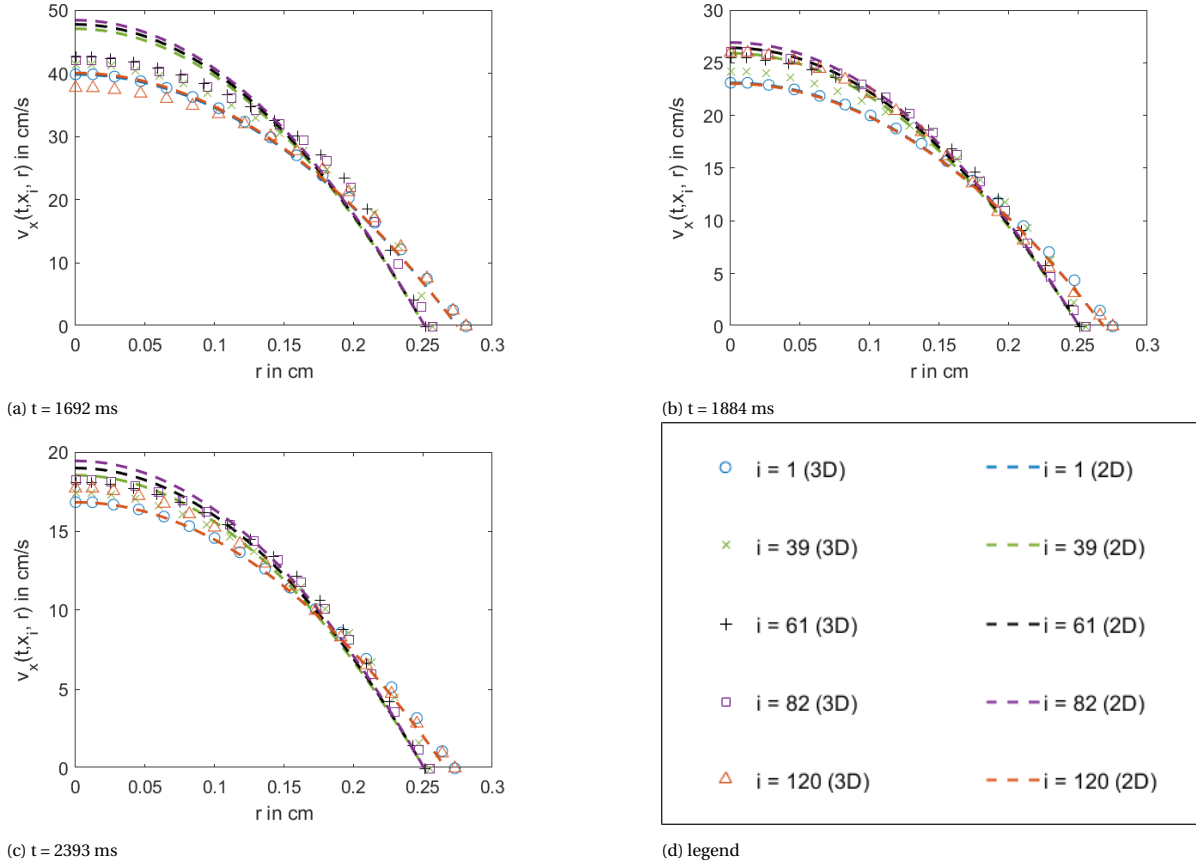


Figure 3.29: Velocity profile observed for the 3D and 2D simulations with axisymmetric calcification.

have become more flat ($\gamma \rightarrow \infty$). The velocity profile at the outlet becomes more flat at $t = 1.692$ s and more linear ($\gamma \downarrow 1$) at $t = 1.884$ s and $t = 2.393$ s. The velocity profiles at the inlet are parabolic since a parabolic velocity profile is prescribed at the inlet.

3.4.3. Local Calcification

Simulation of blood flow with local calcification is shown in figures 3.31 - 3.35. Pressure within the 3D simulation with local calcification (see Figure 3.31) is similar to pressure without calcification (see Figure 3.23). For the 2D simulation, pressure is only similar to the pressure without calcification if the artery's Young's modulus is equal to the Young's modulus of a healthy artery. In cases where the artery's Young's modulus is higher than a healthy artery's Young's modulus, pressure either is too high ($j = 25$, $i \in \{39, 61, 82\}$) or too low ($j = 15$, $i \in \{39, 61, 82\}$). Remark that for the 2D simulation, pressure for $j = 4$ is similar to pressure without calcification, and pressure for $j = 25$ is identical to pressure with axisymmetrical calcification.

From section 3.3.2 we know that pressure can have oscillations in the smoothening region where $\varphi \in (\frac{3}{4}\pi -$

Table 3.7: Flow rate $Q(t, x_i)$ in cm^3/s observed from the 3D and 2D simulation with axisymmetric calcification.

t (in s)	Simulation	$i = 1$	$i = 39$	$i = 61$	$i = 82$	$i = 120$
1.693	3D	4.916	4.917	4.922	4.929	4.939
	2D	4.730	4.675	4.743	4.811	4.755
1.884	3D	2.731	2.724	2.726	2.728	2.728
	2D	2.621	2.567	2.617	2.667	2.613
2.393	3D	1.959	1.957	1.958	1.960	1.960
	2D	1.879	1.835	1.879	1.924	1.879

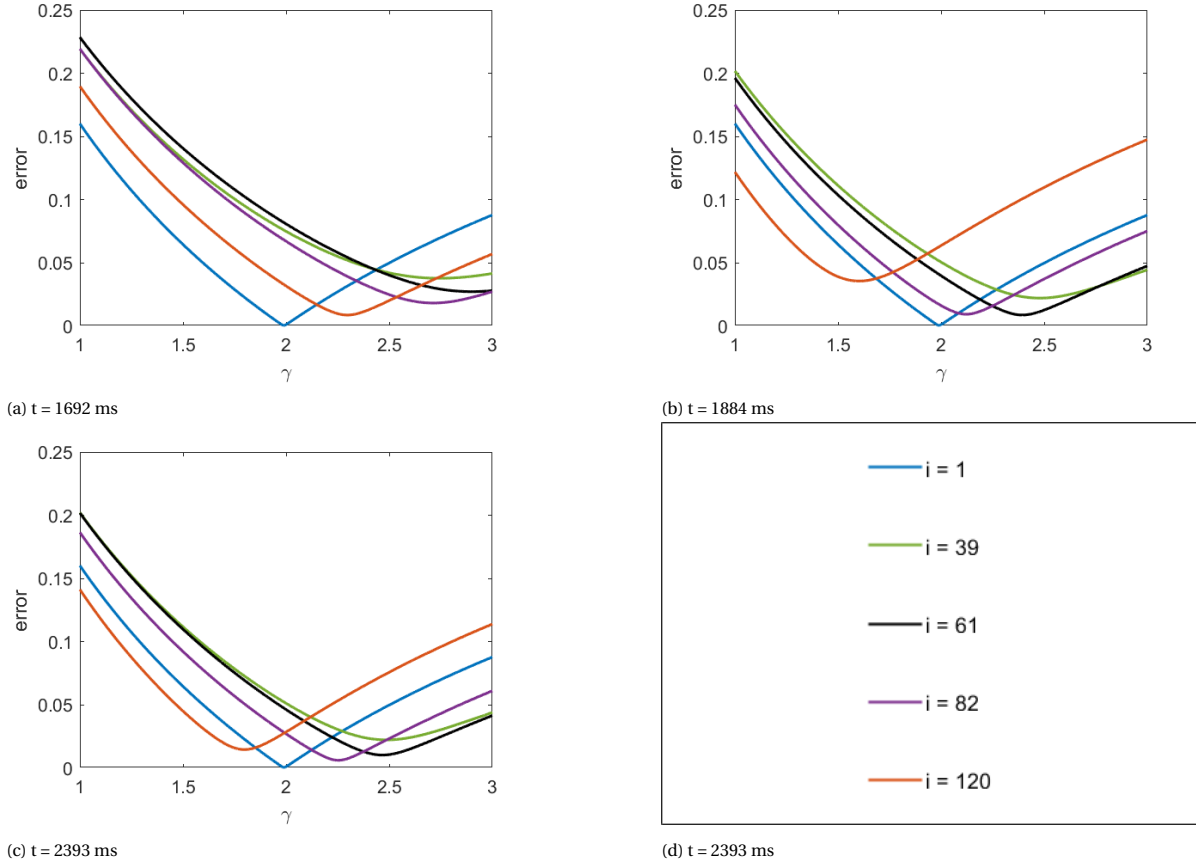


Figure 3.30: Error measured between the velocity profiles obtained from the 3D simulations with axisymmetric calcification and its closest velocity profile allowed in the 2D ROM.

$\xi^\varphi, \frac{3}{4}\pi) \cup (\frac{5}{4}\pi, \frac{5}{4}\pi + \xi^\varphi)$ if $\xi^\varphi / \Delta\varphi$ is larger than 3. For this simulation, $\xi^\varphi / \Delta\varphi = 9$ is significantly larger than 3; thus, oscillations can be expected. The pressure drop seen for $j = 15$, $i \in \{39, 61, 82\}$ occurs due to these oscillation. Consequently, pressure within the 2D simulation within these ranges cannot be trusted.

Inner wall radius for the 2D and 3D simulations are depicted in Figure 3.32. The inner wall radius at the inlet and outlet are similar to the inner wall radius without calcification. For the 3D simulation, the inner wall radius near and in the calcified region ($i \in \{39, 61, 82\}$) is slightly increased compared to the inner wall radius at the inlet/outlet for $j = 4$, whereas it is significantly decreased for $j \in \{15, 25\}$. For the 2D simulation, the inner wall radius near and in the calcified region is similar to the inner wall radius at the inlet/outlet for $j = 4$, while it is significantly lower than the inlet/outlet for $j \in \{15, 25\}$.

Velocity profiles for the 3D and 2D simulations are depicted in Figure 3.33, Figure 3.34, and Figure 3.35 at $t = 1.692$ s, $t = 1.884$ s, and $t = 2.393$ s. Their corresponding volumetric flow rate is shown in Table 3.8 for the 3D simulation and in Table 3.9 for the 2D simulation. Axial velocity within the artery's origin ($v_x|_{r=0}$) has the same value for $j \in \{4, 15, 25\}$ within each cross-section, indicating that Assumption 5 (Continuous blood flow at the origin of the artery), which is added to the 2D ROM, should also hold for the 3D simulation. However, more data points are needed to validate this assumption. The velocity profiles for $j = 15$ and $j = 25$ are similar for the 2D simulation but not for the 3D simulation. This difference most likely occurred because the artery's Young's modulus has different values near the calcified area between the 3D and 2D models.

Flow rate within the 3D simulation is -3.67% ~ 12.17% larger than flow rate within the 2D simulation. The 2D simulation has a higher flow rate for $t = 2.393$ s and $i \in \{39, 61\}$. Mass within the artery is almost conserved at $t = 2.393$ s for the 2D simulation; $2.620 \text{ E-}5 \text{ cm}^3/\text{s}$ more blood flows out of the domain than into the domain. Due to insufficient data points, it is impossible to validate if the 3D simulation conserves mass at $t = 2.393$ s.

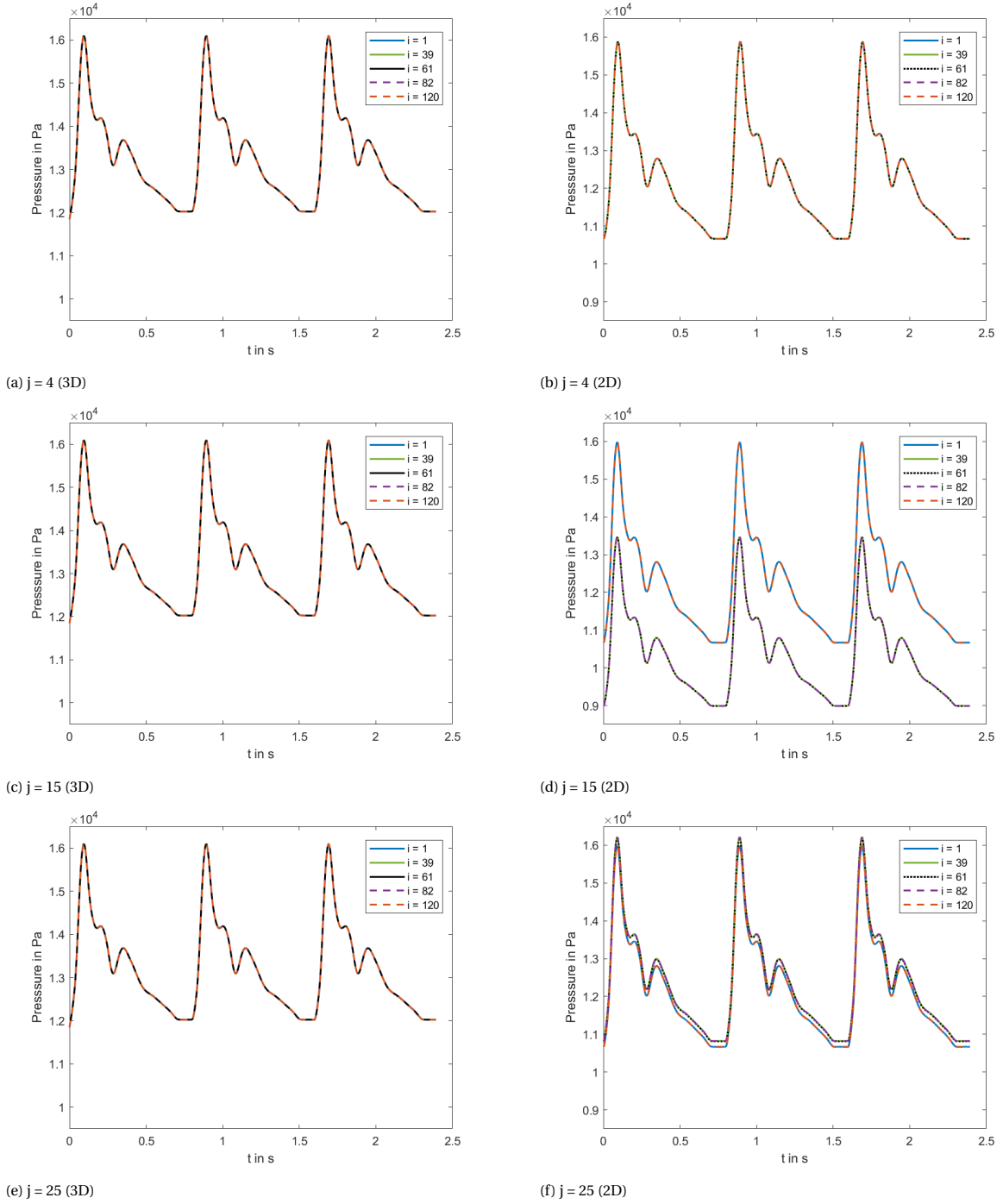


Figure 3.31: Pressure observed for the 3D and 2D simulations with local calcification.

γ from the 2D ROM is depicted in Figure 3.36. γ within the 2D ROM is obtained by averaging the velocity profile around $\gamma = 2$. Figure 3.36b, Figure 3.36c and Figure 3.36d shows that the velocity profiles become more flat ($\gamma \rightarrow \infty$) in and near the calcified region and more linear ($\gamma \downarrow 1$) in the healthy region of the artery. The velocity profiles adjacent to the inlet are parabolic since a parabolic velocity profile is prescribed at the inlet (see Figure 3.36a). Velocity profiles adjacent to the outlet remain relatively close to the parabolic velocity profile.

The 3D simulations without calcification and simulations with axisymmetric calcification already show that

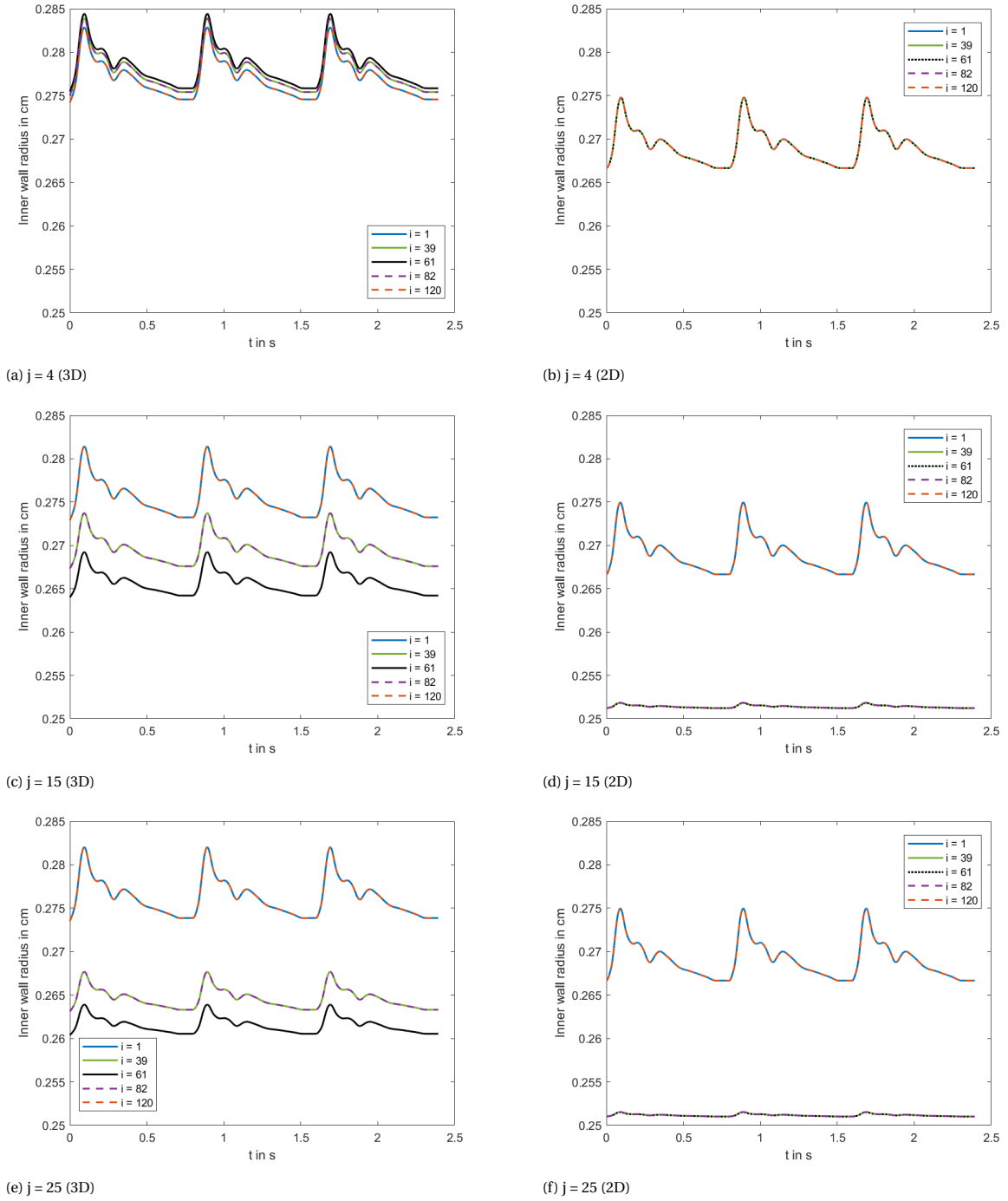


Figure 3.32: Inner wall radius observed for the 3D and 2D simulations with local calcification.

velocity profiles are not always parabolic, indicating that averaging around $\gamma = 2$ does not yield the most accurate velocity profiles. More data points in the 3D simulations are necessary to determine the validity of obtaining γ by averaging. However, for the cross section $i = 61$ we can clearly see that γ for $j \in \{15, 25\}$ is larger than γ for $j = 4$ (see Figure 3.37g, Figure 3.37h and Figure 3.37i). This also hold true for cross section $i = 39$ (see Figure 3.37d, Figure 3.37e and Figure 3.37f), but not for $i = 82$ (see Figure 3.37j, Figure 3.37k and Figure 3.37l). Averaging γ within cross-section $i = 82$ in the 2D ROM leads to different behavior than velocity profiles shown within the 3D velocity profiles.

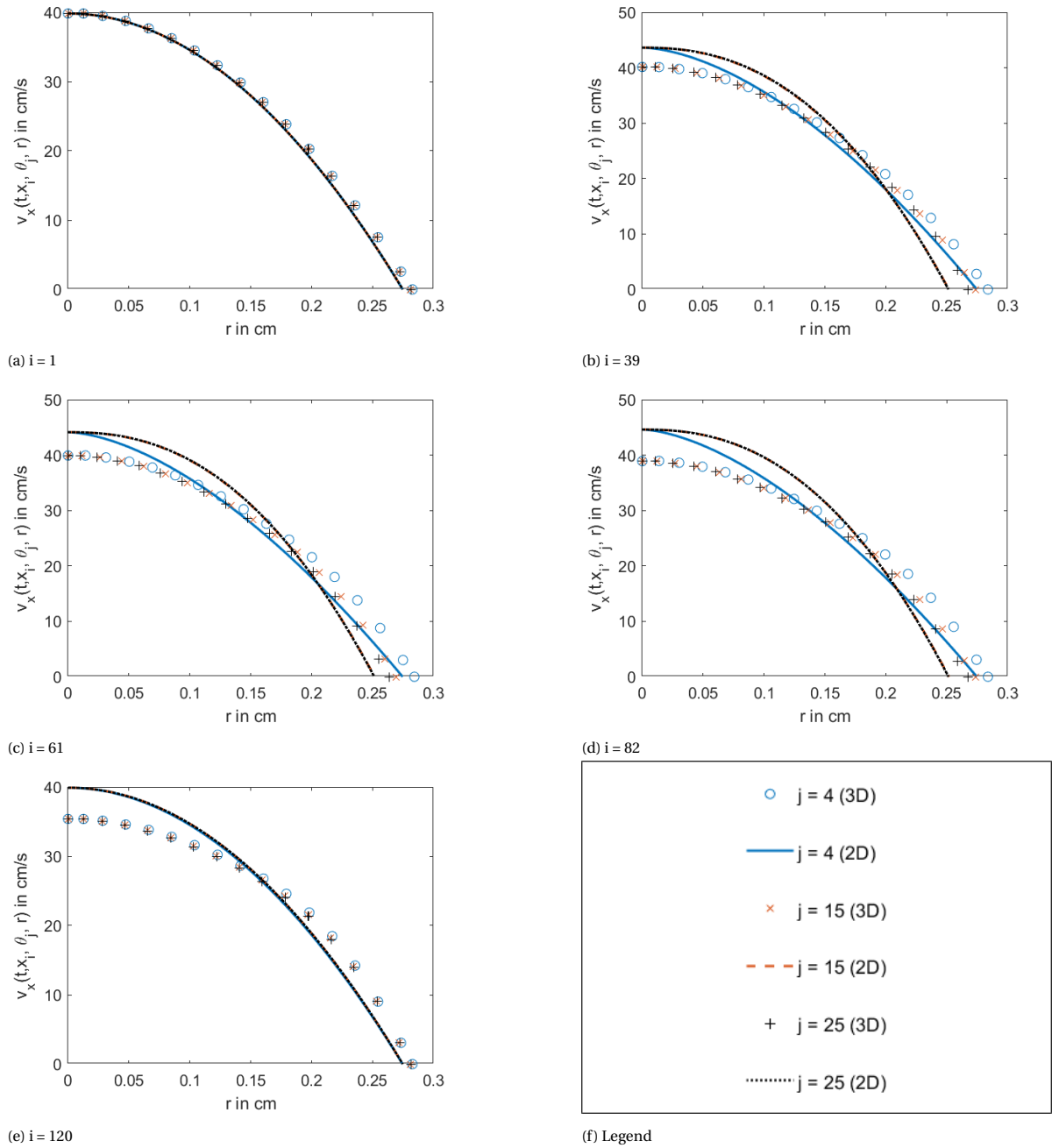


Figure 3.33: Velocity profile observed for the 3D and 2D simulations with local calcification at $t = 1.692$ s.

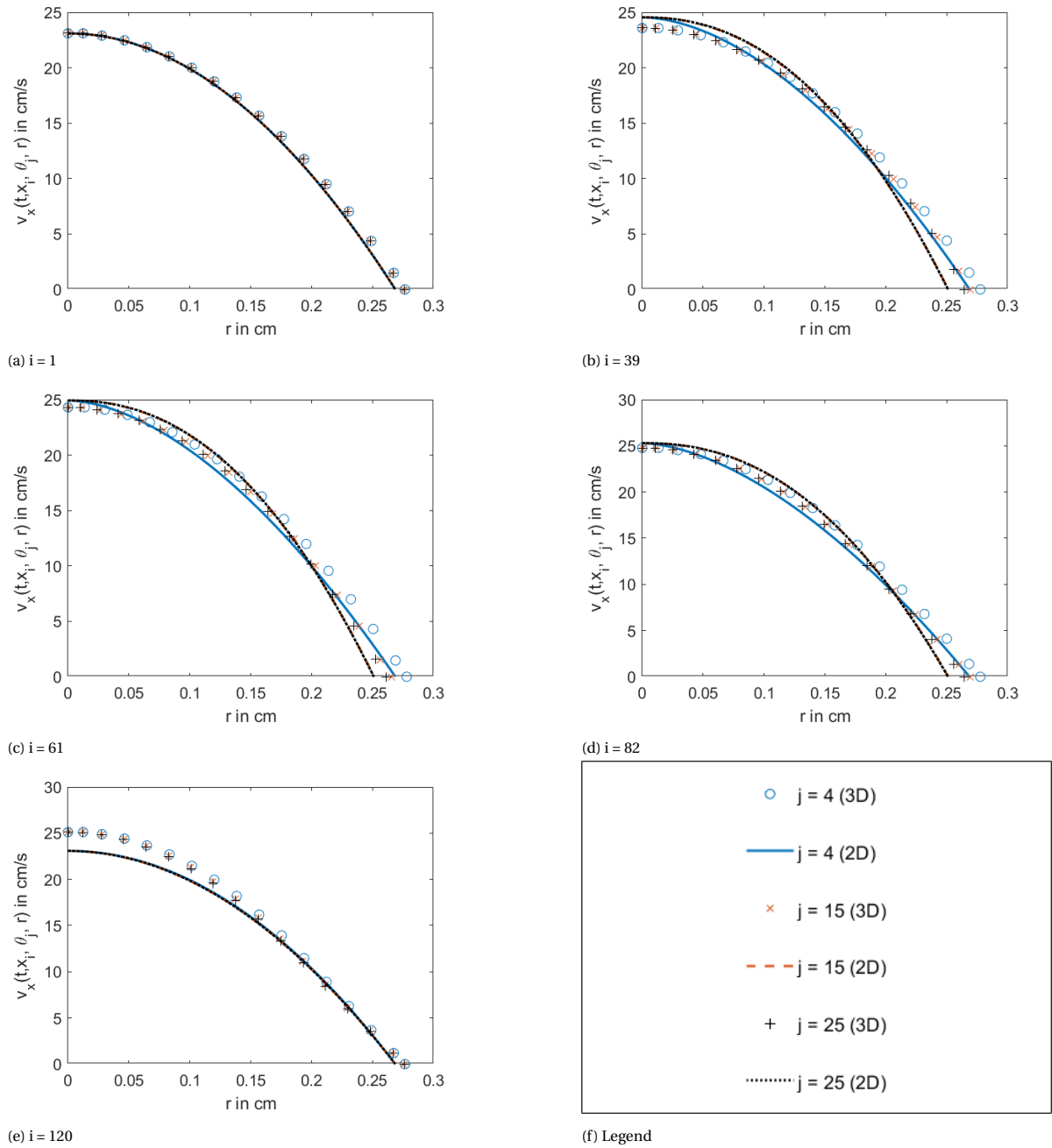


Figure 3.34: Velocity profile observed for the 3D and 2D simulations with local calcification at $t = 1.884$ s.

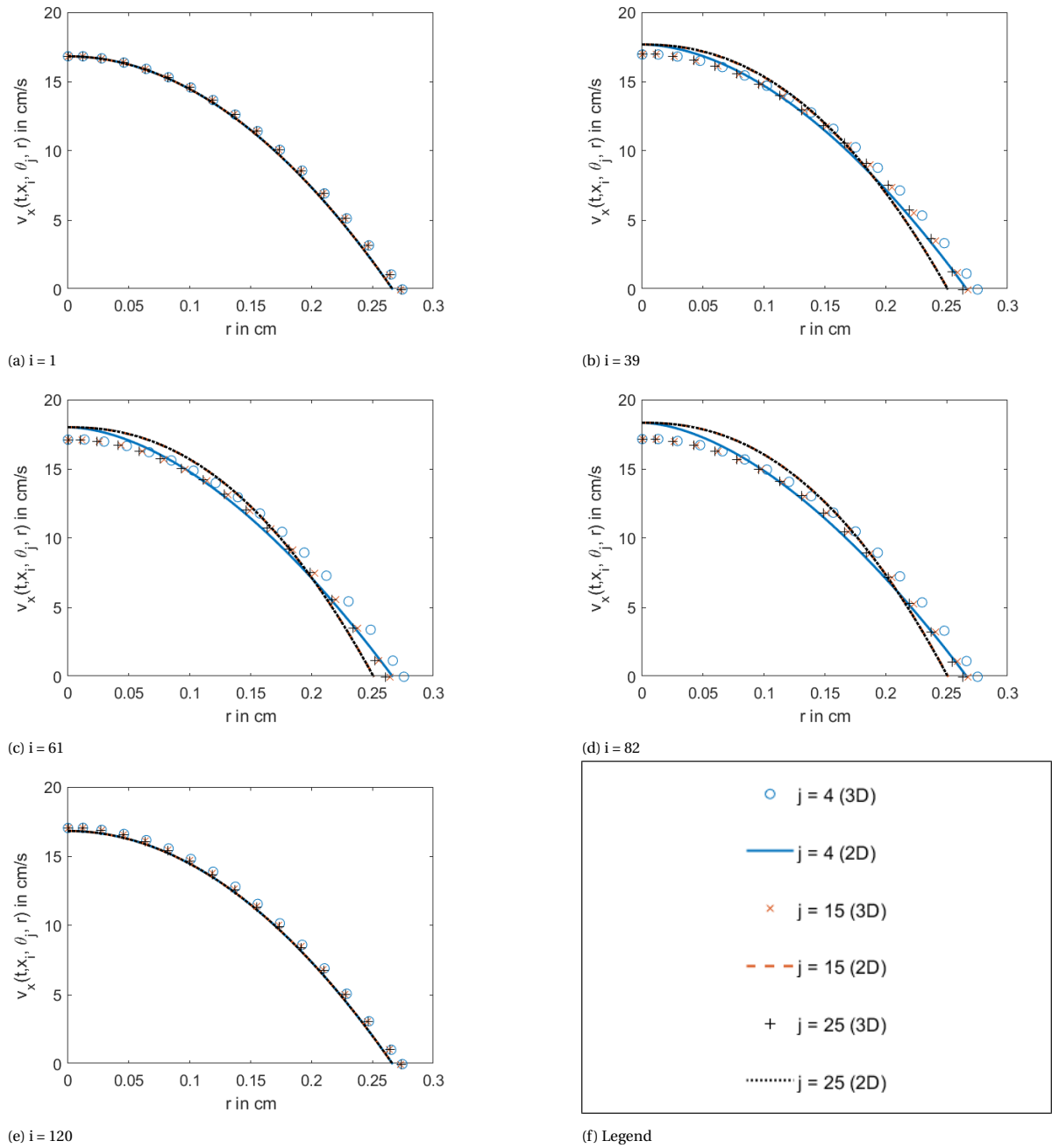


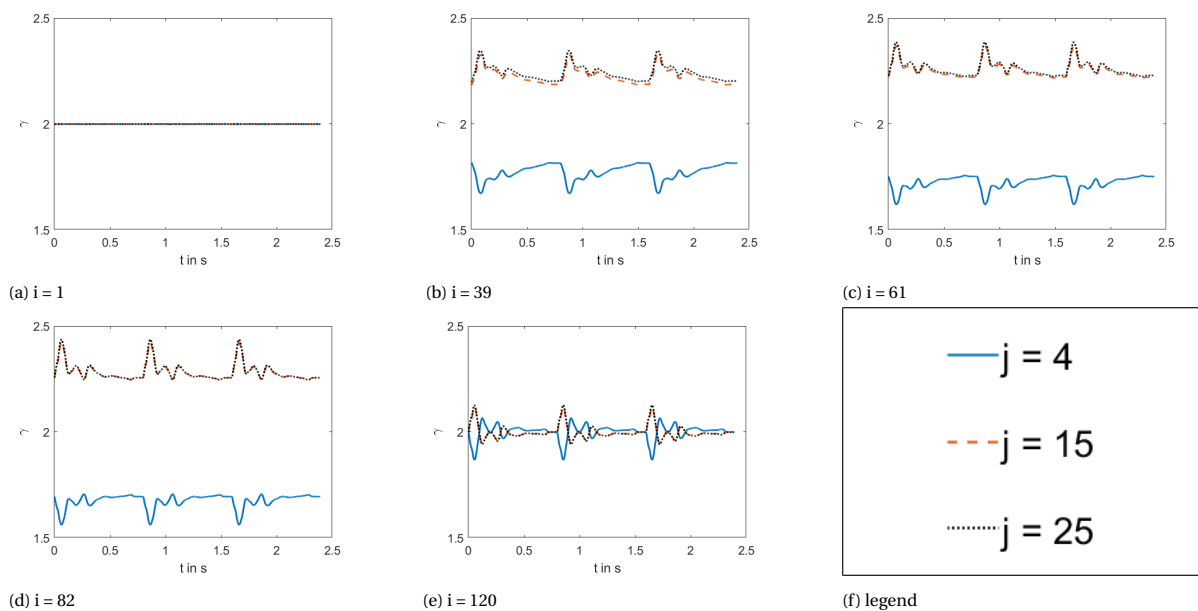
Figure 3.35: Velocity profile observed for the 3D and 2D simulations with local calcification at $t = 1.884$ s.

Table 3.8: Flow rate $Q(t, x_i, \varphi_j)$ in cm^3/s observed from the 3D simulation with local calcification.

j	t (in s)	i = 1	i = 39	i = 61	i = 82	i = 120
4	1.692	0.1039	0.1075	0.1103	0.1098	0.1043
	1.884	0.0577	0.0593	0.0605	0.0603	0.0585
	2.393	0.0413	0.0426	0.0434	0.0432	0.0416
15	1.692	0.1026	0.1016	0.1004	0.1008	0.1024
	1.884	0.0570	0.0565	0.0560	0.0562	0.0568
	2.393	0.0409	0.0405	0.0401	0.0403	0.0408
25	1.692	0.1030	0.0990	0.0963	0.0965	0.1022
	1.884	0.0572	0.0555	0.0544	0.0544	0.0565
	2.393	0.0410	0.0397	0.0389	0.0390	0.0407

Table 3.9: Flow rate $Q(t, x_i, \varphi_j)$ in cm^3/s observed from the 2D simulation with local calcification.

j	t (in s)	i = 1	i = 39	i = 61	i = 82	i = 120
4	1.692	0.0984	0.0984	0.0983	0.0983	0.0982
	1.884	0.0546	0.0547	0.0547	0.0547	0.0547
	2.393	0.0392	0.0392	0.0392	0.0392	0.0392
15	1.692	0.0985	0.0973	0.0988	0.1003	0.0991
	1.884	0.0546	0.0534	0.0545	0.0557	0.0544
	2.393	0.0392	0.0382	0.0392	0.0402	0.0392
25	1.692	0.0985	0.0974	0.0988	0.1002	0.0991
	1.884	0.0546	0.0535	0.0545	0.0556	0.0544
	2.393	0.0392	0.0382	0.0392	0.0401	0.0392

Figure 3.36: Simulated γ for the 2D ROM with local calcification.

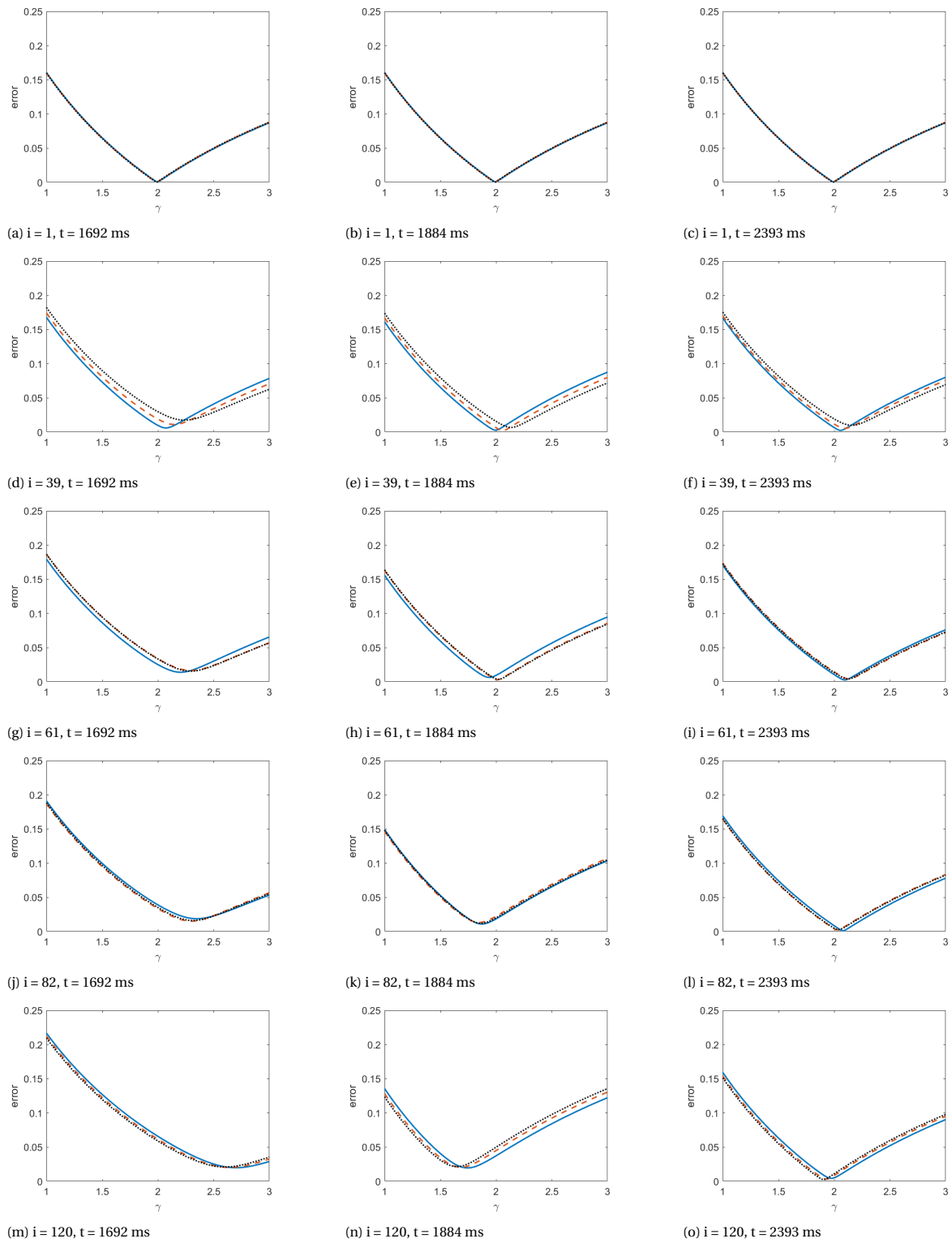


Figure 3.37: Error measured between the velocity profiles obtained from the 3D simulations with local calcification and its closest velocity profile allowed in the 2D ROM. The blue solid line, orange dashed line, and black dotted line represent $j = 4$, $j = 15$, and $j = 25$, respectively.

Validating Assumption 4

Assumption 4 (dominance in axial velocity) has been included in the 2D ROM since axial velocity was expected to be much larger than its orthogonal components. This section quantifies how dominant axial velocity is within the 3D ROM.

The 3D simulations with pulsatile flow had no backflow. Every element within the 3D simulations had a strictly positive axial velocity for $t \geq 0$. Rescaling velocity as $\mathbf{u} = \mathbf{v}/v_x$ quantifies how dominant axial velocity is. $\max\{u_r\}$ within the 3D simulation with local calcification is shown in Table 3.10 for different locations, and $\max\{u_\varphi\}$ is shown in Table 3.11. These tables show that $\max u_r = 0.16928$ and $\max u_\varphi = 0.09734$, making Assumption 4 (dominance in axial velocity) reasonable.

Table 3.10: The maximum rescaled velocity $\max u_r$ at different locations from the 3D simulation with local calcification.

$\max u_r(t, x_i, \varphi_j)$	$i = 1$	$i = 39$	$i = 61$	$i = 82$	$i = 120$
$j = 4$	0.09734	0.06283	0.05729	0.05552	0.16738
$j = 15$	0.08353	0.05830	0.03282	0.06876	0.16896
$j = 25$	0.08325	0.13079	0.02148	0.13044	0.16928

Table 3.11: The maximum rescaled velocity $\max u_\varphi$ at different locations from the 3D simulation with local calcification.

$\max u_\varphi(t, x_i, \varphi_j)$	$i = 1$	$i = 39$	$i = 61$	$i = 82$	$i = 120$
$j = 4$	0.09851	0.01988	0.01221	0.03265	0.01697
$j = 15$	0.00368	0.05722	0.02103	0.08699	0.03672
$j = 25$	0.00023	0.00368	0.00126	0.00505	0.00273

4

Conclusion

This study obtains a 2D reduced order model (ROM) for blood flow that can model asymmetric calcification by studying the following research questions:

- 1) What is the mathematical expression for the 2D ROM that can model blood flow asymmetrically?
- 2) How to develop a numerical method for the 2D ROM?
- 3) How well do 2D simulations compare with 3D simulations?

The 2D ROM is acquired by removing the dimension corresponding to the radial distance 'r' from the 3D model. The 2D ROM applies the same assumptions as the 1D ROM except for the assumption of 'axial symmetry.' This assumption is replaced by the boundary condition $\partial_\varphi v_x|_{r=0} = 0$, where v_x is the axial velocity of blood. This paper contributes to hemodynamics by allowing a family of velocity profiles $s(y, \gamma) = \frac{\gamma+2}{\gamma}(1-y^\gamma)$ within the ROM, where $y \in [0, 1]$ is a rescaled radius and $\gamma > 0$ is dimensionless and influences the shape of the velocity profile. This velocity profile is used in the 1D ROM by predetermining γ in advance. The 2D ROM lets γ depend on the temporal and spatial coordinates. The following equations govern the 2D ROM

$$\partial_t(R^2) + \partial_x(uR^2) = 0, \quad (2.2.33)$$

$$\begin{aligned} \rho \partial_t(uR^2) + \rho \frac{\gamma+2}{\gamma+1} \partial_x(u^2 R^2) = & u^2 R^2 \frac{5\gamma+4}{2\gamma(\gamma+1)^2} \partial_x \gamma + 2\mu u \frac{\gamma+2}{\gamma} \left(-\gamma + (\gamma+2) \frac{\partial_\varphi^2 R}{R} \right. \\ & \left. - \frac{\gamma+1}{2} \frac{\partial_\varphi^2(R^2)}{R^2} + 2 \frac{\gamma-1}{\gamma^2} \partial_\varphi \gamma \frac{\partial_\varphi R}{R} - \frac{2}{\gamma^3} (\partial_\varphi \gamma)^2 + \frac{1}{\gamma^2} \partial_\varphi^2 \gamma \right) - \frac{R^2 \partial_x R}{R_0^2} \beta - R^2 \frac{R-R_0}{R_0^2} \partial_x \beta, \end{aligned} \quad (2.2.34)$$

$$\partial_\varphi \left(\frac{\gamma+2}{\gamma} u \right) = 0, \quad (2.2.35)$$

where $u(t, x, \varphi)$ (mean axial velocity), $R(t, x, \varphi)$ (inner wall radius) and $\gamma(t, x, \varphi)$ are the unknown functions, ρ is the density of blood, μ is the viscosity of blood, and $\beta(x, \varphi)$ is a dimensionless function which contains the mechanical properties of the vascular wall. All terms written in black are incorporated in the 1D ROM, whereas those written in blue are added to the ROM to account for asymmetric flow. Equation (2.2.33) conserves mass within the artery, equation (2.2.34) balances momentum within the artery, and equation (2.2.35) satisfies the boundary condition $\partial_\varphi v_x|_{r=0} = 0$. The boundary condition $\partial_\varphi v_x|_{r=0} = 0$ is changed into the differential equation (2.2.35) since the radial dimension is removed from the 2D ROM.

Numerical methods for the 2D ROM are obtained by incorporating dimensional splitting, which simulates the 2D ROM by solving a sequence of sub-problems numerically. Equation (2.2.35) is satisfied at the end of each iteration by fixing u while computing γ by incorporating a weighted average. Equations (2.2.33) and (2.2.34) are simulated by incorporating Godunov splitting, which leads to a φ -sweep and an x -sweep. The φ -sweep is solved analytically, while the x -sweep is solved numerically by linearizing the problem at each cell interface and incorporating a high-resolution method.

Jump-discontinuities in β (due to calcification) are smoothed out since the x -sweep cannot deal with these jump-discontinuities. The numerical steady-state solution of the 2D ROM admits a numerical error within

the smoothening range of β . More specifically, the volumetric flow rate has humps and dents within the numerical steady-state solution where $\partial_x \beta \neq 0$. The numerical method obtains the analytical steady-state solutions for arteries without calcification. It has a relative error of $\mathcal{O}(\Delta x^{1.500})$. The 2D ROM cannot numerically obtain the non-physiological steady-state solution for arteries with asymmetric calcification due to the numerical errors within the smoothening range.

Simulations with pulsatile flow are done by prescribing a mean axial velocity at the inlet and a fluid resistance boundary condition at the outlet. The 3D and 2D simulations need different parameters for the fluid resistance boundary condition to match a systolic and diastolic pressure of 16.00 kPa (120 mm Hg) and 10.67 kPa (80 mm Hg) without calcification since the 2D ROM leads to lower volumetric flow rates. These parameters are well fitted for the 2D ROM, while the 3D ROM significantly overshoots the diastolic pressure by 1.36 kPa. The 3D simulation without calcification also has a higher inner wall radius than the 2D simulation, and their velocity profiles are not exactly parabolic. The differences in blood flow observed between pulsatile blood flow without calcification and with calcification match decently between the 3D simulations and the 2D simulations, except for locations within the smoothening region.

Limitations and future research

Calcification within the 2D ROM (and 3D model) is applied to all layers within the vascular wall. However, only the medial layer is calcified for medial calcification, so the 2D ROM does not accurately model medial calcification. Future research could more accurately model medial calcification for the 2D ROM by only calcifying the medial layer.

The thin wall model is applied in the 2D ROM as an assumption to relate pressure with the inner wall radius. The thin wall model neglects terms in a 2D framework since the thin wall model is constructed within a 1D framework. It is currently unknown how relevant these terms are for blood flow where calcification is applied asymmetrically.

Numerical error within the 2D ROM mainly occurs where the jump-discontinuity within the artery's mechanical properties are smoothened. This numerical error occurs because the 2D ROM applies dimensional splitting, which solves a linearized Riemann problem for the x-sweep. The linearized Riemann problem cannot deal with discontinuities in the artery's mechanical properties. Future research could implement a numerical method that solves the non-linearized Riemann problem.

Dimensional splitting solves the differential equation (2.2.35) heuristically at the end of each iteration. This differential equation on its own has multiple solutions. The 2D ROM obtains one solution by fixing u and updating γ by incorporating a weighted average within each cross-section. Predictor-corrector methods, similar to the pressure-correction method for the Navier-Stokes equations, should simulate the 2D ROM more accurately.

The 2D ROM incorporates different velocity profiles to deal with asymmetric flow and to ensure that velocity within the artery's origin is continuous. However, the velocity profiles incorporated in the 2D ROM cannot deal with cross sections with strictly positive and negative axial velocity or cross sections where the mean velocity (for a specific angle) is higher than the velocity within the cross section's origin. The numerical steady-state solution with local calcification cannot approximate the analytical steady-state solution where the volumetric flow rate vanishes since the numerical error leads to cross sections with strictly positive and negative mean velocities. Additionally, blood flow within a curved geometry can lead to velocity profiles where the mean velocity (for a specific angle) is higher than the velocity within a cross section's origin. Future research could include more or different velocity profiles for the 2D ROM to handle these limitations. These velocity profiles should be complemented by incorporating the smoothness of axial velocity at the artery's origin.

Bibliography

- [1] Jessica Benitez, Davide Fontanarosa, Jiaqiu Wang, Phani Kumari Paritala, Tim McGahan, Thomas Lloyd, and Zhiyong Li. Evaluating the impact of calcification on plaque vulnerability from the aspect of mechanical interaction between blood flow and artery based on mri. *Annals of Biomedical Engineering*, 49: 1169–1182, 2021.
- [2] Alistair G Brown, Yubing Shi, Alberto Marzo, Cristina Staicu, Isra Valverde, Philipp Beerbaum, Patricia V Lawford, and D Rodney Hose. Accuracy vs. computational time: translating aortic simulations to the clinic. *Journal of biomechanics*, 45(3):516–523, 2012.
- [3] Sunčica Čanić, Josip Tambača, Giovanna Guidoboni, Andro Mikelić, Craig J. Hartley, and Doreen Rosenstrauch. Modeling viscoelastic behavior of arterial walls and their interaction with pulsatile blood flow. *SIAM Journal on Applied Mathematics*, 67(1):164–193, 2006. ISSN 00361399. doi: 10.1137/060651562.
- [4] Zhaoyao Chen, Hui Li, Minghua Wu, Cheng Chang, Xinying Fan, Xinfeng Liu, and Gelin Xu. Caliber of intracranial arteries as a marker for cerebral small vessel disease. *Frontiers in Neurology*, 11:558858, 2020.
- [5] SD Connell and P Stow. The pressure correction method. *Computers & fluids*, 14(1):1–10, 1986.
- [6] Robin Fahraeus and Torsten Lindqvist. The viscosity of the blood in narrow capillary tubes. *American Journal of Physiology-Legacy Content*, 96(3):562–568, 1931.
- [7] Matthew D Ford, Noam Alperin, Sung Hoon Lee, David W Holdsworth, and David A Steinman. Characterization of volumetric flow rate waveforms in the normal internal carotid and vertebral arteries. *Physiological measurement*, 26(4):477, 2005.
- [8] Patricia Hernández-López, Miguel A. Martínez, Estefanía Peña, and Myriam Cilla. Understanding the Parameter Influence on Lesion Growth for a Mechanobiology Model of Atherosclerosis. *Mathematics*, 11(4):1–25, 2023. ISSN 22277390. doi: 10.3390/math11040829.
- [9] Matthew Hirschhorn, Vakhtang Tchantchaleishvili, Randy Stevens, Joseph Rossano, and Amy Throckmorton. Fluid–structure interaction modeling in cardiovascular medicine – A systematic review 2017–2019. *Medical Engineering and Physics*, 78:1–13, 2020. ISSN 18734030. doi: 10.1016/j.medengphy.2020.01.008. URL <https://doi.org/10.1016/j.medengphy.2020.01.008>.
- [10] Peter Lanzer, Fadil M. Hannan, Jan D. Lanzer, Jan Janzen, Paolo Raggi, Dominic Furniss, Mirjam Schuchardt, Rajesh Thakker, Pak Wing Fok, Julio Saez-Rodriguez, Angel Millan, Yu Sato, Roberto Ferraresi, Renu Virmani, and Cynthia St. Hilaire. Medial Arterial Calcification: JACC State-of-the-Art Review. *Journal of the American College of Cardiology*, 78(11):1145–1165, 2021. ISSN 15583597. doi: 10.1016/j.jacc.2021.06.049.
- [11] Sun Joo Lee, In Kyu Lee, and Jae Han Jeon. Vascular calcification—new insights into its mechanism. *International Journal of Molecular Sciences*, 21(8), 2020. ISSN 14220067. doi: 10.3390/ijms21082685.
- [12] Randall J LeVeque. *Finite volume methods for hyperbolic problems*, volume 31. Cambridge university press, 2002.
- [13] Steve A Maas, Benjamin J Ellis, Gerard A Ateshian, and Jeffrey A Weiss. *Febio: finite elements for biomechanics*. *Journal of Biomechanical Engineering*, 2012.
- [14] Whitney Menefee, Julie Jenks, Chiara Mazzasette, and Kim-Leiloni Nguyen. Human anatomy (OERI). [https://med.libretexts.org/Bookshelves/Anatomy_and_Physiology/Human_Anatomy_\(OERI\)](https://med.libretexts.org/Bookshelves/Anatomy_and_Physiology/Human_Anatomy_(OERI)), 2020. Accessed: October 25th, 2023.

- [15] Paul D. Morris, Andrew Narracott, Hendrik Von Tengg-Kobligk, Daniel Alejandro Silva Soto, Sarah Hsiao, Angela Lungu, Paul Evans, Neil W. Bressloff, Patricia V. Lawford, D. Rodney Hose, and Julian P. Gunn. Computational fluid dynamics modelling in cardiovascular medicine. *Heart*, 102(1):18–28, 2016. ISSN 1468201X. doi: 10.1136/heartjnl-2015-308044.
- [16] Wilmer W. Nichols, Michael O’Rourke, Charalambos Vlachopoulos, and Elazer R. Edelman. *McDonald’s Blood Flow in Arteries: Theoretical, Experimental and Clinical Principles*. CRC Press, August 2022. ISBN 9781351253765. doi: 10.1201/9781351253765. URL <http://dx.doi.org/10.1201/9781351253765>.
- [17] Ernesto Pimentel-García, Lucas O Müller, Eleuterio F Toro, and Carlos Parés. High-order fully well-balanced numerical methods for one-dimensional blood flow with discontinuous properties. *Journal of Computational Physics*, 475:111869, 2023.
- [18] Alfio Quarteroni and Luca Formaggia. Mathematical Modelling and Numerical Simulation of the Cardiovascular System. *Handbook of Numerical Analysis*, 12(03):3–127, 2004. ISSN 15708659. doi: 10.1016/S1570-8659(03)12001-7.
- [19] Alfio Quarteroni, Massimiliano Taveri, and Alessandro Veneziani. Computational vascular fluid dynamics: Problems, models and methods. *Computing and Visualization in Science*, 2(4):163–197, 2000. ISSN 14330369. doi: 10.1007/s007910050039.
- [20] Pritesh Ramya. Reduced order modelling of cerebral vasculature. Master’s thesis, TU Delft, 2024.
- [21] Philip L Roe. Approximate riemann solvers, parameter vectors, and difference schemes. *Journal of computational physics*, 43(2):357–372, 1981.
- [22] Timothy W. Secomb. Hemodynamics. *Physiology & behavior*, 176(3):139–148, 2017. doi: 10.1002/cphy.c150038.Hemodynamics.
- [23] S. J. Sherwin, V. Franke, J. Peiró, and K. Parker. One-dimensional modelling of a vascular network in space-time variables. *Journal of Engineering Mathematics*, 47(3-4):217–250, 2003. ISSN 00220833. doi: 10.1023/B:ENGI.0000007979.32871.e2.
- [24] Jay J Shim, Steve A Maas, Jeffrey A Weiss, and Gerard A Ateshian. A formulation for fluid–structure interactions in febio using mixture theory. *Journal of Biomechanical Engineering*, 141(5):051010, 2019.
- [25] N. P. Smith, A. J. Pullan, and P. J. Hunter. An anatomically based model of transient coronary blood flow in the heart. *SIAM Journal on Applied Mathematics*, 62(3):990–1018, 2002. ISSN 00361399. doi: 10.1137/S0036139999355199.
- [26] Eleuterio F Toro and Annunziato Siviglia. Flow in collapsible tubes with discontinuous mechanical properties: mathematical model and exact solutions. *Communications in Computational Physics*, 13(2):361–385, 2013.
- [27] E. van Groesen and Jaap Molenaar. *Continuum Modeling in the Physical Sciences*. Society for Industrial and Applied Mathematics, January 2007. ISBN 9780898718249. doi: 10.1137/1.9780898718249. URL <http://dx.doi.org/10.1137/1.9780898718249>.
- [28] Marie Willemet and Jordi Alastruey. Arterial Pressure and Flow Wave Analysis Using Time-Domain 1-D Hemodynamics. *Annals of Biomedical Engineering*, 43(1):190–206, 2015. ISSN 15739686. doi: 10.1007/s10439-014-1087-4.
- [29] Meiting Wu, Cameron Rementer, and Cecilia M. Giachelli. Vascular calcification: An update on mechanisms and challenges in treatment. *Calcified Tissue International*, 93(4):365–373, 2013. ISSN 0171967X. doi: 10.1007/s00223-013-9712-z.

A

The Axisymmetric Flow Model

This appendix obtains the axisymmetric flow model by incorporating all assumptions denoted in section 2.2.1, by conserving mass and balancing momentum within control volumes denoted in equation (2.2.14), and by applying lemma Lagrange (2D). The axisymmetric flow model obtains axisymmetric velocity ($\partial_\varphi u = 0$) from the continuity condition ($\partial_\varphi v(t, x, \varphi, 0) = 0$) due to the simplicity of the velocity profile.

This appendix starts by conserving mass in section A.1, proceeds by balancing momentum in section A.2 and ends by obtaining the differential form in section A.3.

A.1. Conservation of mass

This section will obtain the integral form of the conservation of mass equation within control volumes depicted in (2.2.14). By incorporating Assumption 4 into the conservation of mass equation (1.2.5), mass is conserved in the control volume if

$$\partial_t \int_{V(t)} \rho d\mathbf{x} + \int_{V(t)} \partial_x (\rho v_x) d\mathbf{x} = 0 \text{ for } t \in (0, T). \quad (\text{A.1.1})$$

Transforming into cylindrical coordinates yields

$$\rho \partial_t \int_{x_1}^{x_2} \int_{\varphi_1}^{\varphi_2} \int_0^R r dr d\varphi dx + \rho \int_{x_1}^{x_2} \int_{\varphi_1}^{\varphi_2} \int_0^R r \partial_x v_x dr d\varphi dx = 0 \text{ for } t \in (0, T). \quad (\text{A.1.2})$$

Applying the rescale $r = yR$ yields

$$\underbrace{\rho \partial_t \int_{x_1}^{x_2} \int_{\varphi_1}^{\varphi_2} R^2 \int_0^1 y dy d\varphi dx}_I + \underbrace{\rho \int_{x_1}^{x_2} \int_{\varphi_1}^{\varphi_2} R^2 \int_0^1 y \partial_x v_x dy d\varphi dx}_{II} = 0 \text{ for } t \in (0, T). \quad (\text{A.1.3})$$

Integrals I and II will be computed separately. Integral I is evaluated as

$$I = \frac{\rho}{2} \partial_t \int_{x_1}^{x_2} \int_{\varphi_1}^{\varphi_2} R^2 d\varphi dx. \quad (\text{A.1.4})$$

Assuming R is smooth enough leads to

$$I = \frac{\rho}{2} \int_{x_1}^{x_2} \int_{\varphi_1}^{\varphi_2} \partial_t R^2 d\varphi dx. \quad (\text{A.1.5})$$

By incorporating (2.2.2), integral II is equal to

$$\begin{aligned} II &= \rho \int_{x_1}^{x_2} \int_{\varphi_1}^{\varphi_2} R^2 \int_0^1 y \partial_x (us) dy d\varphi dx \\ &= \rho \int_{x_1}^{x_2} \int_{\varphi_1}^{\varphi_2} R^2 \partial_x u \int_0^1 ys dy d\varphi dx + \rho \int_{x_1}^{x_2} \int_{\varphi_1}^{\varphi_2} u R^2 \int_0^1 y \frac{\partial s}{\partial y} \frac{\partial y}{\partial R} \frac{\partial R}{\partial x} dy d\varphi dx \\ &= \rho \int_{x_1}^{x_2} \int_{\varphi_1}^{\varphi_2} R^2 \partial_x u \int_0^1 ys dy d\varphi dx - \rho \int_{x_1}^{x_2} \int_{\varphi_1}^{\varphi_2} u R \partial_x R \int_0^1 y^2 s' dy d\varphi dx. \end{aligned} \quad (\text{A.1.6})$$

By applying partial integration and property (1.3.5), we obtain

$$\int_0^1 y^2 s' dy = -2 \int_0^1 y s dy. \quad (\text{A.1.7})$$

By applying (A.1.7) and property (1.3.6), integral II is equal to

$$\begin{aligned} II &= \frac{\rho}{2} \int_{x_1}^{x_2} \int_{\varphi_1}^{\varphi_2} R^2 \partial_x u + 2uR \partial_x R d\varphi dx \\ &= \frac{\rho}{2} \int_{x_1}^{x_2} \int_{\varphi_1}^{\varphi_2} \partial_x (uR^2) d\varphi dx \end{aligned} \quad (\text{A.1.8})$$

By adding (A.1.5) and (A.1.8), mass is conserved if

$$\int_{x_1}^{x_2} \int_{\varphi_1}^{\varphi_2} \partial_t (R^2) + \partial_x (uR^2) d\varphi dx = 0 \text{ for } t \in (0, T). \quad (\text{A.1.9})$$

A.2. Balance of momentum

This section will obtain the integral form of the balance of momentum equation within control volumes depicted in (2.2.14). By incorporating Assumption 4 into the balance of momentum equation (1.2.8), momentum is balanced in the control volume if

$$\underbrace{\partial_t \int_{V(t)} \rho v_x d\mathbf{x}}_{III} + \underbrace{\int_{V(t)} 2\rho v_x \partial_x v_x d\mathbf{x}}_{IV} = \underbrace{\int_{V(t)} \mu (\partial_x^2 v_x \Delta v_x) d\mathbf{x}}_V - \underbrace{\int_{V(t)} \partial_x P d\mathbf{x}}_{VI} \text{ for } t \in (0, T).$$

Each of the integrals III , IV , V , and VI will be computed separately.

Integral III

Transforming into cylindrical coordinates and applying the rescale $r = yR$ yields

$$III = \rho \partial_t \int_{x_1}^{x_2} \int_{\varphi_1}^{\varphi_2} R^2 \int_0^1 y v_x dy d\varphi dx.$$

By incorporating (2.2.2) and the normalization property (1.3.6), III is equal to

$$\frac{\rho}{2} \partial_t \int_{x_1}^{x_2} \int_{\varphi_1}^{\varphi_2} uR^2 d\varphi dx.$$

Assuming that uR^2 is smooth enough yields

$$III = \frac{\rho}{2} \int_{x_1}^{x_2} \int_{\varphi_1}^{\varphi_2} \partial_t (uR^2) d\varphi dx. \quad (\text{A.2.1})$$

Integral IV

Transforming into cylindrical coordinates and applying the rescale $r = yR$ yields

$$IV = 2\rho \int_{x_1}^{x_2} \int_{\varphi_1}^{\varphi_2} R^2 \int_0^1 y v_x \partial_x v_x dy d\varphi dx.$$

By incorporating $v_x(t, x, \varphi, Ry) = u(t, x)s(y)$, we have

$$\begin{aligned} IV &= 2\rho \int_{x_1}^{x_2} \int_{\varphi_1}^{\varphi_2} R^2 \int_0^1 y u s \partial_x (u s) dy d\varphi dx \\ &= 2\rho \int_{x_1}^{x_2} \int_{\varphi_1}^{\varphi_2} u \partial_x (u) R^2 \int_0^1 y s^2 dy + u^2 R^2 \int_0^1 y s \frac{\partial s}{\partial y} \frac{\partial y}{\partial R} \frac{\partial R}{\partial x} dy d\varphi dx \\ &= 2\rho \int_{x_1}^{x_2} \int_{\varphi_1}^{\varphi_2} u \partial_x (u) R^2 \int_0^1 y s^2 dy - u^2 R \partial_x R \int_0^1 \frac{1}{2} y^2 \partial_y (s^2) dy d\varphi dx \end{aligned}$$

where $\partial_y(s^2) = 2ss'$. By applying partial integration and property (1.3.5), we obtain

$$\int_0^1 \frac{1}{2} y^2 \partial_y(s^2) dy = - \int_0^1 y s^2 dy. \quad (\text{A.2.2})$$

Applying (A.2.2) into IV yields

$$\begin{aligned} IV &= \rho \int_{x_1}^{x_2} \int_{\varphi_1}^{\varphi_2} \alpha [u \partial_x(u) R^2 + u^2 R \partial_x R] d\varphi dx \\ &= \frac{\rho}{2} \int_{x_1}^{x_2} \int_{\varphi_1}^{\varphi_2} \alpha [\partial_x(u^2) R^2 + u^2 \partial_x(R^2)] d\varphi dx \\ &= \frac{\rho}{2} \int_{x_1}^{x_2} \int_{\varphi_1}^{\varphi_2} \alpha \partial_x(u^2 R^2) d\varphi dx, \end{aligned} \quad (\text{A.2.3})$$

where $\alpha = 2 \int_0^1 y s^2 dy$ is known as the momentum-flux correction term. By applying the velocity profile $s(y) = \frac{\gamma+2}{\gamma} (1-y^\gamma)$, α is evaluated as

$$\alpha = 2 \int_0^1 y s^2(y) dy = \frac{(\gamma+2)^2}{\gamma^2} 2 \int_0^1 y (1-y^\gamma)^2 dy = \frac{\gamma+2}{\gamma+1} \quad (\text{A.2.4})$$

where

$$\begin{aligned} \int_0^1 y (1-y^\gamma)^2 dy &= \int_0^1 y - 2y^{\gamma+1} + y^{2\gamma+1} dy \\ &= \frac{1}{2} \left(1 - \frac{4}{\gamma+2} + \frac{1}{\gamma+1} \right) \\ &= \frac{1}{2} \frac{(\gamma+1)(\gamma+2) - 4(\gamma+1) + \gamma+2}{(\gamma+1)(\gamma+2)} \\ &= \frac{1}{2} \frac{\gamma^2}{(\gamma+1)(\gamma+2)}. \end{aligned} \quad (\text{A.2.5})$$

α is plotted in Figure A.1.

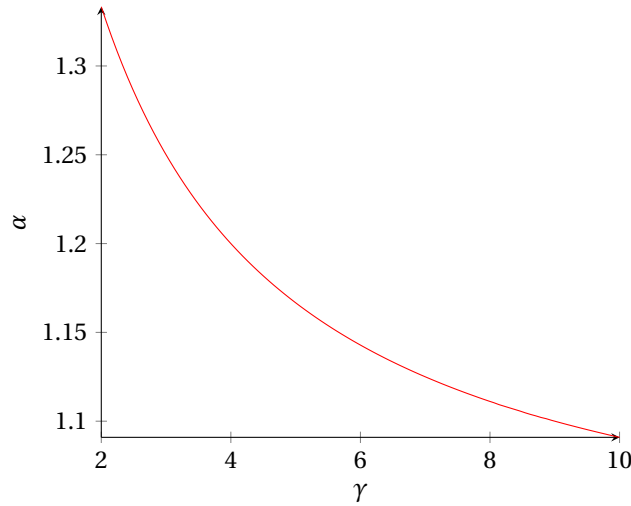


Figure A.1: Plot of momentum-flux correction coefficient.

Integral V

Transforming into cylindrical coordinates yields

$$V = \mu \int_{x_1}^{x_2} \int_{\varphi_1}^{\varphi_2} \int_0^R \underbrace{2r \partial_x^2 v_x}_{V_a} + \underbrace{\frac{1}{r} \partial_\varphi^2 v_x}_{V_b} + \underbrace{\partial_r(r \partial_r v_x)}_{V_c} dy d\varphi dx,$$

where V_a is neglected by Assumption 6,

$$V_b = \frac{\mu}{2} \int_{x_1}^{x_2} \int_{\varphi_1}^{\varphi_2} 2u \frac{(\gamma+2)^2}{\gamma} \frac{\partial_\varphi^2 R}{R} - u \frac{(\gamma+1)(\gamma+2)}{\gamma} \frac{\partial_\varphi^2 (R^2)}{R^2} d\varphi dx \quad (\text{A.2.6})$$

has already been computed in section 2.2.2. By incorporating $v_x(t, x, \varphi, Ry) = u(t, x)s(y)$, we obtain

$$\begin{aligned} V_c &= \mu \int_{x_1}^{x_2} \int_{\varphi_1}^{\varphi_2} \int_0^R \partial_r (r \partial_r [us]) dr d\varphi dx \\ &= \mu \int_{x_1}^{x_2} \int_{\varphi_1}^{\varphi_2} u \int_0^R \partial_r \left(r \frac{ds}{dy} \frac{\partial y}{\partial r} \right) dr d\varphi dx \\ &= \mu \int_{x_1}^{x_2} \int_{\varphi_1}^{\varphi_2} u \int_0^R \partial_r \left(\frac{r}{R} s' \left(\frac{r}{R} \right) \right) dr d\varphi dx \\ &= \mu s'(1) \int_{x_1}^{x_2} \int_{\varphi_1}^{\varphi_2} u d\varphi dx \\ &= -\frac{\mu}{2} (\gamma+2) \int_{x_1}^{x_2} \int_{\varphi_1}^{\varphi_2} 2u d\varphi dx. \end{aligned} \quad (\text{A.2.7})$$

Integral VI

Transforming into cylindrical coordinates and applying the rescale $r = yR$ yields

$$VI = \int_{x_1}^{x_2} \int_{\varphi_1}^{\varphi_2} R^2 \partial_x P \int_0^1 y dy d\varphi dx = \frac{1}{2} \int_{x_1}^{x_2} \int_{\varphi_1}^{\varphi_2} R^2 \partial_x P d\varphi dx.$$

The expression for P can be obtained by satisfying the dynamic coupling condition, in which pressure exerted on the inner arterial wall is balanced by the pressure generated in the blood. By incorporating the deformation model depicted in (2.2.1), we obtain

$$VI = \frac{1}{2} \int_{x_1}^{x_2} \int_{\varphi_1}^{\varphi_2} \frac{R^2 \partial_x R}{R_0^2} \beta + R^2 \frac{R - R_0}{R_0^2} \partial_x \beta d\varphi dx \quad (\text{A.2.8})$$

A.3. Differential form

The integral form of the balance of momentum equation becomes

$$\begin{aligned} \int_{x_1}^{x_2} \int_{\varphi_1}^{\varphi_2} \rho \partial_t (uR^2) + \rho \frac{\gamma+2}{\gamma+1} \partial_x (u^2 R^2) d\varphi dx &= \int_{x_1}^{x_2} \int_{\varphi_1}^{\varphi_2} \mu \frac{\gamma+2}{\gamma} u \left(-2\gamma \right. \\ &\left. + 2(\gamma+2) \frac{\partial_\varphi^2 R}{R} - (\gamma+1) \frac{\partial_\varphi^2 (R^2)}{R^2} \right) - \frac{R^2 \partial_x R}{R_0^2} \beta - R^2 \frac{R - R_0}{R_0^2} \partial_x \beta d\varphi dx \text{ for } t \in (0, T). \end{aligned} \quad (\text{A.3.1})$$

The integral form of the conservation of mass (A.1.9) and the balance of momentum equations hold for every open rectangle $I = (x_1, x_2) \times (\varphi_1, \varphi_2) \subseteq \Omega = (0, L) \times (0, 2\pi)$ where $0 < x_1 < x_2 < L$ and $0 < \varphi_1 < \varphi_2 < 0$. By assuming that $R \in C^1(0, T) \times C^2(\Omega)$ and $u \in C^1(0, T) \times C^2(0, L)$, lemma Lagrange (2D) is applied to obtain the differential form for the axisymmetric flow model

$$\partial_t (R^2) + \partial_x (uR^2) = 0 \text{ for } (t, x, \varphi) \in (0, T) \times \Omega, \quad (\text{A.3.2})$$

$$\begin{aligned} \rho \partial_t (uR^2) + \rho \frac{\gamma+2}{\gamma+1} \partial_x (u^2 R^2) &= \mu \frac{\gamma+2}{\gamma} u \left(-2\gamma + 2(\gamma+2) \frac{\partial_\varphi^2 R}{R} \right. \\ &\left. - (\gamma+1) \frac{\partial_\varphi^2 (R^2)}{R^2} \right) - \frac{R^2 \partial_x R}{R_0^2} \beta - R^2 \frac{R - R_0}{R_0^2} \partial_x \beta \text{ for } (t, x, \varphi) \in (0, T) \times \Omega, \end{aligned} \quad (\text{A.3.3})$$

$$\partial_\varphi u = 0, \quad (\text{A.3.4})$$

B

The Asymmetric Flow Model

The asymmetric flow model aims to obtain a model that allows asymmetric mean velocity within the artery. As seen in the axisymmetric flow model, the velocity profile is too simple, such that the continuity condition leads to a mean axisymmetric velocity. To obtain asymmetric mean velocity, we propose to extend the velocity profile by letting $\gamma(t, x, \varphi) : [0, T] \times \Omega \rightarrow (0, \infty)$ also depends on t , x and φ . This proposal models blood flow in 2D by allowing more velocity profiles

$$s(y, \gamma) = \frac{\gamma + 2}{\gamma} (1 - y^\gamma) \quad (\text{B.0.1})$$

since γ is no longer fixed. From the continuity condition (2.2.4) we can show that for $\gamma > 0$

$$\begin{aligned} \lim_{r \downarrow 0} \partial_\varphi v_x(t, x, \varphi, r) &= \lim_{y \downarrow 0} \partial_\varphi [u(t, x, \varphi) s(y, \gamma)] \\ &= \frac{\gamma + 2}{\gamma} \partial_\varphi u - 2u \frac{\partial_\varphi \gamma}{\gamma^2} \\ &= \partial_\varphi \left(\frac{\gamma + 2}{\gamma} u \right) = 0. \end{aligned} \quad (\text{B.0.2})$$

where $y^\gamma \ln y \rightarrow 0$ as $y \rightarrow 0$ (see (2.2.28)). By integrating (B.0.2) over φ , we obtain

$$D = u \frac{\gamma + 2}{\gamma} =: v_x(t, x, \varphi, 0) \quad (\text{B.0.3})$$

where $D(t, x)$ is an unknown function independent of φ . D represents the axial velocity at the artery's origin, which attains the maximum velocity within the artery's cross-section (due to the applied velocity profile).

This appendix is split into three parts. B.1 conserves mass within control volumes, B.2 balances momentum within control volumes and B.3 obtains the differential form by applying lemma Lagrange (2D).

B.1. Conservation of mass

This section will obtain the integral form of the conservation of mass equation within control volumes depicted in (2.2.14). By taking identical steps as the axisymmetric flow model, mass is conserved if

$$\underbrace{\rho \partial_t \int_{x_1}^{x_2} \int_{\varphi_1}^{\varphi_2} R^2 \int_0^1 y dy d\varphi dx}_{I} + \rho \underbrace{\int_{x_1}^{x_2} \int_{\varphi_1}^{\varphi_2} R^2 \int_0^1 y \partial_x v_x dy d\varphi dx}_{II} = 0 \text{ for } t \in (0, T). \quad (\text{B.1.1})$$

Since I does not have the derivative of v_x , similar steps can be taken as in the axisymmetric flow model to obtain $I = \frac{\rho}{2} \int_{x_1}^{x_2} \int_{\varphi_1}^{\varphi_2} \partial_t (R^2) d\varphi dx$. With the partial derivative

$$\frac{\partial v_x}{\partial x} = \frac{\partial u s}{\partial x} = \frac{\partial u}{\partial x} s + u \frac{\partial s}{\partial x} = \frac{\partial u}{\partial x} s + u \left(\frac{\partial s}{\partial y} \frac{\partial y}{\partial R} \frac{\partial R}{\partial x} + \frac{\partial s}{\partial \gamma} \frac{\partial \gamma}{\partial x} \right), \quad (\text{B.1.2})$$

Π is equal to

$$\begin{aligned} \Pi &= \rho \int_{x_1}^{x_2} \int_{\varphi_1}^{\varphi_2} \overbrace{R^2 \partial_x u \int_0^1 y s dy + u R^2 \int_0^1 y \frac{\partial s}{\partial y} \frac{\partial y}{\partial R} \frac{\partial R}{\partial x} dy + R^2 \int_0^1 y \frac{\partial s}{\partial \gamma} \frac{\partial \gamma}{\partial x} dy d\varphi dx}_{\Pi_{axi}} \\ &= \rho \int_{x_1}^{x_2} \int_{\varphi_1}^{\varphi_2} \frac{1}{2} \partial_x (u R^2) + R^2 \partial_x \gamma \int_0^1 \partial_\gamma s dy d\varphi dx, \end{aligned} \quad (\text{B.1.3})$$

where $\Pi_{axi} = \frac{\rho}{2} \int_{x_1}^{x_2} \int_{\varphi_1}^{\varphi_2} \partial_x (u R^2) d\varphi dx$ has already been computed in the axisymmetric flow model. The integral $\int_0^1 y \partial_\gamma s dy$ is evaluated as

$$\begin{aligned} \int_0^1 y \partial_\gamma s dy &= -\frac{2}{\gamma^2} \int_0^1 y - y^{\gamma+1} dy - \frac{\gamma+2}{\gamma} \int_0^1 y^{\gamma+1} \ln y dy \\ &= -\frac{2}{\gamma^2} \left(\frac{1}{2} - \frac{1}{\gamma+2} \right) + \frac{1}{\gamma(\gamma+2)} \\ &= -\frac{2}{\gamma^2} \frac{\gamma}{2(\gamma+2)} + \frac{1}{\gamma(\gamma+2)} = 0, \end{aligned} \quad (\text{B.1.4})$$

where for $\int_0^1 y^{\gamma+1} \ln y dy = -\frac{1}{(\gamma+2)^2}$ (see (2.2.30)). The conservation of mass equation for the asymmetric flow model becomes

$$\frac{\rho}{2} \int_{x_1}^{x_2} \int_{\varphi_1}^{\varphi_2} \partial_t (R^2) + \partial_x (u R^2) d\varphi dx = 0. \quad (\text{B.1.5})$$

The conservation of mass equation is identical to the continuity equation, even if γ is no longer a constant.

B.2. Balance of momentum

This section will obtain the integral form of the balance of momentum equation within control volumes depicted in (2.2.14). Similar to the axisymmetric flow model, momentum is balanced if

$$\underbrace{\partial_t \int_{V(t)} \rho v_x d\mathbf{x}}_{III} + \underbrace{\int_{V(t)} 2\rho v_x \partial_x v_x d\mathbf{x}}_{IV} = \underbrace{\int_{V(t)} \mu (\partial_x + \Delta v_x) d\mathbf{x}}_V - \underbrace{\int_{V(t)} \partial_x P d\mathbf{x}}_{VI} \quad \text{for } t \in (0, T). \quad (\text{B.2.1})$$

Integrals *III* and *VI* are identically obtained as the axisymmetric flow model, evaluated as

$$III = \frac{\rho}{2} \int_{x_1}^{x_2} \int_{\varphi_1}^{\varphi_2} \partial_t (u R^2) d\varphi dx, \quad (\text{A.2.1})$$

and

$$VI = \frac{1}{2} \int_{x_1}^{x_2} \int_{\varphi_1}^{\varphi_2} \frac{R^2 \partial_x R}{R_0^2} \beta + R^2 \frac{R - R_0}{R_0^2} \partial_x \beta d\varphi dx \quad (\text{A.2.8})$$

where $\beta = \frac{4}{3} E h$. Integrals *IV* and *V* need further investigation.

Integral *IV*

Transforming into cylindrical coordinates and applying the rescale $r = yR$ yields

$$IV = \rho \int_{x_1}^{x_2} \int_{\varphi_1}^{\varphi_2} R^2 \int_0^1 y v_x \partial_x v_x dy d\varphi dx. \quad (\text{B.2.2})$$

With the partial derivative

$$\frac{\partial v_x}{\partial x} = \frac{\partial u}{\partial x} s + u \left(\frac{\partial s}{\partial y} \frac{\partial y}{\partial R} \frac{\partial R}{\partial x} + \frac{\partial s}{\partial \gamma} \frac{\partial \gamma}{\partial x} \right), \quad (\text{B.2.3})$$

IV is identical to

$$\begin{aligned}
 IV &= \overbrace{\rho \int_{x_1}^{x_2} \int_{\varphi_1}^{\varphi_2} u \partial_x(u) R^2 \int_0^1 y s^2 dy + u^2 R^2 \int_0^1 y s \frac{\partial s}{\partial y} \frac{\partial y}{\partial R} \frac{\partial R}{\partial x} dy d\varphi dx}_{IV_{axi}} \\
 &\quad + \rho \int_{x_1}^{x_2} \int_{\varphi_1}^{\varphi_2} u^2 R^2 \int_0^1 y s \frac{\partial s}{\partial \gamma} \frac{\partial \gamma}{\partial x} dy d\varphi dx \\
 &= \frac{\rho}{2} \int_{x_1}^{x_2} \int_{\varphi_1}^{\varphi_2} \frac{\gamma+2}{\gamma+1} \partial_x(u^2 R^2) + 2\alpha_2 u^2 R^2 \partial_x \gamma d\varphi dx,
 \end{aligned} \tag{B.2.4}$$

where $\alpha_2 = \int_0^1 y s \partial_\gamma s dy$. IV_{axi} has already been computed in the axisymmetric flow model and α_2 consists of integrals already computed in (A.2.5) and (2.2.30). α_2 is evaluated as

$$\begin{aligned}
 \alpha_2 &= -2 \frac{\gamma+2}{\gamma^3} \int_0^1 y(1-y^\gamma)^2 dy - \frac{(\gamma+2)^2}{\gamma^2} \int_0^1 y^{\gamma+1} \ln y - y^{2\gamma+1} \ln y dy \\
 &= -2 \frac{\gamma+2}{\gamma^3} \frac{\gamma^2}{(\gamma+1)(\gamma+2)} + \frac{(\gamma+2)^2}{4\gamma^2} \left(\frac{4}{(\gamma+2)^2} - \frac{1}{(\gamma+1)^2} \right) \\
 &= -\frac{2}{\gamma(\gamma+1)} + \frac{3\gamma+4}{4\gamma(\gamma+1)^2} = -\frac{5\gamma+4}{4\gamma(\gamma+1)^2}
 \end{aligned} \tag{B.2.5}$$

and is plotted in Figure B.1.

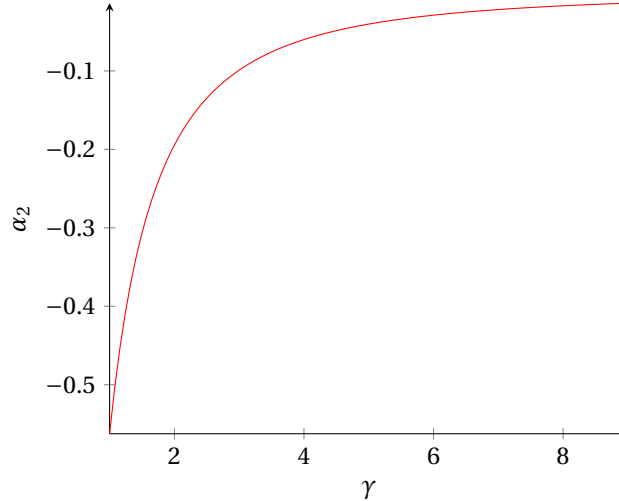


Figure B.1: Plot of α_2 .

Integral V

Transforming into cylindrical coordinates yields

$$V = \mu \int_{x_1}^{x_2} \int_{\varphi_1}^{\varphi_2} \int_0^R \underbrace{2r \partial_x^2 v_x}_{V_a} + \underbrace{\frac{1}{r} \partial_\varphi^2 v_x}_{V_b} + \underbrace{\partial_r(r \partial_r v_x)}_{V_c} dy d\varphi dx, \tag{B.2.6}$$

where V_a is neglected by Assumption 6,

$$V_b = \mu \int_{x_1}^{x_2} \int_{\varphi_1}^{\varphi_2} u \frac{\gamma+2}{\gamma} \left((\gamma+2) \frac{\partial_\varphi^2 R}{R} - \frac{\gamma+1}{2} \frac{\partial_\varphi^2 (R^2)}{R^2} + 2 \frac{\gamma-1}{\gamma^2} \partial_\varphi \gamma \frac{\partial_\varphi R}{R} - \frac{2}{\gamma^3} (\partial_\varphi \gamma)^2 + \frac{1}{\gamma^2} \partial_\varphi^2 \gamma \right) d\varphi dx \tag{B.2.7}$$

has been computed in section 2.2.3, and

$$V_c = -\frac{\mu}{2} (\gamma+2) \int_{x_1}^{x_2} \int_{\varphi_1}^{\varphi_2} 2u d\varphi dx. \tag{A.2.7}$$

has been computed in the axisymmetric flow model.

B.3. Differential form

The integral form of the balance of momentum equation becomes

$$\begin{aligned}
& \int_{x_1}^{x_2} \int_{\varphi_1}^{\varphi_2} \rho \partial_t (uR^2) + \rho \frac{\gamma+2}{\gamma+1} \partial_x (u^2 R^2) - u^2 R^2 \frac{5\gamma+4}{2\gamma(\gamma+1)^2} \partial_x \gamma \, d\varphi \, dx \\
&= \int_{x_1}^{x_2} \int_{\varphi_1}^{\varphi_2} 2\mu u \frac{\gamma+2}{\gamma} \left(-\gamma + (\gamma+2) \frac{\partial_\varphi^2 R}{R} - \frac{\gamma+1}{2} \frac{\partial_\varphi^2 (R^2)}{R^2} + 2 \frac{\gamma-1}{\gamma^2} \partial_\varphi \gamma \frac{\partial_\varphi R}{R} \right. \\
&\quad \left. - \frac{2}{\gamma^3} (\partial_\varphi \gamma)^2 + \frac{1}{\gamma^2} \partial_\varphi^2 \gamma \right) - \frac{R^2 \partial_x R}{R_0^2} \beta - R^2 \frac{R-R_0}{R_0^2} \partial_x \beta \, d\varphi \, dx.
\end{aligned} \tag{B.3.1}$$

The integral form of the conservation of mass (B.1.5) and the balance of momentum equations hold for $t \in (0, T)$ and for every open rectangle $I = (x_1, x_2) \times (\varphi_1, \varphi_2) \subset \Omega = (0, L) \times (0, 2\pi)$ where $0 < x_1 < x_2 < L$ and $0 < \varphi_1 < \varphi_2 < 0$. By assuming that $R \in C^1(0, T) \times C^2(\Omega)$, $u \in C^1(0, T) \times C^2(\Omega)$ and $\gamma \in C^1(0, T) \times C^2(\Omega)$, lemma Lagrange 2D can be applied to obtain the differential form for the asymmetric flow model. The equations govern the asymmetric flow model

$$\partial_t (R^2) + \partial_x (uR^2) = 0, \tag{B.3.2}$$

$$\begin{aligned}
& \rho \partial_t (uR^2) + \rho \frac{\gamma+2}{\gamma+1} \partial_x (u^2 R^2) = u^2 R^2 \frac{5\gamma+4}{2\gamma(\gamma+1)^2} \partial_x \gamma + 2\mu u \frac{\gamma+2}{\gamma} \left(-\gamma + (\gamma+2) \frac{\partial_\varphi^2 R}{R} \right. \\
& \left. - \frac{\gamma+1}{2} \frac{\partial_\varphi^2 (R^2)}{R^2} + 2 \frac{\gamma-1}{\gamma^2} \partial_\varphi \gamma \frac{\partial_\varphi R}{R} - \frac{2}{\gamma^3} (\partial_\varphi \gamma)^2 + \frac{1}{\gamma^2} \partial_\varphi^2 \gamma \right) - \frac{R^2 \partial_x R}{R_0^2} \beta - R^2 \frac{R-R_0}{R_0^2} \partial_x \beta
\end{aligned} \tag{B.3.3}$$

$$\partial_\varphi \left(\frac{\gamma+2}{\gamma} u \right) = 0. \tag{B.0.2}$$

C

Roe's Linearization to 1D Blood Flow

Roe's linearization can be applied to inviscid flow for the 1D ROM (equations (1.3.13) and (1.3.17), where $K_r = 0$). By choosing the parameter vector

$$\mathbf{z} = \frac{\mathbf{q}}{\sqrt{A}}, \implies \mathbf{z} = \begin{bmatrix} z^1 \\ z^2 \end{bmatrix} = \begin{bmatrix} \sqrt{A} \\ \frac{Q}{\sqrt{A}} \end{bmatrix}$$

we obtain its inverse [12]

$$\mathbf{q}(\mathbf{z}) = \begin{bmatrix} (z^1)^2 \\ z^1 z^2 \end{bmatrix} \implies \frac{\partial \mathbf{q}}{\partial \mathbf{z}} = \begin{bmatrix} 2z^1 & 0 \\ z^2 & z^1 \end{bmatrix}$$

and the flux function

$$\mathbf{f}(\mathbf{z}) = \begin{bmatrix} z^1 z^2 \\ \alpha (z^2)^2 + (z^1)^3 \frac{\beta}{3\rho A_0} \end{bmatrix} \implies \frac{\partial \mathbf{f}}{\partial \mathbf{z}} = \begin{bmatrix} z^2 & z^1 \\ (z^1)^2 \frac{\beta}{\rho A_0} & 2\alpha z^2 \end{bmatrix}.$$

Since $\partial \mathbf{f} / \partial \mathbf{z}$ and $\partial \mathbf{q} / \partial \mathbf{z}$ only contains polynomials of z^p for $p \in \{1, 2\}$, Roe's linearization will yield easy to compute averages. By setting

$$z^p(\xi) = Z_{i-1}^p + (Z_i^p - Z_{i-1}^p) \xi \text{ for } p \in \{1, 2\}$$

we obtain in the limit of $Z_i^p - Z_{i-1}^p \rightarrow 0$

$$\hat{B}_{i-1/2} := \int_0^1 \frac{d\mathbf{q}(\mathbf{z}(\xi))}{d\mathbf{z}} d\xi = \begin{bmatrix} 2\bar{Z}^1 & 0 \\ \bar{Z}^2 & \bar{Z}^1 \end{bmatrix} \text{ and } \hat{C}_{i-1/2} := \int_0^1 \frac{d\mathbf{f}(\mathbf{z}(\xi))}{d\mathbf{z}} d\xi = \begin{bmatrix} \bar{Z}^2 & \bar{Z}^1 \\ \bar{Z}^1 \frac{\beta}{\rho A_0} & 2\alpha \bar{Z}^2 \end{bmatrix}$$

where

$$\bar{Z}^p := \int_0^1 z^p(\xi) d\xi = \frac{1}{2} \frac{(Z_i^p)^2 - (Z_{i-1}^p)^2}{Z_i^p - Z_{i-1}^p} = \frac{1}{2} (Z_i^p + Z_{i-1}^p)$$

and

$$\bar{Z}^p := \int_0^1 (z^p(\xi))^2 d\xi = \frac{1}{3} \frac{(Z_i^p)^3 - (Z_{i-1}^p)^3}{Z_i^p - Z_{i-1}^p} = \frac{1}{3} ((Z_i^p)^2 + Z_i^p Z_{i-1}^p + (Z_{i-1}^p)^2).$$

Roe's linearization yields

$$\hat{H}_{i-1/2} = \hat{C}_{i-1/2} (\hat{B}_{i-1/2})^{-1} = \begin{bmatrix} 0 & 1 \\ \frac{\hat{R}\beta}{2\rho A_0} - \alpha \bar{u}^2 & 2\alpha \bar{u} \end{bmatrix}$$

where $\bar{u} = \bar{Z}^2 / \bar{Z}^1$ and $\hat{R} = \bar{Z}^1 / \bar{Z}^1$.

D

Lemma Lagrange (2D)

The following lemma will be proven in this appendix.

Lemma Lagrange (2D). Let Ω be an open subset of \mathbb{R}^d , $f : \Omega \rightarrow \mathbb{R}$ be continuous in Ω and let $\int_V f(\mathbf{x}) d\mathbf{x} = 0$ for every open rectangle $V \subseteq \Omega$, then $f(\mathbf{x}) = 0$ in Ω .

This lemma is extended from Lemma 2.2a (Lagrange) [27]. The following mathematical definitions will be applied to prove this lemma.

Definition Continuity. Let $\Omega \subset \mathbb{R}^d$ be open and $f : \Omega \rightarrow \mathbb{R}$ be a mapping. The mapping f is continuous in Ω if for every $\mathbf{x} \in \Omega$, $\mathbf{y} \in \Omega$ and $\varepsilon > 0$ there exist a $\delta > 0$ such that $\|\mathbf{x} - \mathbf{y}\|_2 < \delta$ implies $|f(\mathbf{x}) - f(\mathbf{y})| < \varepsilon$.

Definition Interval. $I \subset \mathbb{R}$ is called an interval if there exist an $x_1 < x_2$ such that $I = [x_1, x_2]$.

Definition Rectangle. $I \subset \mathbb{R}^d$ is called a rectangle in \mathbb{R}^d if there exist intervals I_1, I_2, \dots, I_d such that $I = I_1 \times I_2 \times \dots \times I_d$.

Definition Open ball. $B_r(\mathbf{x}) \subset \mathbb{R}^d$ is called an open ball centered at $\mathbf{x} \in \mathbb{R}^d$ with a radius of $r > 0$ defined as $B_r(\mathbf{x}) = \{y \in \mathbb{R}^2 : \|x - y\|_2 < r\}$, where $\|\mathbf{x}\|_2$ denotes the euclidean norm. Furthermore, let $B_r^\infty(\mathbf{x})$ be an open set defined as $B_r^\infty(\mathbf{x}) = \{y \in \mathbb{R}^2 : \|x - y\|_\infty < r\}$, where $\|\mathbf{x}\|_\infty$ denotes the maximum norm $\max_i |x_i|$.

With these definitions, lemma Lagrange (2D) will be proven.

Proof Lemma Lagrange (2D). Let there be an $\mathbf{x}_0 = (x_1, x_2) \in \Omega$ such that $f(\mathbf{x}_0) > 0$. Choose $r > 0$ such that $f(\mathbf{x}) > 0$ for $\mathbf{x} \in B_r(\mathbf{x}_0) \subset \Omega$ and let $\rho = \frac{r}{\sqrt{2}}$. $B_\rho^\infty(\mathbf{x}_0) \subset B_r(\mathbf{x}_0)$ since for $\mathbf{y} \in \mathbb{R}^2$, $\|\mathbf{y}\|_2 \leq \sqrt{2}\|\mathbf{y}\|_\infty$. The set $B_\rho^\infty(\mathbf{x}_0)$ is equal to the open rectangle $I = (x_1 - \rho, x_1 + \rho) \times (x_2 - \rho, x_2 + \rho)$. Since f is strictly positive on $I \subset B_r(\mathbf{x}_0)$, an open rectangle I is found such that $\int_I f(\mathbf{x}) d\mathbf{x} > 0$. This however contradicts $\int_V f(\mathbf{x}) dV = 0$ for every open rectangle $V \subset \Omega$, so there does not exist an $\mathbf{x}_0 \in \Omega$ such that $f(\mathbf{x}_0) > 0$. Since assuming that there exists an $\mathbf{x}_0 \in \Omega$ such that $f(\mathbf{x}_0) < 0$ leads to a contradiction by taking similar steps, the proof is concluded.

In hindsight, this proof is trivial since the vector norms $\|\cdot\|_2$ and $\|\cdot\|_\infty$ are equivalent norms on \mathbb{R}^2 .